Elisabeth Savitri Thrane

Effect of Natural Ageing on an Al-Cu-Mg-Si Alloy

A Transmission Electron Microscopy Study

Master's thesis in Physics
Supervisor: Randi Holmestad
Co-supervisor: Sigurd Wenner
June 2022

Master's thesis

NTNU
Norwegian University of
Science and Technology

Elisabeth Savitri Thrane

Effect of Natural Ageing on an Al-Cu-Mg-Si Alloy

A Transmission Electron Microscopy Study

Master's thesis in Physics
Supervisor: Randi Holmestad
Co-supervisor: Sigurd Wenner
June 2022

Norwegian University of Science and Technology
Faculty of Natural Sciences
Department of Physics

NTNU
Kunnskap for en bedre verden

Abstract

The effect of different natural ageing times on precipitate evolution in an undeformed Al-Cu-Mg-Si alloy has been investigated by a variety of transmission electron microscopy (TEM) techniques. The study aimed to relate precipitate quantification, morphology, and crystal structure to the alloy's macroscopic properties, specifically its hardness. Similar research on this alloy has been done before but in that case with deformation. Heat treatments with and without natural ageing were conducted. Two samples were stored at RT for 20 hours before placed in an oven for artificial ageing, while two samples were directly aged. The artificial ageing times for these samples were either 48 hours (peak-age) or 6 hours (underaged). These four conditions were investigated by TEM. Bright field, dark field and convergent beam electron diffraction imaging were used to collect precipitate statistics and study their morphology. High resolution TEM (HRTEM), high angle annular dark field scanning transmission electron microscopy (HAADF-STEM), and scanning precession electron diffraction (SPED) were utilized to investigate precipitate crystal structures. SPED was also used for strain mapping.

It was found that the naturally aged samples exhibited a reduced hardness, also known as the negative effect of natural ageing, and this was especially prominent in the underaged conditions. This was related to a decreased volume fraction, number density and length of the precipitates. The aspect ratio of precipitate cross-sections was measured and the results showed that the naturally aged conditions had more lath-shaped precipitates, while the directly aged conditions had more rod-shaped precipitates. Moreover, it was discovered for the naturally aged conditions that the aspect ratio increased as the cross-section area increased. Phase identification with HRTEM, HAADF-STEM and SPED showed that most of the precipitates in the peak-aged conditions were the L phase, except for two β'' precipitates found with non-negative matrix factorization. The strain maps showed a clear difference in the strain fields surrounding the L phase and the β'' phase.

Sammendrag

Effekten av naturlig elding på utfelling av presipitater i en udeformert Al-Cu-Mg-Si legering ble undersøkt ved ulike teknikker i transmisjonselektronmikroskopi (TEM). Målet med studiet var å relatere presipitatstatistikk, morfologi og krystallstruktur med legeringens makroskopiske egenskaper, mer spesifikt hardheten. Liknende studier har blitt gjort på denne legeringen tidligere, men da på deformerte materialer. Varmebehandling ble gjennomført med og uten naturlig elding (lagring ved romtemperatur). To prøver ble lagret ved romtemperatur i 20 timer før de ble plassert i en ovn for kunstig eldning, mens to prøver var plassert i ovnen direkte. Den kunstig eldningstiden var enten 6 timer (undereldet) eller 48 timer (utherdet til maks styrke) for disse prøvene. Disse fire tilstandene ble undersøkt med TEM. Lysfeltsavbildning, mørkefeltsavbildning og konvergent elektrondiffraksjonsavbildning ble brukt for å samle presipitatstatistikk og studere morfologien til presipitatene. Høyoppløst TEM (HRTEM), høyvinkel annulær mørkefeltsveipetransmisjonselektronmikroskopi (HAADF-STEM), og sveipepresesjonselektrondiffraksjon (SPED) ble brukt for å undersøke krystallstrukturen i presipitatene. SPED ble også brukt for å kartlegge tøyning i materialet rundt presipitatene.

Det ble vist at tilstandene med naturlig elding hadde lavere hardhet. Dette er kjent som den negative effekten av naturlig elding og det var spesielt tydelig i de undereldede tilstandene. Dette ble relatert til en lavere volumfraksjon av presipitatene, i tillegg til lavere antallstetthet og kortere lengder. Størrelsesforholdet av tversnittsarealet til presipitatene ble målt og resultatene viste at tilstandene med naturlig elding hadde mer plankeformede presipitater, mens tilstandene uten naturlig elding hadde mer sylinderformede presipitateter. I tillegg ble det i tilstandene med naturlig elding funnet at størrelsesforholdet økte når tversnittsarealet økte. Resultatene fra faseidentifikasjon med HRTEM, HAADF-STEM og SPED viste at L fasen dominerte i tilstandene som ble utherdet til maks styrke, bortsett fra to β'' presipitater som ble funnet ved nærmere analyse av SPED-dataene. Kartlegging av tøyning viste en tydelig forskjell i tøyningsfeltene rundt L fasen og β'' fasen.

Preface

This thesis concludes my Master of Science Physics degree at the Department of Physics of the Norwegian University of Science and Technology (NTNU). The thesis was written in collaboration with the Japanese company Yoshida Kōgyō Kabushiki-gaisha (YKK) and the INTPART project. I am grateful to YKK for the samples used in this project. The experimental work presented in this thesis was carried out at several laboratories owned by the Department of Physics and the TEM Gemini Centre at NTNU. This work was supervised by Dr. Sigurd Wenner at SINTEF and Professor Randi Holmestad.

Many people have helped me through this journey, and I owe them my gratitude. I would first like to thank Dr. Sigurd Wenner for being my main supervisor in practice. Thank you for your invaluable guidance and feedback throughout this past year and a half. Thank you for acquiring the SPED datasets and HAADF-STEM images for me to analyze, and for teaching me techniques on the TEM. Thank you to Professor Randi Holmestad for acting as my co-supervisor, in addition to giving feedback and support. I would like to thank Elisabeth Thronsen for designing the beginning of my project and answering my questions about YKK, SPED, and the alloy. A great thank you to Bjørn Gunnar Soleim and Emil Frang Christiansen for educating me on how to use the TEM and coming to my aid when the TEMs gave me trouble. A special thanks to Emil for teaching me and answering my questions about SPED, HyperSpy, and PyXem. Thank you to Christoph Hell for showing me how to measure thickness with CBED and often checking up on me to see how I was doing. I would also like to thank Dipanwita Chatterjee for helping me understand the strain Jupyter Notebook. I am so grateful to my boyfriend Johan Magnus Krosby for giving feedback on my thesis and for the immense support he has given me throughout this past year. Last, but not least, I am grateful for the support from my friends and family, especially my parents.

I look forward to the next chapter in my life, which will be to work at Hydro Aluminium AS in Sunndalsøra where I will continue to work with aluminium.

List of Acronyms

ADF	Annular Dark Field
AA	Artificial Ageing/Artificially Aged
BF	Bright Field
BFP	Back Focal Plane
CA	Condenser Aperture
CBED	Convergent Beam Electron Diffraction
CL	Condenser Lens
CoM	Center of Mass
CS	Cross-Section (Area)
CTF	Contrast Transfer Function
DA	Direct Ageing/Directly Aged
DF	Dark Field
DL	Diffraction Lens
DP	Diffraction Pattern
EDS	Energy Dispersive Spectroscopy
EELS	Electron Energy-Loss Spectroscopy
EM	Electromagnetic
FCC	Face Centered Cubic
FFT	Fast Fourier Transform
FEG	Field Emission Gun
GMS	Gatan Microscopy Suite
GP	Guinier-Preston
HAADF	High Angle Annular Dark Field
HREM	High Resolution Electron Microscope/Microscopy
HRTEM	High Resolution Transmission Electron Microscope/Microscopy
IFFT	Inverse Fast Fourier Transform
IL	Intermediate Lens
NA	Natural Ageing/Naturally Aged
NBD	Nano Beam Diffraction
NN	Nearest Neighbour
NMF	Non-negative Matrix Factorization
OA	Objective Aperture
OL	Objective Lens
OPNN	Opposite Plane Nearest Neighbour
PED	Precession Electron Diffraction
PL	Projector Lens
RT	Room Temperature
SA	Selected area Aperture
SAD	Selection Area Diffraction
SAED	Selected Area Electron Diffraction
SEM	Scanning Electron Microscope/Microscopy

SHT	Solution Heat Treatment
SPED	Scanning Precession Electron Diffraction
SSSS	Super Saturated Solid Solution
STEM	Scanning Transmission Electron Microscope/Microscopy
SVD	Singular Value Decomposition
SVG	Scalable Vector Graphics
TEM	Transmission Electron Microscope/Microscopy
VA	Virtual Aperture
VBF	Virtual Bright Field
VDF	Virtual Dark Field
VF	Volume Fraction
VLM	Visual-Light Microscope
WQ	Water Quench
YKK	Yoshida Kōgyō Kabushiki-gaisha

The nomenclature for the four different TEM conditions investigated in this thesis.

Designation	**0-48**	**20-48**	**0-6**	**20-6**
NA time	0 h	20 h	0 h	20 h
AA time	48 h	48 h	6 h	6 h

Chemical elements are referred to by their abbreviations, as given in the periodic table.

Contents

1 Introduction

Aluminium is an important part of the Norwegian metal industry and is Norway's third-largest export [1]. Aluminium compounds were known in various industries throughout history, such as a reddish-brown rock known as bauxite from which alumina (Al_2O_3) could be extracted. The credit for first isolating pure aluminium was given to Hans Christian Ørsted in 1825, but he only managed to produce a small amount. Since aluminium was challenging to produce, it was more valuable than gold in the mid-1800s. This changed when Charles Martin Hall and Paul Héroult independently developed a way to extract pure aluminium from alumina using electrolysis, which became known as the Hall-Héroult process. The industrialization of the aluminium industry caused the prices to drop, where the cost lay under \$2 per kg by 1891 [2].

Since aluminium is a soft metal, small quantities of other elements can be added to create alloys, which can increase strength, ductility, castability, or workability [3]. At the start of the 1900s, Alfred Wilm was testing the hardness of aluminium alloys after quenching from a high temperature and let a sample rest at room temperature while he went sailing for two days. Upon his return, he discovered that the alloy's hardness and tensile properties had increased while he was gone. The discovery of "age hardenable" alloys baffled the scientific community [4]. It was not before 1938 that André Guiner and George Dawson Preston proved that precipitates at nanoscale were the cause of this hardening. The connection between the alloy's microstructure and its properties became important because by performing detailed nanoscale characterization, it was possible to improve an alloy's properties even more [5].

A powerful tool for studying precipitates is the transmission electron microscope (TEM), which can provide atomic-resolution images of the material. Max Knoll and Ernst Ruska demonstrated the first TEM in 1931, and the first commercial TEMs were developed in 1936. In the mid-1950s, scientists were able to perfect their techniques that thinned metal foils down to electron transparency. Since the construction of the first TEM, the quality of TEMs has increased in terms of better resolution, detectors and user-friendliness. Other techniques with high resolution exist, such as scanning electron microscopy (SEM) for studying the surfaces of specimens [6]. However, it is not possible to detect the shape of the precipitates with SEM due to insufficient resolution. In addition, most precipitates are metastable and cannot exist outside aluminium, so TEMs are needed to see through aluminium [7].

Today, aluminium is used in countless products that are incorporated into our everyday lives, such as cooking equipment and soft drink cans [2]. The alloy studied in this thesis has been developed for zipper production by Yoshida Kōgyō Kabushiki-gaisha (YKK) together with Toyama university and its composition is Al-1.27Cu-1.01Mg-0.38Si (all values in wt.%). During the production of zippers, it is normal and unavoidable to store the alloys at room temperature, a process called natural ageing. The effect of natural ageing on this alloy has been studied before where the material was heavily deformed, but the undeformed case has not been studied in great detail [8, 9, 10, 11]. The natural ageing time used in those studies was 20 h (the time used in the industrial process), 18 h and five days (120 h), so the alloy's response to other natural ageing times is unknown. Therefore, this thesis aims to understand the effect of different natural ageing times on precipitate evolution without deformation and study how this affects the alloy's final properties. More specifically, the study aims to quantify precipitates

by measuring their length, cross-section area and number density, thereby calculating their volume fraction. Precipitate morphology and crystal structure are analyzed as well. These characteristics are significant because they influence the alloy's microstructure, which affects its macroscopic properties. This investigation is done with the help of varying TEM techniques. The hope is that this work will assist in developing better materials for zippers in the future.

The layout of the thesis is given as follows: Chapter 2 consists of an overview of the theory needed to understand the motivation of the thesis, the experimental methods used and the acquired results. Chapter 3 presents the material and experimental methods employed in the thesis. The results are introduced in Chapter 4, which are discussed in Chapter 5 in relation to the theory in Chapter 2 and previous work. The conclusion in Chapter 6 provides a summary of the findings and Chapter 7 explores further work that can be done. The Appendices contain supporting results, an explanation of the SPED calibration procedure and lastly, the Jupyter Notebooks that were utilized in this thesis.

2 Theory

2.1 Crystallography

A *crystal* is defined as a periodic arrangement of individual atoms or a group of atoms. If the arrangement is repeated infinitely, it makes up what is known as an *ideal crystal*. The repeated identical groups of atoms, ions or molecules are called the *basis*. The *lattice* is a set of discrete and mathematical points to which the basis is coupled to. Most lattices can be described as a convolution between a basis and a lattice. An example of this is illustrated in Figure 2.1. This section stems from *Introduction to Solid State Physics* by Charles Kittel [12] and is used as reference unless stated otherwise.
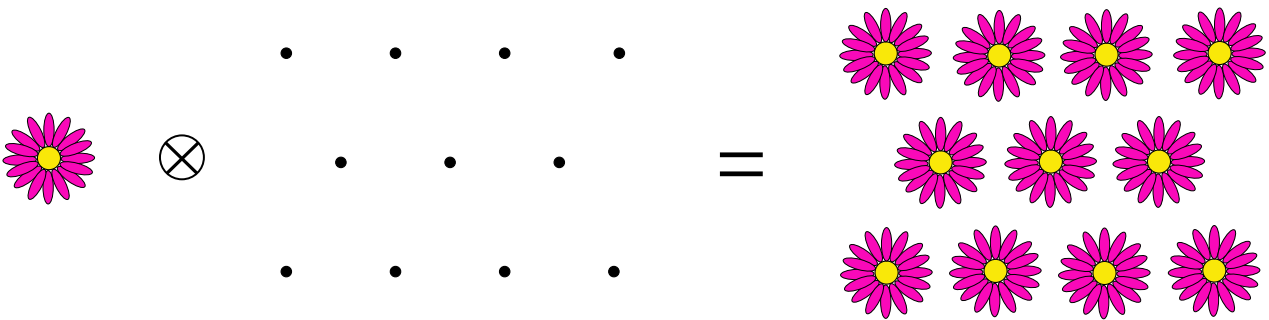

Figure 2.1: A crystal structure formed by a convolution between a basis and a lattice. Adapted from [12].

2.1.1 The Lattice

One can define the lattice in three dimensions with three translation vectors, $\mathbf{a}_1$, $\mathbf{a}_2$, $\mathbf{a}_3$ such that the array of atoms in the crystal looks identical when seen from a point $\mathbf{r}$ as when seen from every point $\mathbf{r}'$ shifted by an integral multiple of $\mathbf{a}_1$, $\mathbf{a}_2$, $\mathbf{a}_3$:

$$\mathbf{r}' = \mathbf{r} + u_1\mathbf{a}_1 + u_2\mathbf{a}_2 + u_3\mathbf{a}_3, \tag{2.1}$$

where u_1, u_2, u_3 are arbitrary integers. The lattice can then be defined by the set of points $\mathbf{r}'$ for all u_1, u_2, u_3. The lattice is called a *primitive lattice* if any two locations look identical and always satisfy equation (2.1) for selected integers u_i. The *primitive lattice cell* is then built upon the *primitive translation vectors* $\mathbf{a}_i$. Therefore, the cell has a volume of $\mathbf{a}_1 \cdot \mathbf{a}_2 \times \mathbf{a}_3$ and is the smallest possible volume that can act as single identical building blocks filling all of 3D space with the crystal structure. The primitive translation vectors $\mathbf{a}_i$ are frequently used to define the *crystal axes*, which generally make up the three adjacent edges of a primitive parallelepiped. Once the crystal axes are selected, the basis can be determined. The distance from the center of an atom j of the basis to a point on the lattice can be described by the lattice vector,

$$\mathbf{r}_j = x_j\mathbf{a}_1 + y_j\mathbf{a}_2 + z_j\mathbf{a}_3, \tag{2.2}$$

where $0 \leq x_j, y_j, z_j \leq 1$. This is because the associated lattice point (the origin) can always be relocated to fit this criterion. The basis which contains the smallest number of atoms, ions or

molecules possible is called the *primitive basis*.

A useful quality of crystal lattices is that they can be mapped onto themselves by lattice translation operations or other various symmetry operations. Rotation about an axis that goes through a lattice point is a relevant symmetry operation, called rotational symmetry. Lattices can have one-, two-, three-, four-, and sixfold rotation axes that map the lattice onto itself, denoted by n where $n = 1, 2, 3, 4, 6$. These rotations are equivalent to rotating the lattice by $2\pi/n$ radians, and by an integral multiple of this. Another important symmetry operation is mirror reflections denoted by m, where a mirror plane is a plane that goes through a lattice point. Lastly, the rotation-inversion, only found in three dimensions or more, denoted by $\bar{n}$, consists of a rotation n succeeded by an inversion through an inversion center point. Combining different operations and applying them to a lattice point to map the lattice onto itself, is called a *point group* and there are 32 different types.

In three dimensions, restrictive conditions must be imposed on the crystal axes $\mathbf{a}_1$, $\mathbf{a}_2$, $\mathbf{a}_3$ if the requirement is a lattice that is invariant under one or more symmetry operations. This results in a collection of *Bravais lattices* shown in Table 2.1. There are 14 unique types of Bravais lattices. They are categorized by the length of the edges of the cell, i.e. $||\mathbf{a}_1||$, $||\mathbf{a}_2||$, $||\mathbf{a}_3||$, and the angles between them α, β, γ. The cubic system is especially important since it is one of the most common and has three distinct Bravais lattices, which are shown in Figure 2.2. When combining the 32 point groups with the 14 Bravais lattices, one can form 230 different *space groups*.

Table 2.1: The 14 Bravais lattice types in three dimensions. Obtained from [12].

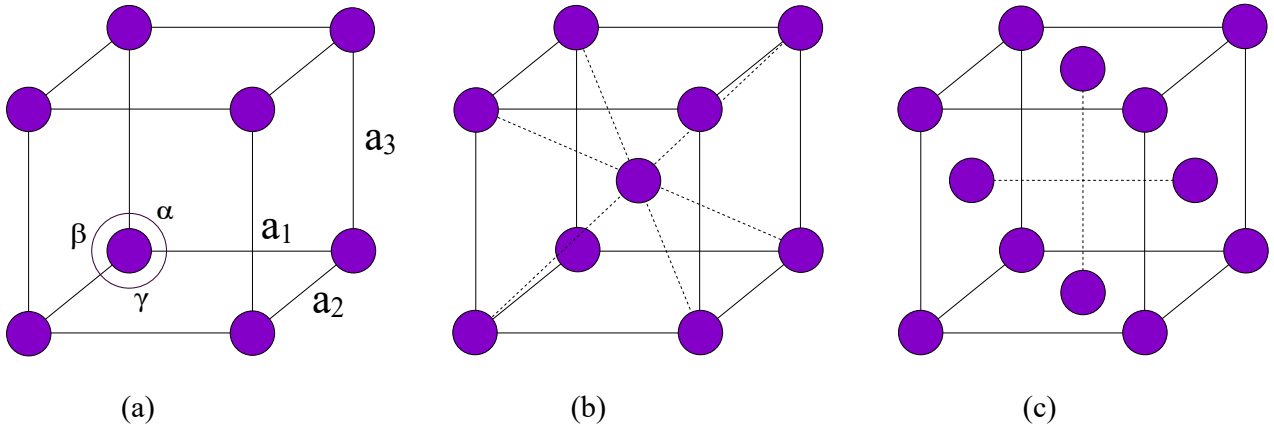| System	Number of lattices	Restrictions on conventional cell axes and angles
Triclinic	1	$a_1 \neq a_2 \neq a_3$ $\alpha \neq \beta \neq \gamma$
Monoclinic	2	$a_1 \neq a_2 \neq a_3$ $\alpha = \gamma = 90° \neq \beta$
Orthorhombic	4	$a_1 \neq a_2 \neq a_3$ $\alpha = \beta = \gamma = 90°$
Tetragonal	2	$a_1 = a_2 \neq a_3$ $\alpha = \beta = \gamma = 90°$
Cubic	3	$a_1 = a_2 = a_3$ $\alpha = \beta = \gamma = 90°$
Trigonal	1	$a_1 = a_2 = a_3$ $\alpha = \beta = \gamma < 120°, \neq 90°$
Hexagonal	1	$a_1 = a_2 \neq a_3$ $\alpha = \beta = 90°, \gamma = 120°$

Figure 2.2: The three cubic Bravais lattices: (a) simple cubic, (b) body-centered cubic, (c) face-centered cubic. Adapted from [12].

2.1.2 Index System for Crystal Planes

To determine the orientation of planes in a crystal, one can use three points in the plane as long as they don't lie along the same line. Let each point lie on a different crystal axis $\mathbf{a}_i$, such that the orientation of the plane can be described by the *Miller indices* which follow the following rules. First, find where the plane intersects the axes in terms of the unit cell edges a_1, a_2, a_3. Secondly, take the reciprocal of the three numbers and reduce them to the lowest three integers that have the same ratio. These three integers, denoted by (hkl), are called the Miller indices which give the index of the plane or the set of parallel planes. Planes that intersect the axes on the negative side of the origin are denoted by a bar above the index, like $(h\bar{k}l)$. If the plane does not intercept an axis, or intercepts at infinity, its reciprocal is 0. The *d-spacing* is defined as the interplanar spacing between the equivalent (hkl) planes and for a cubic crystal it is given by,

$$d_{hkl} = \frac{a}{\sqrt{h^2 + k^2 + l^2}},\tag{2.3}$$

where a is the length of the edges of the cubic unit cell, also called the *lattice parameter*. Directions in a crystal can be described by a vector from the origin of the crystal lattice to the point (ua_1, va_2, wa_3), denoted by $[uvw]$. The direction of the line formed from two intersecting crystal planes is called the *zone axis*. When the zone axis $[uvw]$ is perpendicular to the (hkl) plane (which is the case for cubic systems), then

$$hu + kv + lw = 0,\tag{2.4}$$

which is known as the *Weiss zone law*.

2.1.3 Reciprocal Lattice

This section will focus on the dual of real space, which is the *reciprocal space*. A real space crystal lattice can be described by a periodic function. Performing the Fourier transform of this periodic function will give another periodic function associated with the crystal lattice in reciprocal space. It is also possible to take the inverse Fourier transform of the reciprocal periodic function to go back to

the real space periodic function. A point in reciprocal space represents a collection of crystal planes in real space. Reciprocal space is therefore useful for describing planes, while real space is useful for describing directions. The crystal lattice in reciprocal space is called the *reciprocal lattice*, and it can be defined by the reciprocal lattice vector:

$$\mathbf{G} = m_1\mathbf{b}_1 + m_2\mathbf{b}_2 + m_3\mathbf{b}_3. \tag{2.5}$$

Here m_1, m_2, m_3 are integers and $\mathbf{b}_1$, $\mathbf{b}_2$, $\mathbf{b}_3$ are the *primitive reciprocal lattice* vectors. These vectors $\mathbf{b}_i$ have the property,

$$\mathbf{b}_i \cdot \mathbf{a}_j = 2\pi\delta_{ij} \ (j = 1, 2, 3), \tag{2.6}$$

where $\mathbf{a}_i$ are the primitive real lattice vectors and δ_{ij} is the Kronecker delta. The reciprocal lattice vector that corresponds to the Miller indices (hkl) of a crystal plane is given by,

$$\mathbf{g}_{hkl} = h\mathbf{b}_1 + k\mathbf{b}_2 + l\mathbf{b}_3. \tag{2.7}$$

The d-spacing from equation (2.3) and the length of the reciprocal lattice vector $\mathbf{g}_{hkl}$ are associated through this relationship:

$$||\mathbf{g}_{hkl}|| = \frac{2\pi}{d_{hkl}}. \tag{2.8}$$

2.1.4 Defects

This section is based on Chapter 4 of *Materials Science and Engineering* by Callister and Rethwisch [13]. Thus far, ideal crystals have been introduced and discussed, but in reality, they do not exist. Instead, crystalline solids contain various imperfections or *defects*, more specifically lattice irregularities of one or more dimensions. Since real crystals are not infinitely large, they have an external surface leading to surface defects. In addition, bulk or volume defects affect the material on a larger scale resulting in, e.g., pores and cracks. Defects can influence the properties of a material, for example, they play an important role in the strengthening of aluminium.

Figure 2.3 shows some examples of defects in a crystal lattice which give rise to mechanical hardening in metals. A point defect occurs at one or two atomic positions, for example, if an impurity atom replaces one of the host atoms in the lattice. This type of point defect is called a *substitutional solute atom* or *substitutional impurity atom* (A). When several solute atoms substitute the host atoms close to each other, they form a cluster (B). Another type of point defect occurs when a lattice site that is usually occupied is vacant, called a *vacancy* (D). Other varieties of defects include linear, interfacial, and bulk defects. An example of a linear defect is a *dislocation*, where some atoms have been displaced so the lattice planes do not match up (C). Dislocations occur in crystalline materials during solidification, plastic deformation or during rapid cooling due to thermal stresses. An important type of bulk defect is *precipitates* (E), which is a phase with another crystal structure compared to the host lattice. This will be addressed in greater detail in Section 2.2.3. Interfaces (or interfacial defects) are two-dimensional boundaries that usually separate areas in the material that have dissimilar orientations and/or crystal structure. A grain boundary is an appropriate example of this (F).
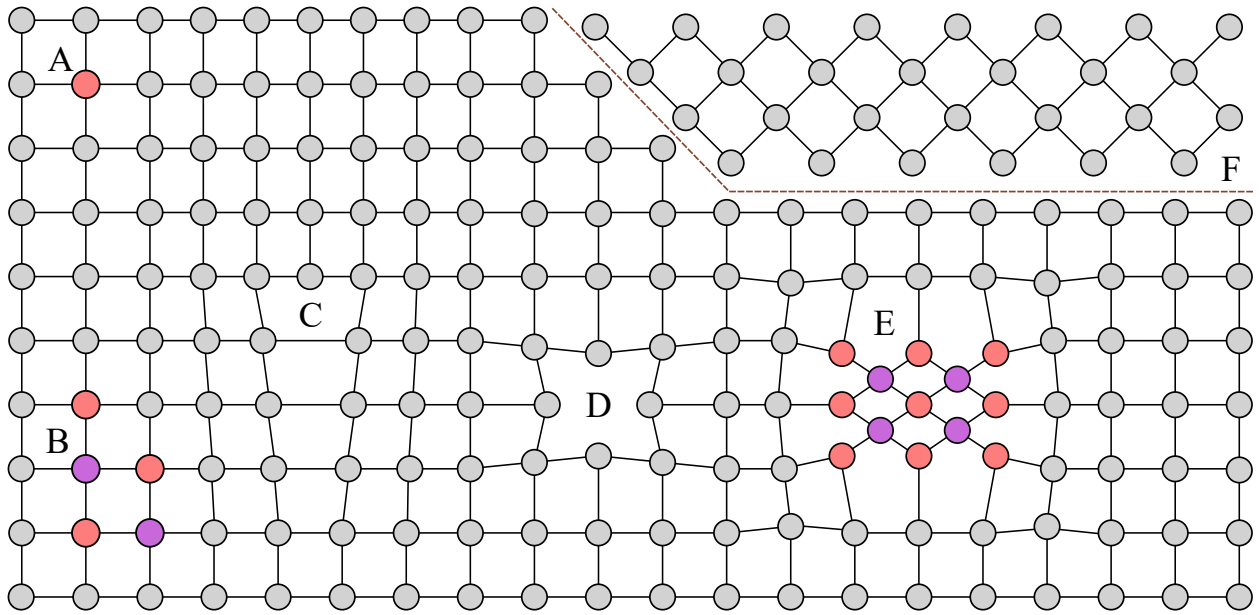
6

Figure 2.3: Illustration of different types of defects in a crystal lattice. A: solute atom, B: cluster of solute atoms, C: dislocation, D: vacancy, E: precipitate, F: grain boundary. Adapted from [14].

2.2 Aluminium

2.2.1 Introduction to Aluminium and Its Alloys

Aluminium is the second most abundant metallic element on earth [15]. It has an atomic number of 13 and has a face-centered cubic (FCC) crystal structure. This structure is stable from $4\,\mathrm{K}$ to its melting point $933.47\,\mathrm{K}$ [16]. The density of aluminium is $2.70\,\mathrm{gcm^{-3}}$ which is roughly a third of the density of steel [3]. A few selected properties of pure aluminium are presented in Table 2.2.

Table 2.2: Selected properties of pure aluminium at standard pressure and temperature. Data obtained from [17, 18].

Properties	Value
Atomic number	13
Lattice constant	$4.05\,\text{Å}$
Density	$2.70\,\mathrm{gcm^{-3}}$
Melting point	$660.32\,^{\circ}\mathrm{C}$
Appearance	Silvery-white
Electrical conductivity	$38 \times 10^6\,\mathrm{S\,m^{-1}}$
Thermal conductivity	$235\,\mathrm{W\,m^{-1}\,K^{-1}}$
Crystal structure	FCC

The production of pure aluminium requires a high amount of energy [3]. Alumina (Al_2O_3) is first extracted from the mineral bauxite. It is then melted and reduced to pure aluminium through electrolysis. This process is known as the Hall-Héroult process and has the chemical reaction equation [2]:

$$2Al_2O_3 + 3C \rightarrow 4Al + 3CO_2, \tag{2.9}$$

where the two reactions at the cathode and anode are:

$$Al_3^+(\text{melt}) + 3e^- \rightarrow Al(l), \tag{2.10}$$

and

$$2O_2^-(\text{melt}) + C(s) \rightarrow CO_2(g) + 4e^-, \tag{2.11}$$
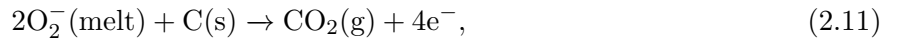
respectively. Aluminium has good corrosion resistance due to an inert layer of aluminium oxide covering the surface of the body of metal. This is because aluminium oxide is more stable than pure aluminium [3]. When the surface layer is damaged, it heals quickly since pure aluminium reacts with oxidants forming a new layer of aluminium oxide during a very short time [16]. The effects of corrosion on aluminium alloys are dependent on their chemical composition, their fabrication process and their heat treatment [3].

Aluminium is a soft metal, so different techniques have been developed to increase its strength. One of them is to make alloys by adding other elements in small quantities to pure aluminium. The main alloying elements are magnesium, silicon, copper, zinc, and manganese. These elements contribute with certain properties, for example, increased strength or increased corrosion resistance. Aluminium

alloys can be categorized according to which fabrication process they went through: casting alloys or wrought alloys [3]. Casting refers to filling moulds with molten aluminium [15]. Wrought alloys undergo hot- or cold-rolling processes such as extrusion, rolling or drawing without being remelted. Aluminium alloys can also be differentiated based on whether their strength increases through heat treatment or not. They are either heat treatable alloys or non-heat treatable alloys, also known as work-hardenable alloys. Table 2.3 lists the unique wrought alloy families, their primary alloying elements, their heat treatability and typical areas of application. A number consisting of four digits is used to organize wrought alloys into families (see Table 2.3), where the first digit represents which primary alloying elements they have [3].

Table 2.3: The distinct wrought aluminium alloys, their primary alloying elements, typical areas of application and their heat treatability [15].

Alloy family	Primary Alloying Elements	Heat Treatable?	Typical areas of application
1xxx	None	No	Electrical and chemical industries
2xxx	Cu, (Mg)	Yes	Aircraft industry
3xxx	Mn	No	Architectural applications, general-purpose alloy
4xxx	Si	No	Welding rods and brazing sheets
5xxx	Mg	No	Marine industry
6xxx	Mg, Si, (Cu)	Yes	Architectural applications
7xxx	Zn, (Cu), (Mg), (Cr), (Zr)	Yes	Aircraft industry, other high-strength applications
8xxx	Sn, (Li), various	Yes	Various

2.2.2 Strengthening Mechanisms

The level to which a material deforms depends on the amount of stress and force applied to it. *Deformation* can be classified into two types when exposed to mechanical stress: *plastic* deformation and *elastic* deformation. Elastic deformation occurs when the material returns to its original shape after the applied force is released, so it is non-permanent. Plastic deformation is permanent, so the original shape cannot be recovered. If a material has experienced a large extent of permanent deformation, fractures occur. The strength and hardness of a material are given by its resistance to plastic deformation. In most crystalline materials, the motion of dislocations is what causes plastic deformation, a process called *slip*. This means that strengthening mechanisms depend on restricting and hindering the dislocations' ability to move. The *slip plane* is the plane along which the dislocation line moves. The direction in which they move is called the *slip direction*. For aluminium, which has an FCC crystal structure, its slip plane is the {111} family of planes and its slip direction is the ⟨110⟩-type [13].

The main strengthening mechanisms for metals like aluminium are *grain size reduction*, *solid-solution strengthening*, *strain hardening* and *precipitation hardening*. It is possible to utilize more than one mechanism at a time. The first mechanism takes place because the size of the grains in a metal affects its mechanical properties. For example, let two adjacent grains A and B share a common grain boundary. During slip, the dislocation has to travel across the common grain boundary from grain A to grain B. The grain boundary functions as an obstacle for the dislocation motion for two reasons. The first reason is that the dislocation has to change its direction from grain A to grain B. The second reason is that the slip planes are discontinuous across the grain boundary due to the atomic disorder there. A material that has small grains (fine-grained) and therefore a greater total grain boundary volume to hinder slip, is harder and stronger than a coarse-grained material. This is why grain-size reduction is a strengthening mechanism [13].

As mentioned in the previous section, introducing impurity atoms to the solid solution is a method to increase hardness and strength, called solid-solution strengthening. When the impurity atoms replace the host atoms either substitutionally or interstitially, they cause lattice strains on the host atoms around them. The lattice strain field interactions between the dislocations and the alloying elements result in resistance to slip because the overall lattice strain increases if a dislocation is separated from impurity atoms [13]. One should note that solid-solution strengthening is more prominent in aluminium when the concentration of alloying elements is lower, and less effective for higher concentrations [19].

Strain hardening is a strengthening mechanism that occurs when a metal's strength and hardness increases under plastic deformation. It is also called *work hardening* or *cold working* because the operating temperature is "cold", usually room temperature, in comparison to the absolute melting temperature of the metal. Increasing the amount of plastic deformation increases the density of dislocations in the metal, meaning that the average separation distance between them decreases. Since dislocation-dislocation strain field interactions are repulsive on average, the dislocation motion is obstructed by other dislocations [13]. Non-heat treatable alloys are strengthened this way, normally by cold rolling [19]. The next section will address the last strengthening mechanism: precipitation hardening.

2.2.3 Heat Treatment and Precipitation Hardening

A phase is defined as a part of a system that has homogeneous composition and properties, but is physically different from the remaining parts of the system. For example, in a metal alloy, the host matrix has the original phase while *precipitates* are small uniformly distributed particles consisting of a new phase. The phase transformation arises during heat treatment, a process called precipitation hardening or *age hardening*. Like other defects, precipitates hinder the propagation of dislocations in the matrix [13]. The precipitate-dislocation interaction depends mostly on the precipitate's size, spacing and coherency [19]. Coherency is defined at the end of this section. Dislocations can either *loop* around the precipitates leaving a closed dislocation loop, or cut them into two (also known as *shearing*). Shearing calls for a lot of energy when the spacing between precipitates is small, so an alloy with a high number density of small precipitates is therefore the strongest [12]. The metal alloy's

strength and hardness may increase as the alloy ages and precipitates form, which is why this process is a strengthening mechanism. However, if the alloy is overaged (meaning that it has aged for a longer time than necessary), it becomes softer and weaker because the resistance to slip is reduced [13].

To better understand heat treatments and precipitation hardening, a phase diagram of an Al-Cu system is presented in Figure 2.4. The same principles presented here applies to all precipitation hardening alloys. Note that this phase diagram is for a binary case, so increasing the number of solutes complicates the diagram [13]. In addition, this phase diagram only applies to an equilibrium case, while all precipitates are metastable and are not included here.
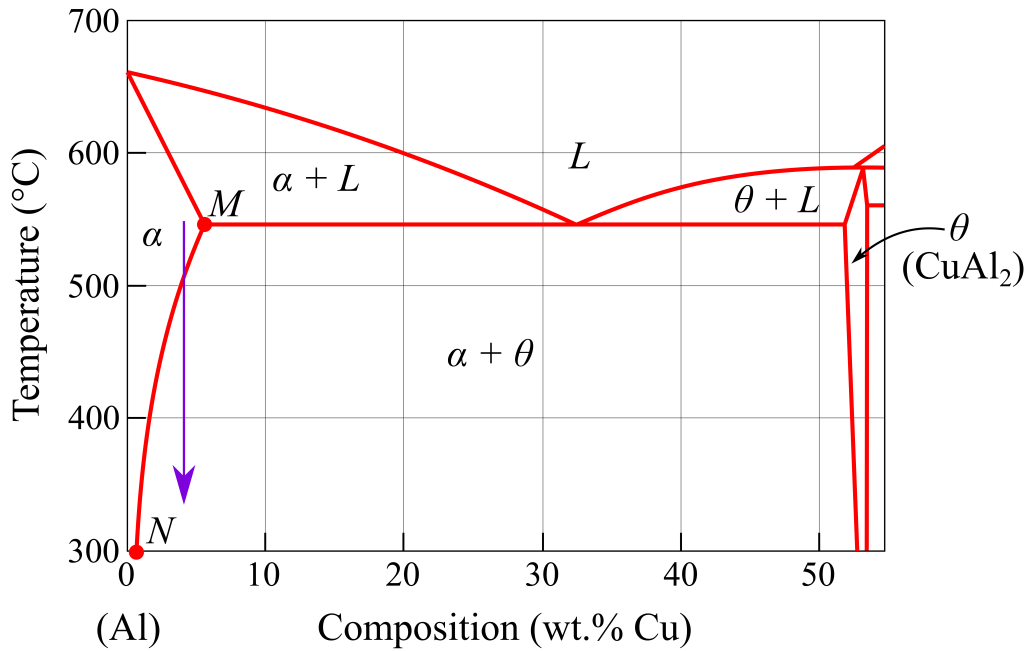
Figure 2.4: The aluminium-rich side of the binary Al-Cu phase diagram. Solution heat treatment generally occurs in the α region, and with water quenching, the phase transformation follows the vertical purple arrow down to the $\alpha + \theta$ region. Adapted from [13].

There are two requirements imposed on the phase diagram for precipitation hardening to occur. The first being that the maximum solubility of one phase must be several percent orders larger than the other. The second being as the temperature decreases, the major phase's ability to dissolve the other phases decreases rapidly. Both of these requirements are met in the Al-Cu phase diagram. The letter L represents the liquid phase, the α phase is a solid solution of Cu in Al, while the θ phase is the intermetallic compound $CuAl_2$. Point M corresponds to the maximum solubility limit. Point N represents the minimum solubility limit between α and $\alpha + \theta$ as the temperature and concentration of Cu decrease. In addition to these requirements, the alloy's composition is generally less than the maximum solubility for precipitation hardening to occur. Furthermore, two additional heat treatments are needed and are illustrated in Figure 2.5 [13].

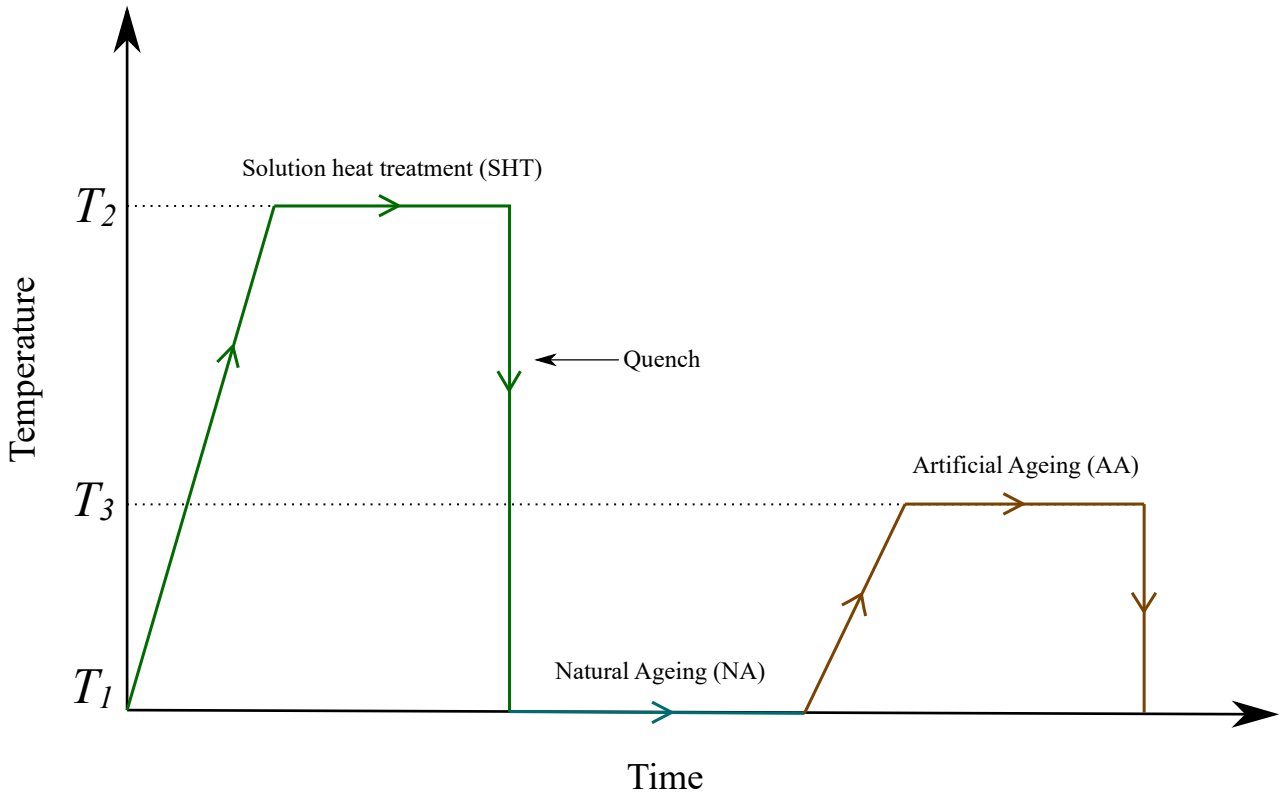Figure 2.5: Schematic temperature vs. time plot showing solution heat treatment, natural ageing, and artificial ageing for precipitation hardening. Adapted from [13].

Solution Heat Treatment

The first heat treatment is *solution heat treatment* (SHT) where the alloy is heated to a temperature T_2 that lies within the α region of the phase diagram (see Figures 2.4 and 2.5). Here the impurity atoms are dissolved into the host matrix to form a single-phase solid solution, which in this case is α. The material is then rapidly cooled or quenched to a temperature T_1, usually room temperature (RT) [13]. Quenching gives no time for a new equilibrium concentration to form, thereby freezing the solid solution such that a high concentration of vacancies becomes *quenched-in* [20]. Quenching also prevents coarse, incoherent precipitates that do not contribute to age hardening from forming [19]. After SHT, the solid solution is supersaturated with Cu, and the driving force to form the θ phase precipitates is the *vacancy pump mechanism* [20]. The vacancies in the matrix find impurity atoms and travel together as a diffusion pair until they find regions of higher solute concentrations, advancing substitutional diffusion. The vacancy then disconnects from the solute atom and repeats the process [20]. For aluminium alloys, SHT is typically done at temperatures >500 °C for a set time, typically 30 minutes.

Natural Ageing

After SHT, the alloy can rest at $T_1 = $ RT for natural ageing (NA) as shown in Figure 2.5. Most alloys' mechanical properties change after natural ageing, but the effect is dependent on their composition [21]. The *supersaturated solid solution* (SSSS) is not stable after SHT, due to the substitutional diffusion mentioned previously. The alloying elements diffuse through the matrix and form small clusters at RT [22]. The clusters generally serve as nucleation sites for later precipitation. The diffusion rate during

12

NA is slow, such that the single α phase in the Al-Cu system is preserved for a relatively long time. However, this process can be sped up with artificial ageing (AA) [13].

Artificial Ageing

The second heat treatment is *artificial ageing* (AA) where the alloy is heated to a temperature T_3 that lies between T_1 and T_2 (see Figure 2.5). For the Al-Cu system, this refers to the $\alpha + \theta$ region of the phase diagram in Figure 2.4, where the diffusion rate is substantial [13]. This is because the elevated temperature lowers the nucleation energy barrier, which accelerates precipitate nucleation [19]. With increasing AA time, the strength and hardness of the alloy increases until it reaches its maximum called *peak hardness*. After peak hardness, if the material is artificially aged any longer, the strength and hardness diminishes resulting in overageing [13]. After AA, the alloy is again quenched to a temperature $T_1 = \mathrm{RT}$ where it generally remains stable. If the alloy is artificially aged directly after SHT, the procedure is referred to as direct ageing (DA) [23]. For aluminium alloys, AA is typically done at temperatures between $150\,^{\circ}\mathrm{C}$ and $180\,^{\circ}\mathrm{C}$. The time to achieve maximum strength varies with composition and AA temperature, but it usually takes between a few hours and a day.
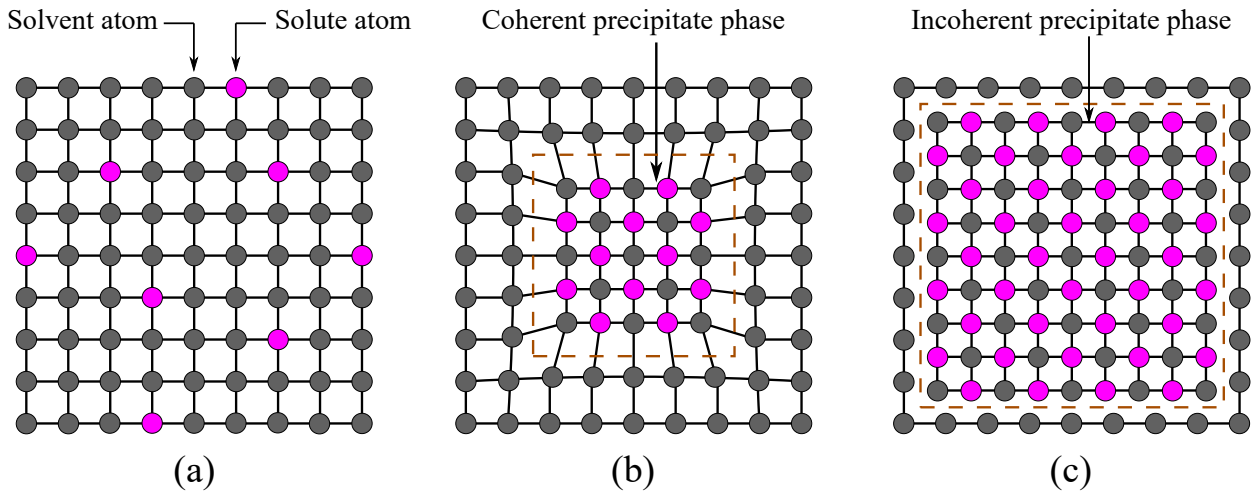
Figure 2.6: Parts of the precipitation sequence. (a) Random distribution of solute atoms in the host matrix under SHT. (b) A coherent precipitate phase formed under NA or AA. (c) An incoherent precipitate forms when the host matrix is not able to accommodate the lattice mismatch. Note that this is a simplified depiction since defects like vacancies have been neglected. Adapted from [13].

Figure 2.6 illustrates typical parts of the precipitation sequence during heat treatment on an atomic scale. This depiction is simplified since defects like vacancies are neglected. Figure 2.6(a) shows the random distribution of solute atoms in the host matrix during SHT. After SHT and during NA, the solute atoms will form small solute clusters in the lattice. When a solute cluster has sufficiently grown in size, either in the early stages of NA or AA, a coherent precipitate will often form. An example of this is shown in Figure 2.6(b), and here one can see a strain field on the surrounding matrix. For a fully coherent boundary, this occurs because the lattice planes get "bent" to fulfill the one-to-one matching of the lattice planes across the interface. Further ageing can lead to the cluster containing too many solute atoms, such that one-to-one matching is not possible across all boundaries, resulting in a semi-coherent precipitate. The difference in lattice parameters becomes too great, such that the

phases are not able to fit together. When the semi-coherent precipitate grows sufficiently large, the host matrix is not able to accommodate the lattice mismatch, creating incoherent precipitates. Phase transformations from a coherent phase to a semi-coherent or incoherent phase often occur as well. Incoherent precipitates are generally a stable, equilibrium phase with a weaker or no strain field on the surrounding matrix compared to coherent phases. Strain is discussed in further detail in Section 2.2.5.

2.2.4   Precipitates in Al-Mg-Si(-Cu) Alloys

There are different types of precipitate phases in the Al-Mg-Si(-Cu) system, but all of them have uniaxial morphology. They can have different shapes such as needles, laths, rods or plates which extend along the $\langle 001 \rangle$Al direction. The Si-columns in the $\langle 001 \rangle$Al direction are usually ordered in a projected hexagonal network with $0.4 \, \text{nm}$ spacing, called the Si-network [7]. Precipitates can therefore be regarded as different arrangements of atomic columns of Al, Mg, and/or Cu situated between the Si-columns. The number density, size and types of metastable precipitates in a material are dependent on the alloy composition and thermo-mechanical processing. This includes storage time, ageing time and temperature, heating and cooling rates, and deformation before ageing [24]. It was discovered that precipitates form in a sequence: the relative fractions of the different precipitate types change with increased AA time. Moreover, different precipitates form at different stages of ageing, for example, overaged compared to peak-age. To maximize a precipitate type's presence in a material, one must use its preferred alloy composition and heat treatment procedure. A precipitate type's preference is often unknown and must be found with *alloy design*. The precipitation sequence for an Al-Mg-Si system (Cu-free) is [25]:

$$\text{SSSS} \rightarrow \text{atomic clusters} \rightarrow \text{GP zones} \rightarrow \beta'' \rightarrow \beta', \text{U1, U2, B}' \rightarrow \beta, \text{Si,}$$

where β'', β', U1, U2, B$'$ and β are the different phases in this system. Guinier-Preston (GP) zones have similarities to a solute cluster because it is a region consisting of solute-rich atoms. These zones occupy Al FCC lattice positions, but have their own ordered structure [26]. GP-zones are formed after atomic clusters and provide structural stability for the following precipitates that form [27]. The β'' phase is the most efficient precipitate for strengthening 6xxx alloys, since it is particularly coherent with the Al matrix. During overageing, β'' evolves into coarser post-β'' phases, such as β', U1, U2 and B$'$ leading to a significant loss of strength [24]. An overview of the precipitate phases in a Al-Mg-Si system and their morphology are presented in Table 2.4.

Table 2.4: Overview of known precipitate phases in Al-Mg-Si alloys.

Phase	Shape	Space group	Reference
GP zones	Needle	$C2/m$	[25]
β''	Needle	$C2/m$	[25, 28]
β'	Rod	$P6_3$	[28]
U1	Needle	$P\bar{3}m1$	[25, 28]
U2	Needle	$Pnma$	[25, 28]
B$'$	Lath	$P\bar{6}$	[28]
β	Plate	$Fm\bar{3}m$	[25, 28]

Addition of Cu to Al-Mg-Si alloys can lead to increased strength in a material. This is due to Cu-containing alloys producing a high number density of short needles leading to finer precipitate microstructure. This results in high precipitate volume fraction and therefore greater interface strain that impedes dislocation movement. The precipitation sequence for an Al-Mg-Si-Cu system is [25]:

$$\text{SSSS} \rightarrow \text{atomic clusters} \rightarrow \text{GP zones} \rightarrow \beta'', \text{L, C, QP, QC} \rightarrow \beta', Q' \rightarrow Q,$$

where β'', L, C, QP, QC, β', Q$'$ and Q are the different phases in this system. The relative fraction of β'' is reduced by addition of Cu due to co-existing with other precipitate phases formed at peak hardness, e.g., the L and C phases. These phases evolve into β' and Q$'$ during overageing, and are followed by the stable Q phase [28]. Both the L and C phase have a $\langle 001 \rangle$ *habit plane* and are lath/plate shaped, so their cross-sections lie along the {100} Al planes. The L phase is believed to contribute significantly to increased hardness and thermal stability in Al-Mg-Si-Cu alloys [24]. It was proposed by Torsæter et al. that the L phase is a disordered version of the C phase but with lath morphology instead of plate morphology [29]. An overview of the precipitate phases in the Al-Mg-Si-Cu system and their morphologies are shown in Table 2.5.

Table 2.5: Overview of known precipitate phases in Al-Mg-Si-Cu alloys.

Phase	Shape	Space group	Reference
QP	Needle	Hexagonal	[25]
QC	Needle	Hexagonal	[25, 28]
C	Plate	Monoclinic	[28]
L	Lath	Disordered	[25]
Q$'$	Lath	$P\bar{6}$	[25, 28]
Q	Lath	$P\bar{6}$	[28]

2.2.5 Strain

Strain, ε, is a measure of the fractional displacement of an atom in a crystal lattice and is a dimensionless tensor. In a crystal with defects, like precipitates, atoms are displaced from their ideal lattice positions around the defects. The atomic displacement in three dimensions and Cartesian coordinates

is determined by the following vector:

$$\mathbf{u}(\mathbf{r}) = \mathbf{r}(x, y, z) - \mathbf{r}_0(x, y, z), \tag{2.12}$$

where $\mathbf{r}(x, y, z)$ and $\mathbf{r}_0(x, y, z)$ are the position vector of the displaced atom and the ideal lattice position atom, respectively [30]. The 3D strain is a tensor made up of 9 components defined by the first-order derivative of $\mathbf{u}(\mathbf{r})$'s components:

$$\varepsilon_{xx} = \frac{\partial u_x}{\partial x}, \quad \varepsilon_{yy} = \frac{\partial u_y}{\partial y}, \quad \varepsilon_{zz} = \frac{\partial u_z}{\partial z}, \tag{2.13}$$

and

$$\varepsilon_{xy} = \varepsilon_{yx} = \frac{1}{2} \left(\frac{\partial u_x}{\partial y} + \frac{\partial u_y}{\partial x} \right), \quad \varepsilon_{xz} = \varepsilon_{zx} = \frac{1}{2} \left(\frac{\partial u_x}{\partial z} + \frac{\partial u_z}{\partial x} \right), \quad \varepsilon_{yz} = \varepsilon_{zy} = \frac{1}{2} \left(\frac{\partial u_z}{\partial y} + \frac{\partial u_y}{\partial z} \right) \tag{2.14}$$

where the three components in equation (2.13) are the normal strains, which represent the fractional displacement lengths along the x-, y- and z-directions. The six components in equation (2.14) are the shear strains, which correspond to the shear angles and are measured in radians [30].

As mentioned previously, strain fields appear in the region of the interface between precipitate and matrix. For a coherent boundary, the strain energy is large because the one-to-one matching of lattice planes often requires relatively high atomic displacements. For semi-coherent and incoherent boundaries, the atomic displacements are not as high which leads to lower strain energy [31]. One can therefore deduce that a fully coherent precipitate phase like β'' induces a higher lattice strain on the host matrix than a semi-coherent phase like the L phase [32]. A loss of coherency in precipitates weakens the material since coherent boundaries are considered more effective at stopping dislocation motion [31].

2.2.6 Column Arrangement Principles of Al-Mg-Si(-Cu) Precipitates

Since Al has an FCC structure, the d-spacing for neighbouring (001) planes is 2.025 Å. Due to the 3D stacking of atoms, a $\langle 001 \rangle$ column is shifted by half a unit cell in the z-direction relative to its neighbouring columns. For that reason, one can assign all atomic columns a relative height of $z = 0$ or $z = \frac{1}{2}a_{\mathrm{Al}}$. For a fixed atom on a given plane, $\frac{1}{3}$ of its nearest neighbours (NN) lie in the same plane, while the remaining $\frac{2}{3}$ NN lie in the two opposite planes. These are deemed the opposite plane NN (OPNN). The NN column arrangement principles depend on the majority element of the column. The following principles can therefore determine the column species and height [33]:

1. Al FCC structure has 4-fold symmetry and has 12 NN. Therefore an Al column has 4 NN in the same plane, and two sets of 4 OPNN.

2. A Mg column generally has 15 NN, so 5 NN in the same plane and two sets of 5 OPNN.

3. A Si column has 9 NN, so 3 NN in the same plane and two sets of 3 OPNN.

4. A Cu column generally has the same principles as Si, but they are differentiated by Z-contrast.

Figure 2.7 gives an illustration of a fixed atom on either $z = 0$ or $z = \frac{1}{2}a_{Al}$ height with one set of its OPNN.
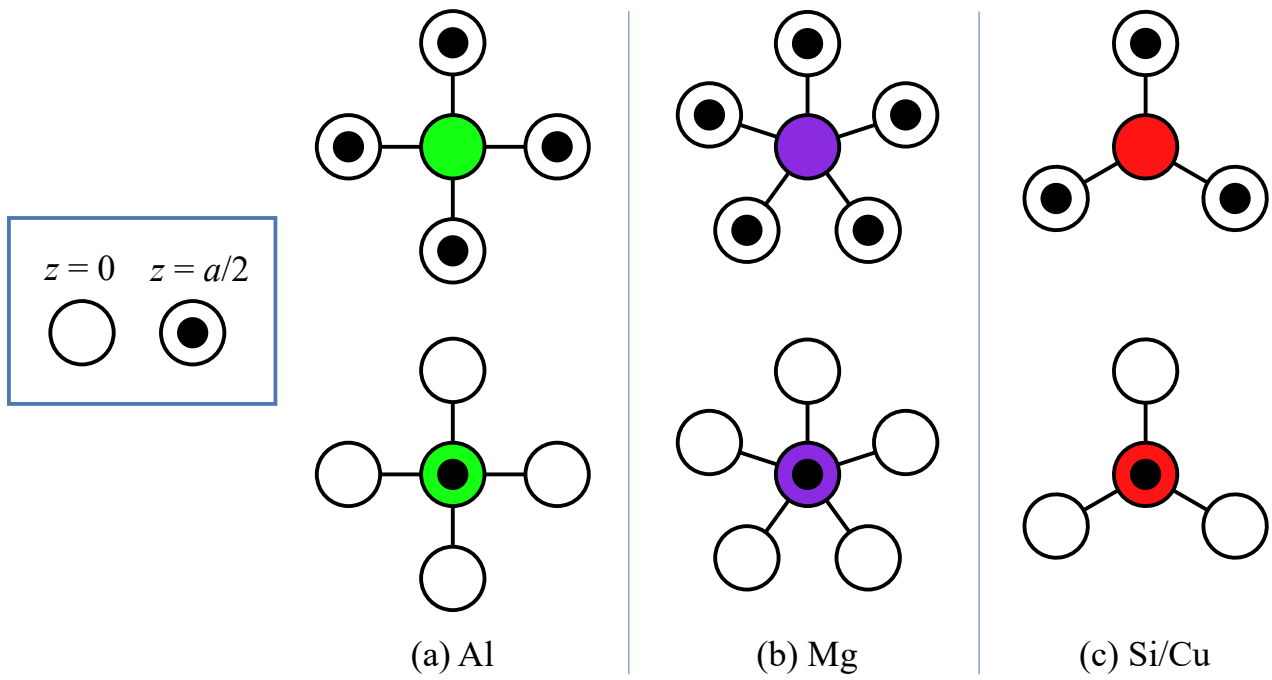

(a) Al   (b) Mg   (c) Si/Cu

Figure 2.7: An illustration of a fixed atom on a given plane with one set of its opposite plane nearest neighbours. (a) for Al, (b) for Mg, and (c) for Si/Cu, where z is the longitudinal displacement and a is the Al lattice constant $= 4.05\,\text{Å}$.

2.3 Transmission Electron Microscopy

Most of the content in this chapter is adapted from *Transmission Electron Microscopy: A Textbook for Material Science*, second edition by Williams and Carter (2009) [6] and is used as reference unless stated otherwise.

The first transmission electron microscope (TEM) was made in 1931. Several techniques to study materials and their structure already existed before that, e.g., X-ray diffraction and visual-light microscopes (VLM). However, there is a limitation to a VLM called the Rayleigh criterion, which decides the resolution of the image. It is given by,

$$\delta = \frac{0.61\lambda}{\mu \sin \beta}, \tag{2.15}$$

where δ is the shortest resolvable length, λ is the wavelength of the visual light wave, μ is the refractive index of the material, and β is the angle between the optical axis and the edge of the cone of light. β is also referred to as the *collection semi-angle*. Since it is within interest to study materials at a higher resolution, it was beneficial to find another method other than visual light to help humans see the microstructures. To get a better resolution δ, one thing that can change is decreasing the wavelength λ. After Louis de Broglie proposed that electrons behave as a wave and have their own wavelength, it was suggested to use electrons instead of visual light. Even though there are other options, like other particles and electromagnetic (EM) radiation, electrons have the advantage that they are charged particles and can therefore be manipulated by EM fields.

The TEM was developed, and its resolution can be approximated by,

$$\delta \sim \frac{1.22\lambda}{\beta} \text{ or } \frac{1.22}{\sqrt{E}}, \tag{2.16}$$

which is much less than δ for visual light. Louis de Broglie's equation for the wavelength of an electron is,

$$\lambda = \frac{h}{p}, \tag{2.17}$$

where h is Planck's constant and p is the electron's momentum $p = mv$. To give electrons momentum in a TEM an electric potential U is used. The electron then has a potential energy in electron volts eV, where $1\,\text{eV} = 1.602 \times 10^{-19}$ J. When all the potential energy has been converted to kinetic energy, the energies must be equal,

$$eU = \frac{1}{2}m_0 v^2, \tag{2.18}$$

here m_0 is the mass of the electron and v is the velocity of the electron. Rearranging equation (2.18) to isolate the velocity v, one can calculate the momentum:

$$p = m_0 v = (2m_0 eU)^{1/2}. \tag{2.19}$$

Putting this expression into equation (2.17) gives

$$\lambda = \frac{h}{(2m_0 eU)^{1/2}}, \tag{2.20}$$

which is the wavelength of the electron in the TEM for non-relativistic cases. For potentials $U > 100\,\text{kV}$, one has to take relativistic effects into account, so the adjusted wavelength becomes,

$$\lambda = \frac{h}{\left[2m_0 eU\left(1 + \frac{eU}{2m_0 c^2}\right)\right]^{1/2}}, \tag{2.21}$$

where $c = 299\,792\,458\,\text{m\,s}^{-1}$ is the speed of light. In TEM, it is normal to use accelerating voltages that lie between $100\,\text{kV}$ and $300\,\text{kV}$ which gives wavelengths between $0.0037\,\text{nm}$ and $0.0025\,\text{nm}$. This should give atomic resolution, but the resolution is still limited mainly by aberrations in the lenses and not the wavelength of the electrons. This is why spherical- and chromatic-aberration corrections are needed in the TEM. Apertures also limit the resolution since they affect the collection semi-angle β from equation (2.15).

2.3.1   Electron-Specimen Interaction

When electrons travel through the specimen in a TEM, several events occur. Electrons are charged particles, so they interact strongly with matter since the Coulomb forces are dependent on the charge. The most important aspect to remember about TEM specimens is that they have to be extremely thin. They have to be thin enough for electrons to pass through, usually from about $10\,\text{nm}$ to below $200\,\text{nm}$. This is because electrons have low penetration depth even for matter with a low atomic number, Z. Another aspect to take into account is that electrons can remove other electrons from the atoms in the specimen, a process called ionization. This results in an electron moving from a higher energy level to a lower energy level to replace the electron that was removed from the shell. The electron emits an X-ray photon which is dangerous in large amounts, so security measures must be taken when building and operating a TEM. For example, by building thick walls and making sure there are no radiation leaks. However, these X-rays can be detected to characterize materials.

A scattering event is defined by an object colliding with another object, for example, two electrons colliding. When discussing electron scattering, electrons will be treated as particles and not waves. One can have elastic scattering where the energy is conserved and inelastic scattering where the energy is not conserved. Usually, one differentiates between coherent- and incoherent scattering of electrons in the material as well. Coherence is defined by being in phase and having the same wavelength. Forward scattering is when electrons are scattered less than $90°$ and backscattering is when electrons are scattered more than $90°$. Thicker specimens result in more back-scattered electrons that are incoherent because the electrons struggle to travel through the bulk of the specimen more. Incoherent backscattering is utilized in *scanning electron microscopy* (SEM) and is useful since the signals give high contrast in images. Forward scattering generates signals that are useful for several TEM modes. The thickness of the specimen also determines how many scattering events can occur. If the specimen is thin enough, it might be possible to have a single scattering event resulting in kinematical diffraction. Thicker specimens will give rise to multiple scattering events resulting in dynamical diffraction.

One of the greatest advantages of TEM is the ability to obtain many signals simultaneously from the same area. In the TEM, it is normal to use the terms incident beam and scattered beam to denote the stream of electrons in the system. One of the benefits of using ionizing radiation is the secondary signals emitted from the specimen. Some of the events that can occur when the electron

beam goes through a thin specimen are summarized in Figure 2.8(a). The transmitted electrons are either scattered elastically or inelastically, and they have different applications. The direct beam is used for bright field (BF) imaging and the elastically scattered electrons are used for dark field (DF) imaging and electron diffraction. The inelastically scattered electrons are used for electron energy loss spectroscopy (EELS) and the characteristic X-rays are used for energy-dispersive X-ray spectroscopy (EDS). The different TEM modes are explained in greater detail in Section 2.3.4.
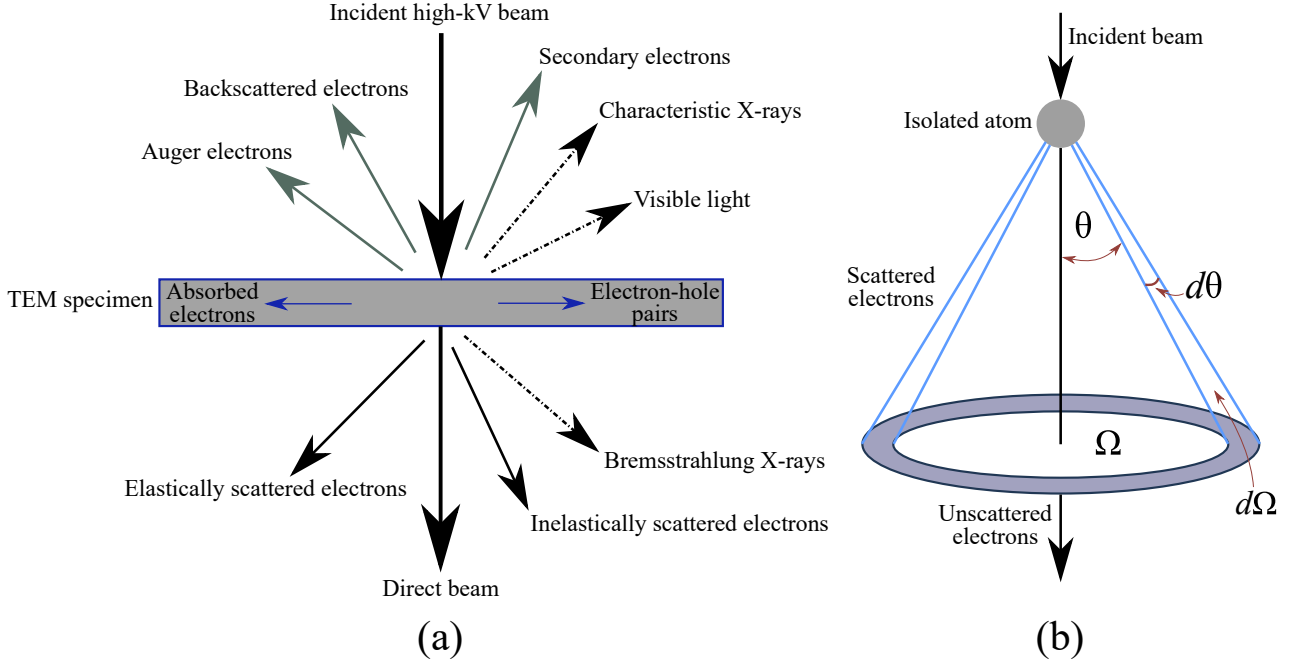

Figure 2.8: (a) Schematic showing the multitude of signals generated when a high energy beam of electrons interact with a TEM specimen. (b) Electrons scattering onto a single isolated atom. When the electrons scatter at a semi-angle θ, the solid angle is Ω. Increasing the scattering angle $d\theta$ results in an increased solid angle $d\Omega$. Both figures adapted from [6].

When the incident beam comes in contact with the specimen, it is useful to calculate where the scattered electrons will end up and the probability of this. This variable is called the *interaction cross-section* denoted by σ. To understand what σ is, study a simple case first: electrons scattering onto a single atom. The electrons that have been scattered at a semi-angle θ end up in an area defined by a solid angle Ω, see Figure 2.8(b). The relationship between θ and Ω is given by,

$$\Omega = 2\pi(1 - \cos\theta), \tag{2.22}$$

where for $\theta = 0$, no scattering occurs. Differentiating equation (2.22) gives

$$d\Omega = 2\pi \sin\theta d\theta. \tag{2.23}$$

One can see from Figure 2.8(b) that by increasing θ, integration will eventually result in a spherical shell. Dividing by $d\sigma$ on both sides and inverting the equation gives the expression for the differential scattering cross-section in the singular atom case:

$$\frac{d\sigma}{d\Omega} = \frac{1}{2\pi\sin\theta}\frac{d\sigma}{d\theta}. \tag{2.24}$$

In the TEM, it is interesting to check the distribution of electrons that stray from the angle θ and, therefore, the central mechanisms in the microscope, so integrating equation (2.24) from θ to π,

$$\sigma_{\text{atom}} = \int_{\theta}^{\pi} d\sigma = 2\pi \int_{\theta}^{\pi} \frac{d\sigma}{d\Omega} \sin\theta d\theta, \tag{2.25}$$

gives the distribution. For a high potential U and a thin specimen, most electrons are unscattered at $\theta = 0$ or scattered at an angle close to $\theta = 0$. In that case, one would integrate equation (2.25) from 0 to θ to get the distribution. Generalizing the expressions to a specimen related case, assume that the specimen has N atoms per unit volume. The total scattering cross-section is then given by,

$$\sigma_{\text{total}} = N\sigma_{\text{atom}} = \frac{N_0 \rho \sigma_{\text{atom}}}{A}, \tag{2.26}$$

where σ_{atom} is defined in equation (2.25), N_0 is Avogadro's number, A is the atomic weight of the atoms in the specimen and ρ is their density. The specimen will have a thickness t, which should be taken into account when calculating the scattering probability p. This can be written as such,

$$p = \frac{1}{\lambda} = t\sigma_{\text{total}} = \frac{N_0 \sigma_{\text{atom}}(\rho t)}{A}, \tag{2.27}$$

where σ_{total} is defined in equation (2.26), and λ is the mean free path of the electron travelling through the specimen, not the wavelength.

2.3.2   Diffraction

This section on diffraction is based on [12]. Diffraction is defined as "an interaction between a wave of any kind and an object of any kind" [34]. In this case, the wave consists of electrons and the object is the sample. Scattering of electrons was discussed previously where the electrons were treated as particles. In this discussion of diffraction, the electrons will be treated as waves. Diffraction is a useful tool as it can give information about the sample, more specifically about its crystal structure. The information that is possible to detect comes from the electron beams that have been diffracted from the crystal. Since a crystal is periodic, one can compare the parallel planes of atoms to a mirror, one that reflects poorly. With mirrors, the angle of incidence equals the angle of reflection. Assume that the parallel lattice planes have a d-spacing defined in equation (2.3), so the path difference is $2d\sin\theta$ for waves reflected from neighbouring planes. See Figure 2.9(a) for a simple illustration of this. When the waves reflect and interfere constructively, one can detect the diffracted beams. This occurs when the path difference is an integral number n of wavelengths λ, giving the *Bragg law*

$$n\lambda = 2d\sin\theta_{\text{B}}, \tag{2.28}$$

which is valid for $\lambda \leq d_{hkl}$. An equivalent alternative to the Bragg law is given by the *Laue conditions* which are more general and easier to work with when dealing with 3D lattices. This is the reciprocal space approach using the reciprocal lattice vectors $\mathbf{G}$ to determine the possible reflections. If $\mathbf{k}$ is the wavevector of the incident beam, and $\mathbf{k}'$ is the wavevector of the outgoing beam, then $\Delta\mathbf{k}$ is the difference between them. This can be written as

$$\mathbf{k} + \Delta\mathbf{k} = \mathbf{k}', \tag{2.29}$$

where $\Delta\mathbf{k}$ is also referred to as the scattering vector. The Laue condition is satisfied when

$$\Delta\mathbf{k} = \mathbf{G}, \tag{2.30}$$

in other words when the scattering vector equals the reciprocal lattice vector. The Laue equations come about when one takes the scalar product of the real lattice vectors and equation (2.30):

$$\mathbf{a}_1 \cdot \Delta\mathbf{k} = 2\pi h \quad ; \quad \mathbf{a}_2 \cdot \Delta\mathbf{k} = 2\pi k \quad ; \quad \mathbf{a}_3 \cdot \Delta\mathbf{k} = 2\pi l. \tag{2.31}$$

The three integer numbers h, k and l are the Miller indices of the parallel crystal planes mentioned earlier and $\Delta\mathbf{k}$ must meet all three equations for a diffraction spot to emerge. The *Ewald sphere* is a good visual representation of the Laue condition, see Figure 2.9(b). This sphere in reciprocal space has a radius equal to $2\pi/\lambda = |\mathbf{k}|$, where λ is the wavelength of the electrons. In Figure 2.9(b), the reciprocal lattice points are stretched out into reciprocal lattice roads, or relrods for short. This occurs because non-ideal crystals have a finite size, and for a TEM specimen, the extension of the lattice perpendicular to $\mathbf{k}$ is much greater than in the direction straight through the specimen where it is thinnest. The points of intersection between the Ewald sphere and the relrods give a new diffraction condition, increasing the number of diffraction spots even though the Bragg condition is not completely met. The deviation from the exact Laue condition can be described with the vector $\mathbf{s}$ known as the *deviation vector* or the *excitation error*. The relaxed Laue condition is then given by,

$$\Delta\mathbf{k} = \mathbf{G} + \mathbf{s}. \tag{2.32}$$

One can see that for $\mathbf{s} = 0$, the Ewald sphere cuts through the center of a relrod and the Bragg condition is fulfilled.
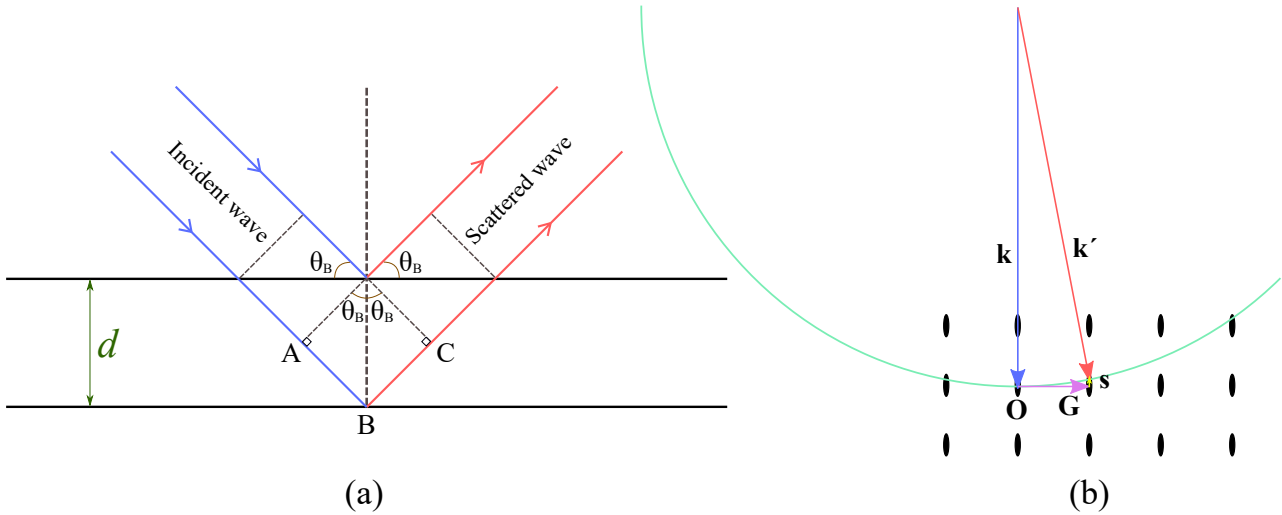
Figure 2.9: (a) Simplified illustration of the Bragg law where an incident wave is reflected by parallel planes with distance d between them, emitting a scattered wave. The path difference between the waves is AB + BC. (b) Illustration of a segment of the Ewald sphere in reciprocal space. The reciprocal lattice points are stretched out into relrods due to the size of the crystal. Both figures adapted from [12].

In a crystal, many reciprocal lattice vectors $\mathbf{G}$ of all possible values can result in a DP. Each point in the DP would correspond to a lattice plane. However, one has to take into consideration the

difference in phase between the waves diffracted from adjacent parallel atomic planes with the same Miller indices. The structure factor for a crystal lattice is a mathematical way to describe this and is given by,

$$F(\theta) = \sum_{i}^{\infty} f_i(\theta) e^{2\pi j(hx_i + ky_i + lz_i)}, \tag{2.33}$$

where hkl are the Miller indices, $f_i(\theta)$ is the atomic-scattering amplitude of atom i, θ is the angle between the incident and outgoing beam, and x_i, y_i, z_i are defined in equation (2.2). $f(\theta)$ is related to the differential scattering cross-section from equation (2.24) by,

$$|f(\theta)|^2 = \frac{d\sigma(\theta)}{d\Omega}, \tag{2.34}$$

so $f(\theta)$ is the scattering amplitude from an isolated atom and $|f(\theta)|^2 \propto$ to the scattered intensity. From equation (2.33) one can see that the structure factor $F(\theta)$ is the unit-cell equivalent of $f(\theta)$, as it gives the scattering amplitude of the unit cell. It shows the link between the type of atom, its position, the atomic planes (hkl), and the *selection rules* of which beams are allowed to be diffracted. Since the intensity of the DP spots is proportional to the amplitude squared,

$$I \propto |F(\theta)|^2, \tag{2.35}$$

the crystal structure influences the intensity as well. For aluminium, which has an FCC crystal structure, it is known that the coordinates for the atoms are:

$$(x_i, y_i, z_i) = (0, 0, 0), \left(\frac{1}{2}, \frac{1}{2}, 0\right), \left(\frac{1}{2}, 0, \frac{1}{2}\right), \left(0, \frac{1}{2}, \frac{1}{2}\right). \tag{2.36}$$

Putting these values into equation (2.33) gives

$$F_{\text{Al}} = f_{\text{Al}} \left[1 + e^{\pi i(h+k)} + e^{\pi i(h+l)} + e^{\pi i(l+k)} \right]. \tag{2.37}$$

When F_{Al} is equal to zero for a selected combination of hkl, it means that diffraction spots that would have been present for a simple cubic lattice are absent for an FFC lattice. Trying different combinations of hkl to see what equals zero, eventually gives these selection rules for aluminium:

$$F_{\text{Al}} = \begin{cases} 4f_{\text{Al}} & \text{if} \quad h, k, l \text{ all even or all odd} \\ 0 & \text{if} \quad \text{mixed parity} \end{cases} \tag{2.38}$$

2.3.3 Anatomy of a TEM

To be able to interpret TEM results, one must understand how the instrument operates. A typical TEM design is shown in Figure 2.10. A TEM is comparable to a VLM in the sense that instead of using glass lenses, electromagnetic fields are used as lenses. In a VLM, the lenses have a fixed strength and their placements change. In a TEM, the lenses have a fixed placement and their strength is controlled by variable currents through magnetic coils. In addition, instead of a light source, an electron source or "gun" is used to emit a beam of electrons. The two types of guns are *thermionic* and *field-emission* guns. Thermionic sources are commonly LaB_6 crystals that are heated to produce electrons. The heat gives the electrons enough energy to overcome the work function of LaB_6 so that

they can escape the source. A field-emission source consists of a fine tungsten needle, and a large electric potential between it and an anode is used to produce electrons. The extracted electrons are accelerated utilizing an electric field. Similarly for the VLM, it is convenient to split the TEM into the illumination system, the objective lens (OL) system, and the imaging system. These three systems are built on top of each other to form a column, and this column environment needs to be in a vacuum since electrons scatter off of gases. The vacuum pressure inside the column of a standard TEM is $\sim$ 10^{-5} Pa.

The three systems in a TEM are indicated in Figure 2.10. The *illumination system* consists of the gun and the condenser lenses (CL), and its role is to transport the electrons from the source to the specimen. Together with a condenser aperture (CA), they control whether the beam is broad or focused (i.e. the width) and with which angle the beam enters the specimen (convergence angle). The *objective lens system* consists of the objective lens, the objective aperture (OA), and the specimen holder. The objective aperture is located in the back focal plane (BFP) of the objective lens and manipulates which electrons make up the final image. This system has the most important role in the TEM because the electron beam and specimen interactions occur here, and it is where the images and diffraction patterns are formed. The quality of the objective lens system affects the quality of the data collected about the specimen. A selected area aperture (SA) lies in the image plane of the objective lens and above the imaging system. Its role is to select an area of the specimen and only allow electrons from that area to pass through. The *imaging system* consists of a diffraction lens (DL), an intermediate lens (IL), a projector lens (PL), a viewing screen and an image recording system. The diffraction lens and the intermediate lens are used to magnify and focus the image or diffraction pattern created by the objective lens in the BFP. The projector lens projects the image or diffraction pattern onto the viewing screen or the image recording system.

The specimen is inserted into the objective lens in the specimen holder. This makes it easier to correct varying defects like aberrations and astigmatism from the magnetic lenses. Since the pole pieces (structures that direct the magnetic field) are so close to the specimen, it can restrict the capacity to tilt the specimen in the z-direction and, therefore, the signals generated from it. TEMs have astigmatism- and aberration-correction systems for several lenses to overcome these defects, but one can also use small apertures to restrain aberrations. The specimen holder controls the orientation of the specimen by tilting in the x- and/or y-direction. The specimen usually has to be a 3 mm in diameter disc, since specimen holders require this.
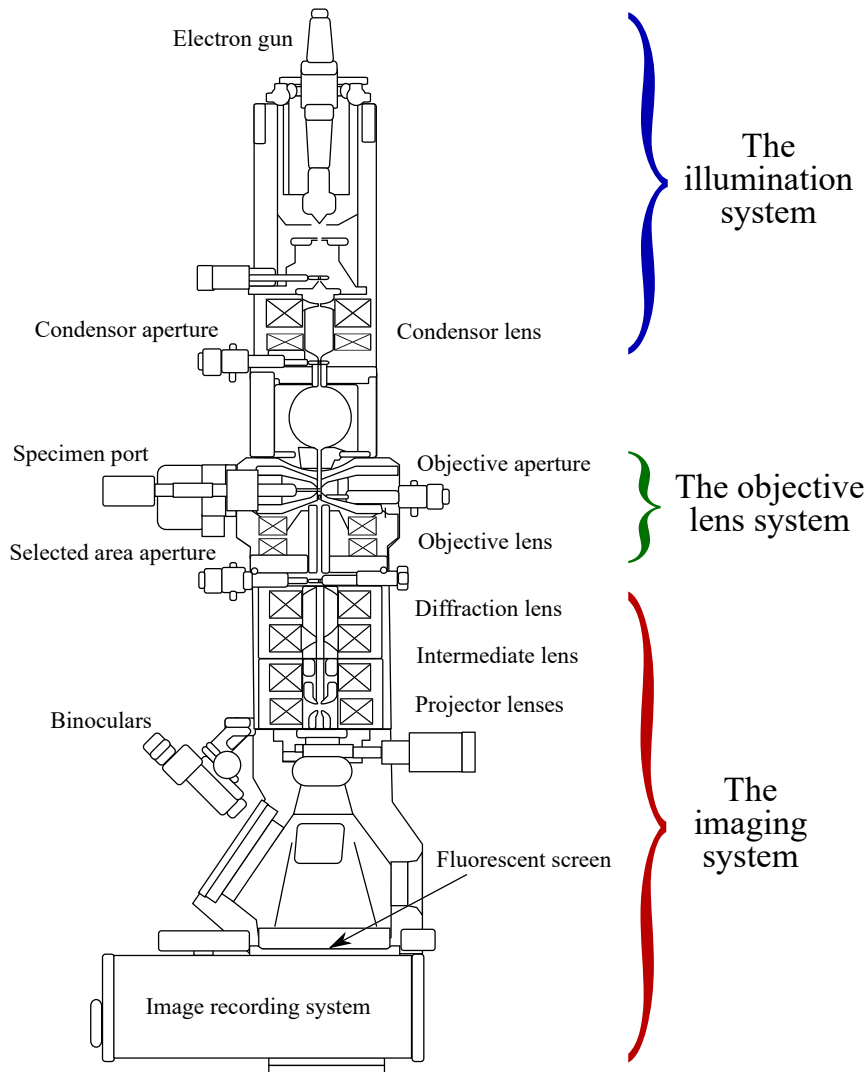
Figure 2.10: Schematic of a standard TEM showing the conventional apertures and lenses. The illumination system, the objective lens system and the imaging system are highlighted. Adapted from [35].

2.3.4 Operation Modes in TEM

As one might remember from Figure 2.8(a), the electron specimen interaction generates various signals. These signals can be utilized in several ways, meaning that a TEM needs different operational modes specialized to a particular signal and analyze different aspects of the sample microstructure. Different techniques were implemented throughout the thesis, and this section will give a brief explanation of the most important techniques. For a more detailed explanation of the modes, other literature (e.g. [6]) is recommended.

Obtaining Contrast

There are two main causes for contrast in TEM images: *amplitude contrast* and *phase contrast*. This is because when an incident electron beam scatters onto a specimen, it can change the amplitude and phase of the electrons in the beam. The electrons scattered at different angles have different phases,

which leads to interference. Phase contrasts are variations in detected intensity generated by interference between coherently scattered beams. There must therefore be more than one beam contributing to the image. Amplitude contrast is a combination of *mass-thickness contrast* and *diffraction contrast*, since it comes about during diffraction or when electrons are deflected by the nucleus. The contrast in DF-TEM images is normally dominated by amplitude contrast, while for HAADF-STEM it is mass-thickness contrast. BF-TEM images have both mass-thickness contrast and diffraction contrast. Areas with high atomic number Z will appear darker in BF images since the scattering probability is proportional to Z. In addition, the thicker or denser areas of the specimen will also look darker since there are more atoms to scatter off of. Mass-thickness contrast is always present in TEM [36]. Diffraction contrast occurs because of local variations in diffraction conditions in the specimen. For example, if a specimen has crystals of varying orientations or structures, it would show up as different intensities where areas that have diffracted more strongly are darker.

High Resolution TEM

High resolution TEM (HRTEM) is a technique that uses phase contrast. The procedure to acquire HRTEM images is to insert a large OA (or no OA) to allow the direct beam and diffracted beams to pass, and then go to high magnification (>x500k). One can achieve atomic resolution using this technique, but spherical aberrations can affect the final image, making image interpretation difficult. It is also important to regulate the astigmatism in the system, and to adjust to the correct height and focus. Interpretation of HRTEM images is not straightforward because the *contrast transfer function* (CTF) is not linear with spatial frequency, which makes it difficult to determine which atomic columns light up in the image. Therefore simulations are needed to provide information about the atomic structure of the material. The FFT of HRTEM images can also show the spatial frequencies of the sample.

Selected Area Electron Diffraction

An advantage of TEM is the ability to switch between *image mode* and *diffraction mode* with the push of a button. Image mode takes place when the object plane of the IL is the image plane of the OL, and the image is projected onto the viewing screen or camera. Diffraction mode takes place when the object plane of the IL is the BFP plane of the OL, and the diffraction pattern is shown on the screen or camera. For *selected area electron diffraction* (SAED) mode, parallel beams are required. The procedure starts with inserting an SA and centering it on the optic axis. One should spread the electron beam to max so as not to damage the detector, and then go to selected area diffraction (SAD) mode. It is possible to adjust the focus of the DP using diffraction-focus controls. Figure 2.11(a) illustrates an example of the beam path so one can see how a DP appears on a fluorescent screen.

Studying a crystalline specimen in SAED mode gives a DP with areas of maximum intensity, referred to as spots or reflections. See Figure 2.11(b) for an example of this. Each spot in the DP corresponds to a reciprocal lattice point characterized by the Miller indices *hkl*. Therefore, each spot in the DP is related to an array of crystal lattice planes in real space characterized by the same Miller indices *hkl* from Section 2.1.2. As mentioned previously, the factor that determines which spots are visible is where the edge of the Ewald sphere intersects the relrods. Selected area diffraction patterns (SADP) are useful for selecting the spots used for BF or DF imaging.
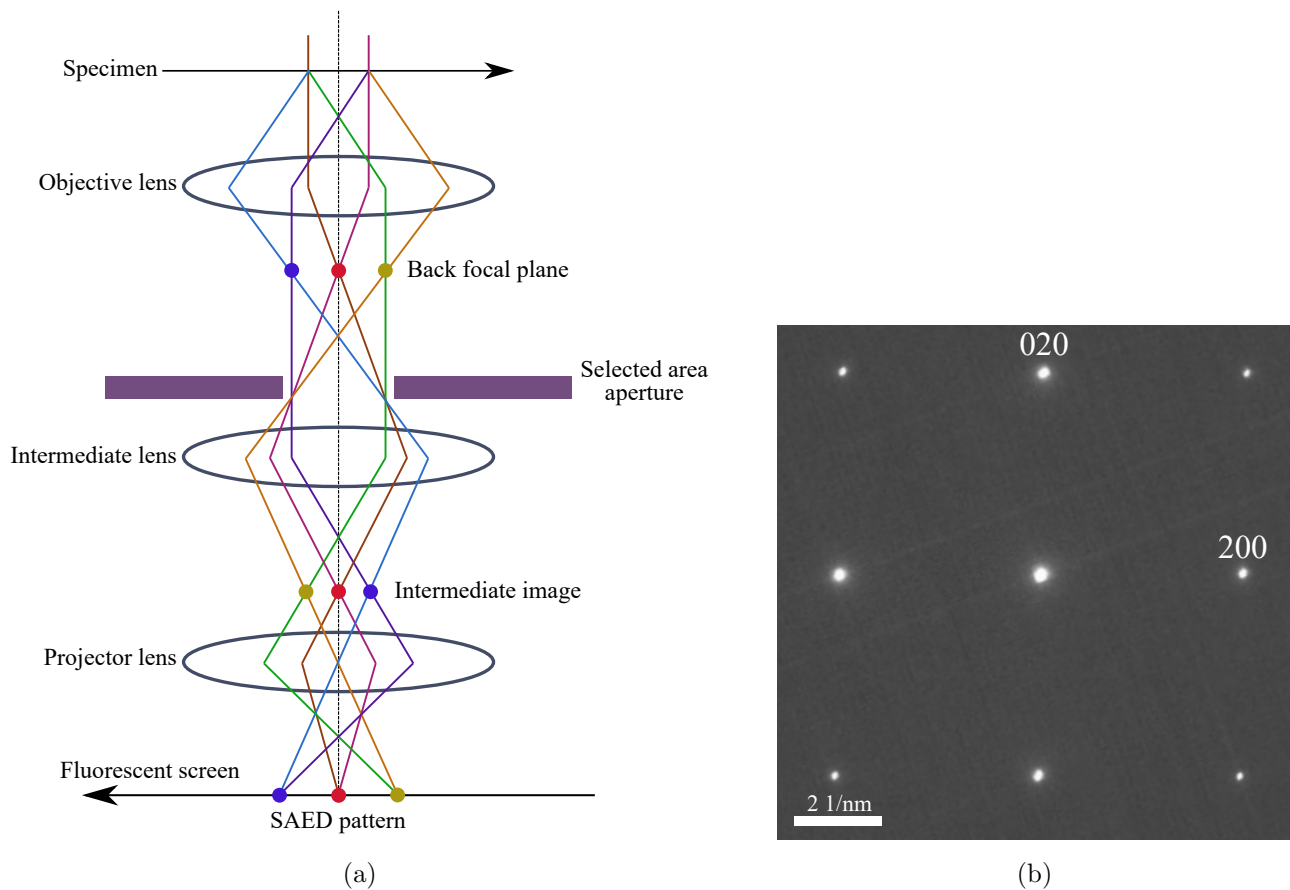
Figure 2.11: (a)Simplified schematic of the beam path in SAED mode. Adapted from [6]. (b) Example of a SAED pattern from a 6xxx Al alloy at the [100] zone axis. Taken directly from [37].

Bright Field

Bright field (BF) TEM images are created using the direct electron beam, and this mode is quite common. The procedure to obtain BF images starts with using a selected area aperture (SA), going to selected area diffraction mode, and viewing the selected area diffraction pattern. The DP will have a central spot consisting of electrons from the direct beam. An OA is inserted into the BFP of the OL, which will block out most of the DP. Centering the OA around the bright central spot, removing the SA, and returning to image mode will result in bright field mode. Figure 2.12(a) illustrates an example of the beam path and see Figure 2.12(b) for an example of a BF image.

As mentioned earlier, amplitude contrast dominates in a BF-TEM image. This implies that BF-TEM images give information about the different phases of the same material, but also if there are variations in the type of material. BF-TEM also shows strain contrast in the imaged region. For Al, strain from precipitates and dislocations appear darker in BF images since strain increases scattering and therefore the diffraction intensity [30]. This technique does not have as great resolving power as HRTEM mode because the OA blocks the diffracted beams, but it makes up for it with good contrast at medium magnifications.
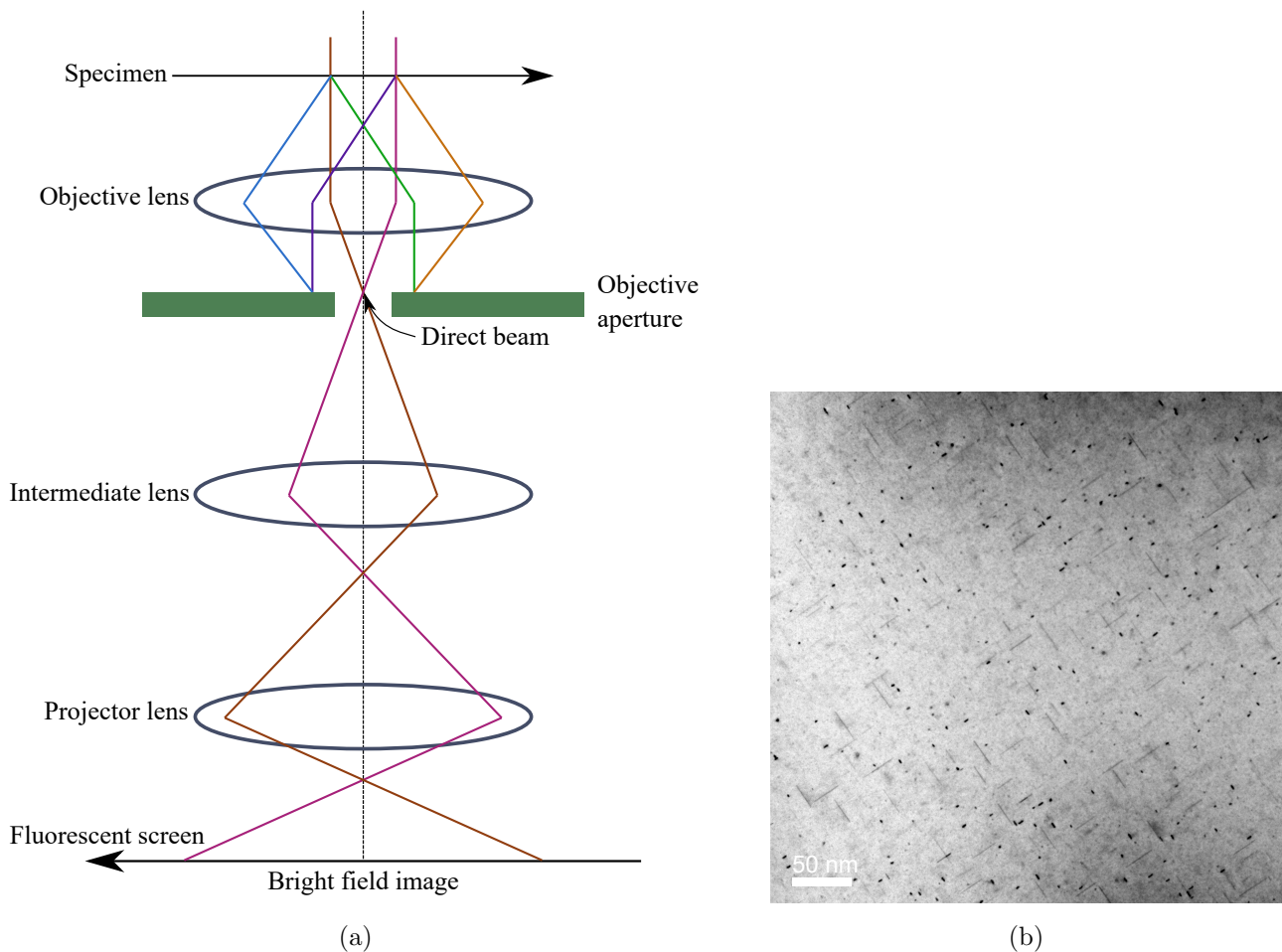
Figure 2.12: (a) Simplified schematic of the beam path when generating a BF image. Adapted from [6]. (b) Example of a BF-TEM image of a 6xxx alloy showing the contrast between the precipitates and the matrix.

Dark Field

Dark field (DF) TEM images are created in a similar way to BF-TEM images, but instead of using the direct beam, one uses one (or a few) diffracted beams. This is done in one of two ways. The first way is to start in SAD mode by moving the OA from the central spot to a dark area between the bright spots to block the direct beam and let the diffracted beams through. Returning to image mode will result in a DF image. The second way is to keep the OA in place and tilt the incoming electron beam by an angle of 2θ, which is equal and opposite to the scattering angle. This will allow the diffracted electrons to travel along the optic axis. In SAD mode, it will look like the diffraction pattern has shifted so that the OA encloses an area containing diffracted spots from precipitates, since the phases have larger unit cells and reciprocal space is denser. Tilting the incoming electron beam is the recommended procedure since off-axis electrons are affected by aberrations and astigmatism more than on-axis electrons. Figure 2.13(a) illustrates an example of the beam path when applying the tilting method.

Similar to BF-TEM images, amplitude contrast is the main source of contrast, however, the contrasts are reversed in DF mode. This is easier to understand if one compares the BF image in Figure 2.12(b)

and the DF image in Figure 2.13(b). One sees that the Al matrix background is bright in BF mode while almost black in DF mode. The precipitates look dark in BF mode, while they are bright white in DF mode. An advantage of DF-TEM is that one can select electrons from a specific area of interest, which results in images with greater binary contrast. This makes it easier to see what one is interested in, such as precipitates and dislocations.

(a)   (b)
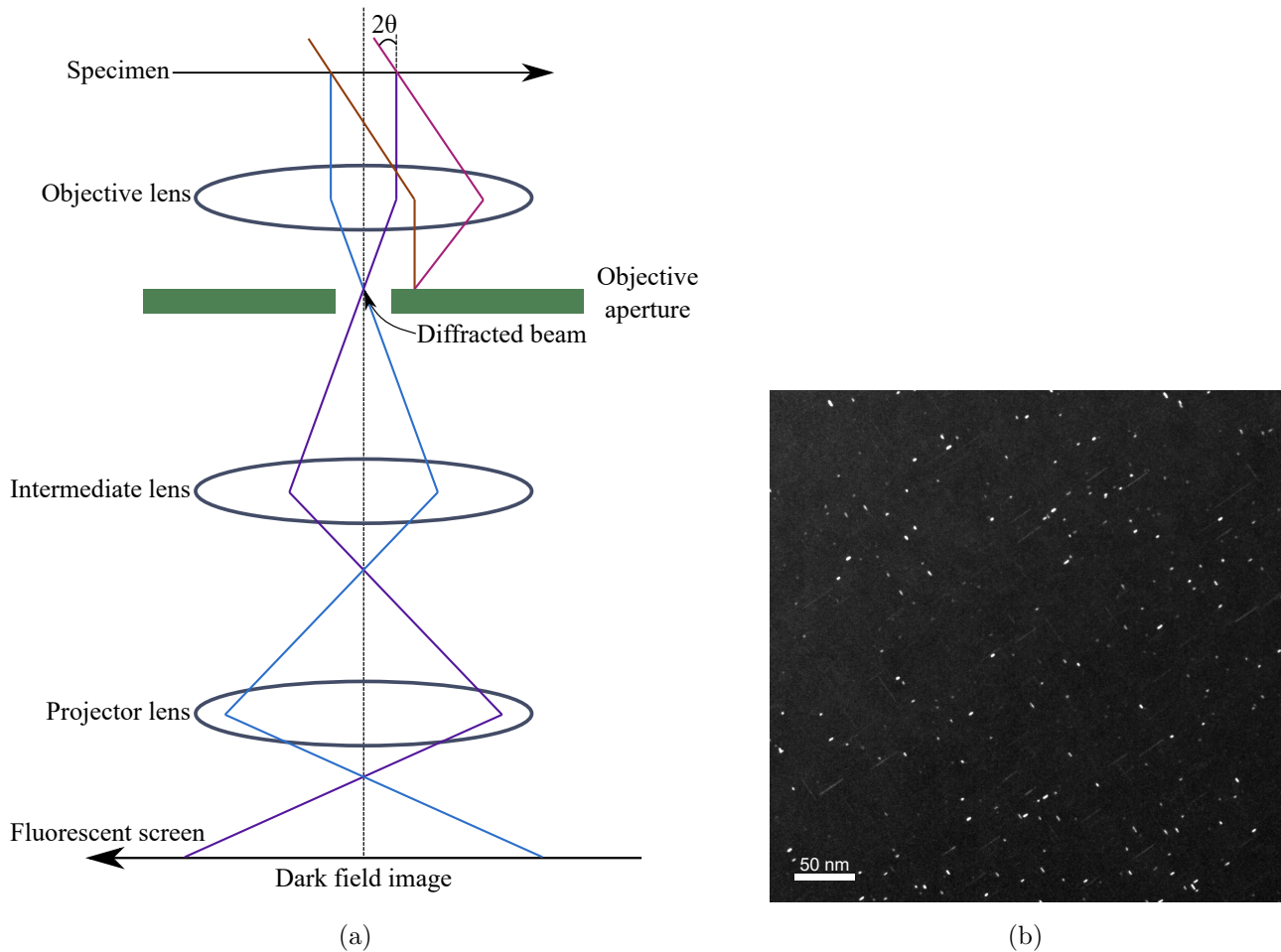
Figure 2.13: (a) Simplified schematic of the beam path when applying the tilting method to generate a DF image. Adapted from [6]. (b) Example of a DF-TEM image taken from the same sample and area as Figure 2.12(b). The objective aperture was centered outside the Al reflections in a quadrant between the (000) and the (020)/(200) reflections.

Convergent Beam Electron Diffraction

In *convergent beam electron diffraction* (CBED) mode, the beam is focused on the sample, and will therefore probe a small area with a convergent beam giving a range of $\mathbf{k}$ vectors. This produces a range of Ewald spheres, which means the total Ewald sphere becomes a shell with a thickness. Several cones of electron beams then exit the specimen resulting in Bragg discs instead of spots giving a CBED pattern. The procedure to obtain CBED images starts in image mode with inserting and centering a CA, usually the second largest one. Change the brightness so the beam converges to a spot on the region of interest, then switch to SAD mode. Adjust the camera length until the preferred CBED pattern is displayed. CBED patterns are dependent on the convergence semi-angle, the camera length,

the probe diameter, the focus and the thickness of the region of interest. See Figure 2.14(b) for an example of a CBED pattern.

An example of the beam path that forms CBED discs is shown in Figure 2.14(a). One can see from the figure that similar to SAED where DP spots are formed in the BFP of the OL, CBED discs are formed in the OL's BFP. CBED images are useful when taken from thicker specimens where dynamical scattering takes place. In addition, CBED can give information about the specimen thickness, the symmetries of a crystal (point group and space group), the lattice parameters and so much more. By tilting the sample off zone to reach the two-beam condition with one excited hkl reflection and the direct beam, one can determine the thickness from the fringe pattern that arises. For an example of a two-beam condition, see Figure 3.3(a) in Section 3.6.1. The central direct beam corresponds to the exact Bragg condition where the deviation vector $\mathbf{s} = 0$. The distance between the minima in the diffracted beam, also known as the fringe spacings, corresponds to the angles $\Delta\theta_i$. The magnitude of the deviation vector $\mathbf{s}_i$ for the ith fringe is given by,

$$|\mathbf{s}_i| = s_i = \lambda \frac{\Delta\theta_i}{2\theta_{\text{B}} d^2}, \tag{2.39}$$

where i is an integer, λ is the electron wavelength, θ_{B} is the Bragg angle for the diffracted hkl plane, and d is the interplanar spacing between the hkl planes. The distance between the center of the direct beam disc and the hkl disc is $2\theta_{\text{B}}$. The fringes are analogous to the real space rocking-curve intensity oscillations. The intensity of the fringes I_g in the diffracted beam varies as a function of the effective deviation vector s_{eff}, the thickness t and the extinction length ξ_g for the diffraction g [38]:

$$I_g(s_{\text{eff}}) = \left(\frac{\pi}{\xi_g}\right)^2 \frac{\sin^2(\pi s_{\text{eff}} t)}{(\pi s_{\text{eff}})^2}, \tag{2.40}$$

where

$$s_{\text{eff}} = \sqrt{s^2 + \frac{1}{\xi_g^2}}. \tag{2.41}$$

The fringes have minimum intensity in equation (2.40) when $s_{\text{eff}} t = $ an integer giving,

$$t^2 \left(s_i^2 + \frac{1}{\xi_g^2}\right) = n_k^2, \tag{2.42}$$

where n_k is an integer [38]. Here k is an integer equal to i, or differs from i but with a constant integer. Knowing the extinction distance ξ_g, one can determine the thickness t of the specimen by rearranging equation (2.42):

$$\frac{s_i^2}{n_k^2} + \frac{1}{\xi_g^2 n_k^2} = \frac{1}{t^2}. \tag{2.43}$$

If ξ_g is unknown, a graphical method must be used. This method is used in this thesis to determine the thickness of the Al foils, which is needed to determine the density of precipitates.
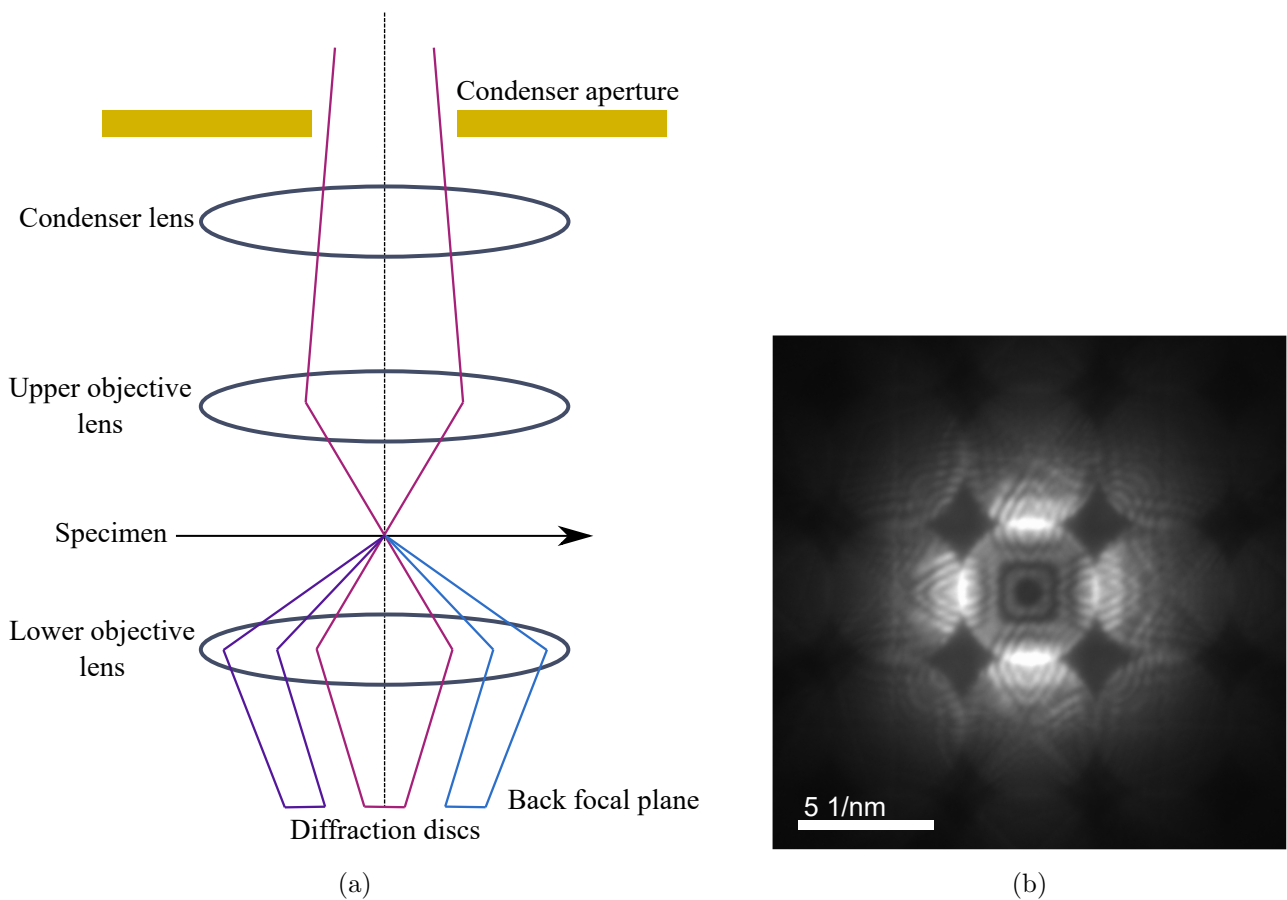
Figure 2.14: (a) Simplified schematic of part of the beam path when generating a CBED pattern. The diffraction discs appear in the BFP of the objective lens. Adapted from [6]. (b) Example of CBED pattern from a 6xxx Al alloy at the [001] zone axis.

Nanobeam Electron Diffraction

Compared to SAD mode where the electron beam travels through a large region of the specimen, *nanobeam electron diffraction* (NBD) mode illuminates a small area, typically $\sim 1\,\text{nm}$. This is similar to CBED, but NBD uses a smaller aperture. The nanometre-sized probe is mainly parallel due to a small circular CA giving a small convergence angle of $\sim 1\,\text{mrad}$. The convergence angle is larger than for SAED and smaller than for CBED, resulting in small non-overlapping discs in the NBD pattern [39]. NBD mode is useful for recording DPs from, e.g., precipitate cross-section, whose area typically are in the nanoscale region, to determine their crystal structure.

Scanning Precession Electron Diffraction

Precession electron diffraction (PED) patterns are made when the incoming beam is rocked at a constant precession angle ϕ around the optical axis. The rocking is done by the upper deflection coils and the beam shapes into a hollow cone. The beam then travels through the sample at an angle instead of on-axis. Under the sample, the beam is de-rocked by lower deflection coils forming another hollow cone. This is why PED is sometimes called double-conical beam rocking. This process is equivalent to having a fixed, on-axis incoming beam and instead precessing the specimen [40]. An example of a PED setup is illustrated in Figure 2.15.
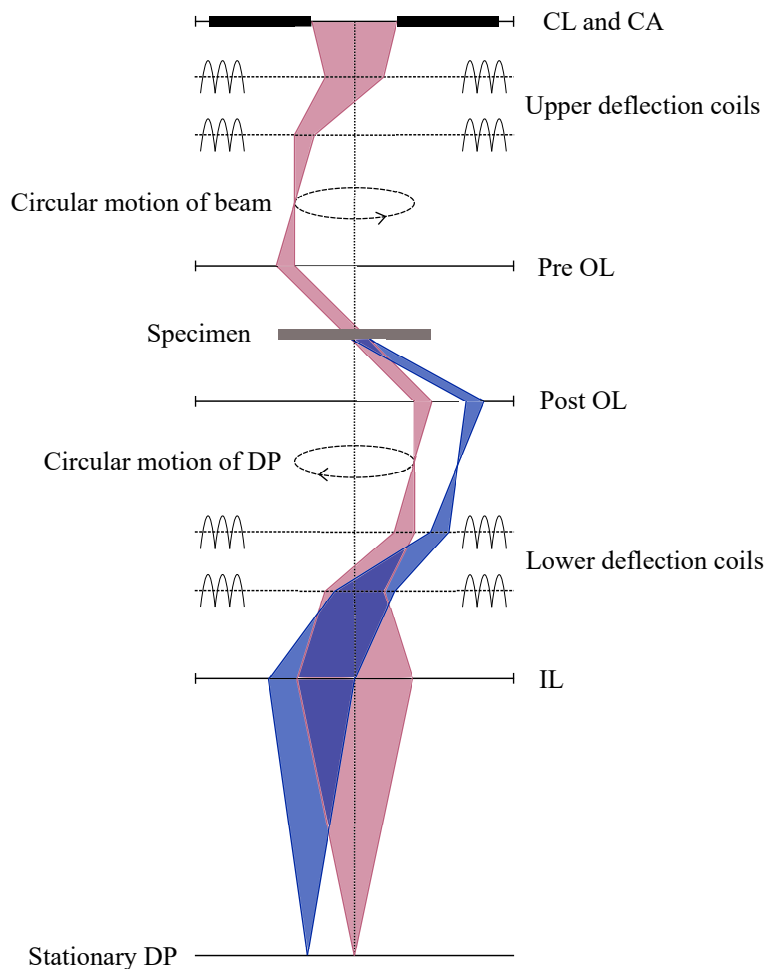
Figure 2.15: Schematic of a setup in PED mode. Adapted from [41].

Since the precession of the electron beam creates a range of wavevectors, it leads to a precession of the Ewald sphere around the optical axis. As the Ewald sphere rotates, it intercepts more relrods than a stationary Ewald sphere, resulting in more spots in a PED pattern compared to an SADP. The intensity of a spot in a PED pattern is an integration of the diffracted intensities over the precession angle under the Bragg condition [40]. PED is useful for phase identification because the reflections in the pattern have reduced dynamical effects and appear kinematic [41].

If one scans the beam across an area while precessing it, one gets *scanning precession electron diffraction* (SPED) [41]. One usually conducts SPED in NBD mode [39]. This means that for each scan

position or pixel, a diffraction pattern is recorded. A SPED dataset has four dimensions (4D) comprising of two dimensions in real space (x and y) and two dimensions in reciprocal space (k_x and k_y). An important thing in SPED is that the scanning speed must be synchronized with the precession frequency, such that each pixel in the dataset is recorded during an integer number of precession cycles. SPED can be used for strain mapping, phase mapping, orientation mapping and structure determination [41].

HAADF-STEM

Scanning transmission electron microscopy (STEM) images are created pixel by pixel using a sub-nanometer-sized electron probe with a beam convergence of a few tens milliradians. When the converging incident beam illuminates the specimen, a CBED pattern appears far below the specimen. This pattern has a lot of overlap between the discs (otherwise the probe size would be too large and one would not obtain lattice resolution). The intensity in chosen areas of the CBED pattern is detected by STEM detectors. The signals from this are converted into an image where the intensity of a pixel corresponds to the probe location of the specimen. The STEM detectors are categorized according to the range of scattering angles of transmitted electrons that they detect [42]. See Figure 2.16 for a simplified schematic of this. A *high angle annular dark field* (HAADF) detector picks up incoherently elastically scattered electrons at high angles. Rutherford scattering is useful for understanding electron scattering at high angles and is given by,

$$\frac{d\sigma}{d\Omega} = \frac{Z^2 e^4}{16 E_0^2 \sin^4(\theta/2)}, \tag{2.44}$$

where $d\theta/d\Omega$ is the differential scattering cross-section, e is the electron charge, E_0 is the kinetic energy of the incident electron, Z is the atomic number, and θ is the total scattering angle [38]. The probability that an incident electron scatters at a higher angle is proportional to Z^2, so heavier elements scatter more. This dependence on Z explains why HAADF-STEM is also known as *Z-contrast imaging*. HAADF-STEM images are formed by summing the intensities of electrons scattered by individual atoms, also including thermal diffuse scattering. When the probe size is smaller than the atomic column spacing in a crystal, each atomic column is illuminated consecutively as the probe scans over the specimen. The intensity of each column in the map depends on the average atomic number Z of the atoms in the column. Consequently, HAADF-STEM is less sensitive for materials with low Z. Due to the high intensity of the electron probe scanning an area over a time period, a drawback to HAADF-STEM is the possibility of contamination and beam damage [38].
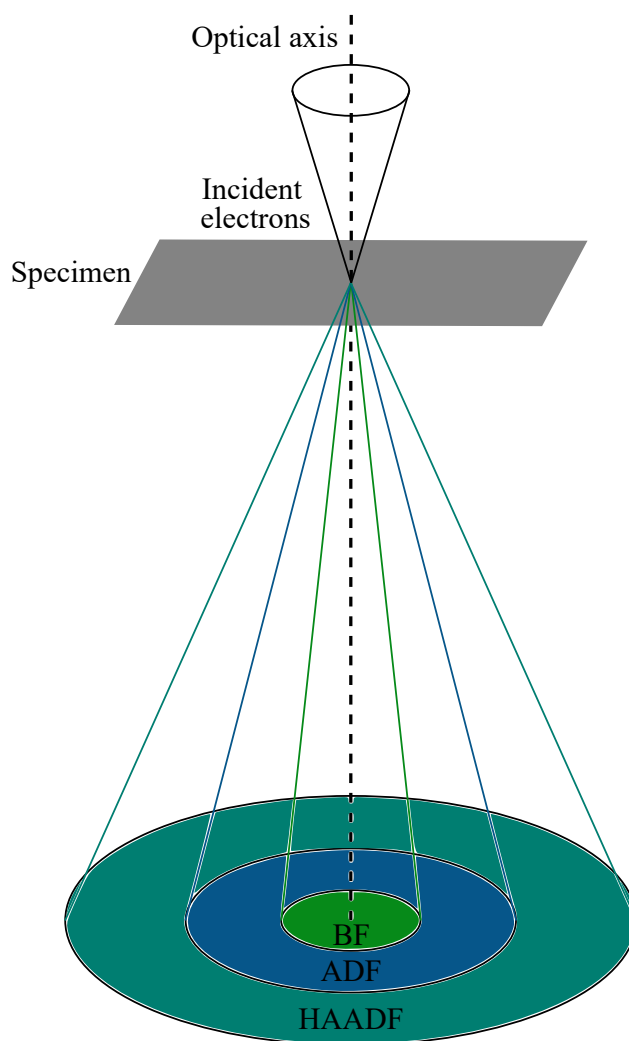
Figure 2.16: Simplified schematic of a STEM setup including a bright field (BF), annular dark field (ADF) and high angle annular dark field (HAADF) detector. Adapted from [43].

2.3.5 TEM Based Strain Measurements

There are several ways to measure the displacement of atoms in a crystal lattice, and therefore strain, with a TEM. This can be done in either diffraction mode or image mode. High resolution electron microscopy (HREM) can be implemented to measure individual atomic positions and their local lattice displacements directly, and hence calculate the strain [44]. It is also possible to place an aperture on a reflection in the Fourier transform of a HREM image, and take the inverse Fourier transform. Information about the local lattice displacements and the displacement field can be extracted from the phase components in the image. From this, the local strain components can be calculated [45]. Annular dark-field STEM (ADF-STEM) is a technique with atomic resolution and can be used to accurately determine where an atomic column is to get high resolution strain measurements [32]. The high resolution methods can be difficult to execute and only covers a small region of the specimen, while diffraction-based techniques measure the atomic plane spacings in reciprocal space and can cover a larger area [46].

A method based on NBD is utilized in this thesis to acquire strain maps, where a series of DP from a strained and unstrained region are acquired and compared. By computing the drift of the DP spots due to the relative lattice mismatch, one can determine the strain. If the specimen is a 3D real space crystal, the DP obtained from it is a 2D projection of its 3D reciprocal lattice. Consequently, the strain measured with this DP method is a 2D projection of a 3D strain field. The strain is computed by utilizing two reciprocal lattice point vectors g_1 and g_2 that are related to the lattice spacing of the crystal planes by equation (2.7). These vectors are recorded from the DP and must be non-parallel. The vectors g_1 and g_2 are defined by their x- and y-components perpendicular to the zone axis. They give the following reciprocal lattice point matrix G [30]:

$$G = \begin{bmatrix} g_{1x} & g_{2x} \\ g_{1y} & g_{2y} \end{bmatrix} \tag{2.45}$$

The 2D deformation matrix D of the area where the DP was acquired is given by,

$$D = (G^{\mathrm{T}})^{-1} G_0^{\mathrm{T}} - I, \tag{2.46}$$

where G is the reciprocal point matrix from a strained region, and similarly G_0 is from an unstrained reference region. Here, I is the identity matrix and T represents the matrix transpose operation. In cases with less than $10°$ rotation and 4% strain, which is relatively small, the 2D strain tensor ε is computed by taking the symmetric part of D [30]:

$$\varepsilon = \frac{1}{2}(D + D^{\mathrm{T}}) = \begin{bmatrix} \varepsilon_{xx} & \varepsilon_{xy} \\ \varepsilon_{yx} & \varepsilon_{yy} \end{bmatrix}. \tag{2.47}$$

The 2D rotation tensor ω is computed by taking the asymmetric part of D:

$$\omega = \frac{1}{2}(D - D^{\mathrm{T}}) = \begin{bmatrix} \cos\theta & -\sin\theta \\ \sin\theta & \cos\theta \end{bmatrix}, \tag{2.48}$$

where θ is the rotation angle between the strained lattice and the unstrained lattice. By conducting SPED in NBD mode, one can scan a larger area and calculate the strain for each pixel by applying this method to its DP. This generates a local strain map in real space. As mentioned earlier, precession reduces dynamical effects and studies have shown that it improves the quality and robustness of strain analysis [47]. The same study also found that precession yields more flexible experimental conditions, in particular by allowing larger convergence angles than NBD mode and consequently a smaller probe size.

3 Material and Experimental Methods

3.1 Material

The material from YKK was provided as cylindrical rods with a diameter of $\Phi = 3.8\,\text{mm}$. The composition of the Al alloy was measured by YKK in Japan using inductively coupled plasma - optical emission spectrometry (ICP-OES). Measurements of the composition were also taken in Trondheim on a non-heat treated alloy using electron probe microanalysis (EPMA) by Morten Peder Raanes. This was done in homogenous areas of $1\,\text{µm}$, not taking into account Al-Si-Fe particles which are expected to be present in the alloy [48]. The values from both methods are presented in Table 3.1. The production process by YKK before delivery is shown in Figure 3.1. The process consists of casting and homogenisation, extrusion to $8\,\text{mm}$, SHT, and lastly drawing to $3.8\,\text{mm}$. The material was given as drawn.

Table 3.1: The measured composition of the alloy. All values are in wt.%.

Method	Cu	Mg	Si	Fe	Ti	B	Zn	Mn	Cr	Zr
ICP-OES	1.27	1.01	0.38	0.069	0.019	0.004	0.003	0.001	< 0.001	< 0.001
EPMA	1.17	1.30	0.32	-	-	-	-	-	-	-

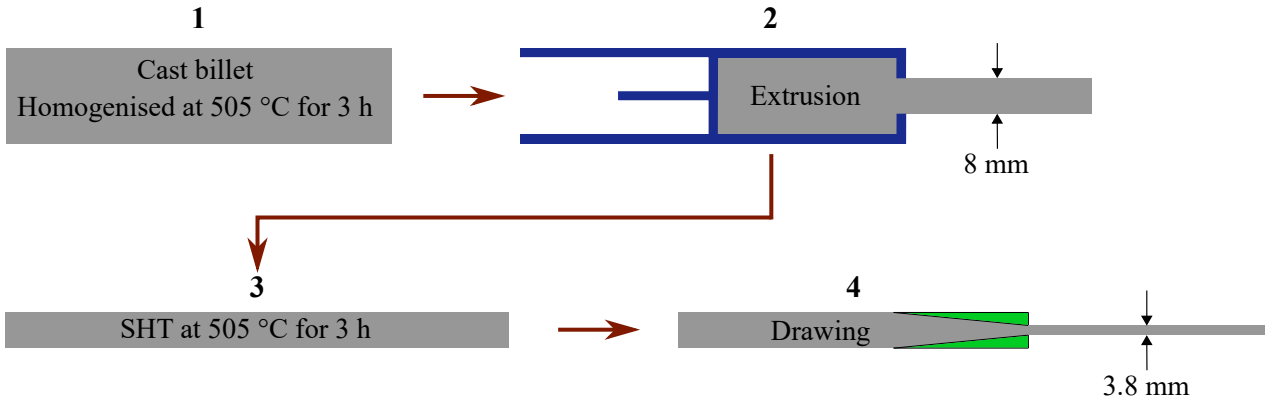Figure 3.1: Processing of the material before it was received from YKK. Figure adapted from [9].

3.2 Heat Treatment

After receiving the cylindrical bars from YKK, they were first cut into $20\,\text{mm}$ long pieces using a Struers Labotom-5 cutting machine. Ten pieces of the alloy underwent ten different precipication hardening sequences without NA. SHT in a Nabertherm N17/HR Chamber Muffle Furnace was done at $505\,°\text{C}$ for $3\,\text{h}$ and quenched in room temperature (RT) water for $5\,\text{s}$. The ten samples were placed into a Nabertherm Forced Convection Chamber Furnace N15/65HA at $160\,°\text{C}$ for AA (directly aged). The samples were exposed to $<2\,\text{min}$ NA during transferral. They were then taken out of the air oven one by one at these times respectively: $10\,\text{min}$, $30\,\text{min}$, $1\,\text{h}$, $3\,\text{h}$, $6\,\text{h}$, $12\,\text{h}$, $24\,\text{h}$, $48\,\text{h}$, $96\,\text{h}$ and $168\,\text{h}$, a total of one week. Each sample was water quenched (WQ), rinsed with ethanol and hardness measurements were taken (more detail on this in Section 3.3).

Based on the results of the hardness measurements from heat treatment without NA, four AA times were chosen to proceed with: 10 min, 1 h, 6 h and 48 h. These were combined with four NA times: 30 min, 20 h, 120 h and 744 h, a total of one month. This gives a total of 16 different conditions with prolonged (non-zero) NA time. SHT and WQ were done similarly to the heat treatment procedure without NA, but were not placed into an oven immediately for AA. Instead, the samples were divided into four groups and were set to rest at RT for their respective NA times. Following this, the samples were placed into the oven and taken out one by one at their chosen AA times, similar to before. The samples were also WQ, rinsed with ethanol and their hardness was measured. Figure 3.2 shows the temperature-time curve for the total heat treatment process.
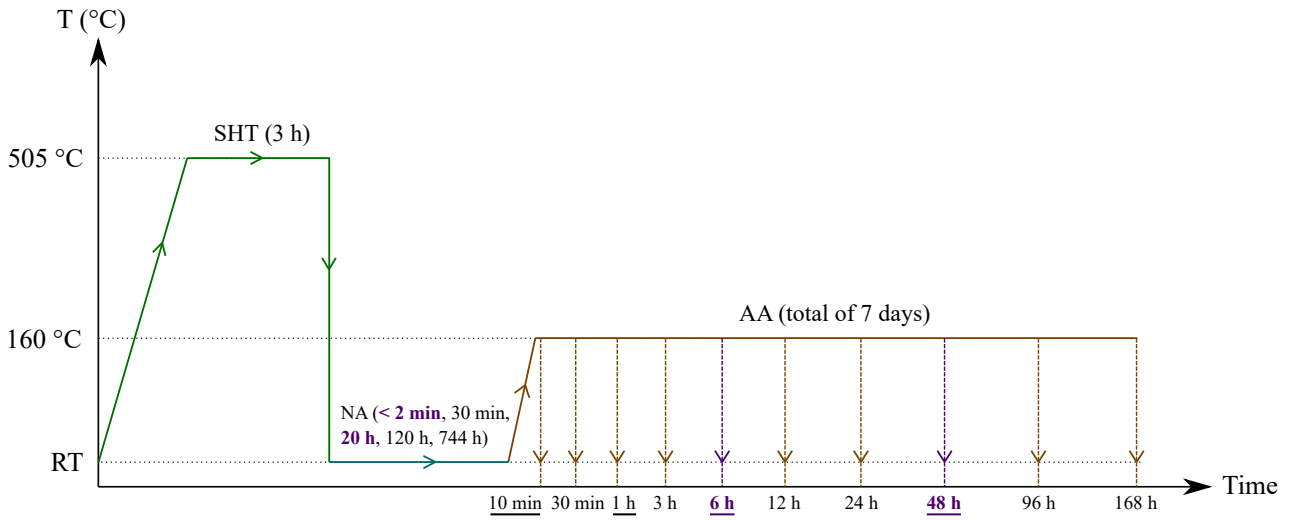

Figure 3.2: Schematic of the heat treatments performed on the alloy. After SHT, the samples were WQ and stored at RT for NA at different times before placed in an oven for AA. The dashed vertical lines under AA corresponds to WQ followed by hardness measurements. The underlined AA times were used in the heat treatments with NA, while the remaining AA times were only used for direct ageing. The purple times in bold indicate which conditions were studied by TEM.

3.3 Vickers Hardness Tests

After AA, a 1.5 mm piece from each sample was cut using a low-speed saw from South Bay Technology model 650. Since the utilized silicon carbide saw blade has a thickness of 508 µm, each piece became closer to 1.2 mm thick. The samples were glued to a steel polishing stub, and polished using a Struers LaboPol polishing machine starting with P1200 paper and then P2500 paper. Lastly, they were polished with P4000 paper until they obtained a mirror finish. The paper was changed when the polishing stripes pointed normal to the previous stripes. The hardness measurements were done using a calibrated Innovatest Vickers hardness testing machine with a 0.5 kg load and a 10 s load time. An indent from the machine has the shape of a pyramid with a square base, and the square had a diameter of approximately 100 µm. Each indent was at least 300 µm from the edge of the sample and a minimum of 500 µm apart. Eight measurements were taken for each condition. The diameters d_1 and d_2 of each indent were noted down, in addition to their absolute difference Δd. The hardness

measurements were given in units HV by the machine. The formula for HV is given by,

$$\text{HV} = F \cdot \frac{2\sin\left(\frac{136°}{2}\right)}{\langle d \rangle^2},$$ (3.1)

where F is the load applied in kg and $\langle d \rangle = \frac{d_1 d_2}{2}$ is the mean of the two diagonals [49]. The mean, standard deviation and standard error of the measurements were calculated and the data was plotted using Matplotlib in Python [50].

3.4   TEM Sample Preparation

The conditions chosen to be studied with TEM were selected based on the results from the hardness measurements. Their nomenclature is given in Table 3.2. As explained earlier in Section 2.3.1, TEM samples must be electron transparent with a thickness between 10 nm and 200 nm. For Al, the samples should be ∼100 nm thick. The cylindrical samples needed to be shaped into 3 mm in diameter discs, since TEM specimen holders require this. This was accomplished by first cutting 1.5 mm pieces using the same low-speed saw as in Section 3.3. The samples were mechanically polished with Struers LaboPol on both circular sides starting with P1200 paper, then P2500 paper, finishing up with P4000 paper. The result was 3.8 mm discs with a thickness of 100 μm and a mirror finish on both sides. 3 mm discs were then punched out with their plane normal to the drawing direction.

Table 3.2: The nomenclature for the four different conditions investigated in the present study.

Designation	0-48	20-48	0-6	20-6
NA time	0 h	20 h	0 h	20 h
AA time	48 h	48 h	6 h	6 h

Electrolyte polishing, also referred to as electropolishing, is a procedure where an electrolyte solution etches a hole into the sample under a set potential. The 3 mm disc sample is put into a sample holder, and the sample holder is put into the electropolishing machine. The two nozzles in the machine function as the cathode, while the sample in between them functions as the anode. The machine pumps electrolyte through the nozzles to etch the sample from both sides until a hole forms. A light source is positioned on one side of the disc, while a light sensor lies on the other side. When the hole is formed, light is able to travel through to the sensor stopping the machine. The samples were electropolished using Struers TenuPol-5 electropolishing unit with an applied voltage of 20 V, a light stop value of 100, and a pump flow rate of 20. The electrolyte was cooled using liquid nitrogen and held between a temperature of −20 °C and −30 °C. The electrolyte comprised of 1/3 nitric acid and 2/3 methanol. Since ethanol reacts strongly with the electrolyte, the samples were first rinsed in methanol to remove traces before being rinsed in ethanol.

3.5 TEM Studies

To study the four conditions, three different (S)TEMs were used: JEOL JEM-2100, JEOL JEM-2100F and JEOL JEM-ARM200F. All three instruments were operated at 200 kV. The JEOL JEM-2100 TEM is equipped with a LaB_6 thermionic electron source, and a Gatan 2k Orius CCD camera. This TEM was used for acquiring BF, DF and CBED images for precipitate statistics. For each condition ten BF images were taken at x400k magnification, five to seven BF images were taken at x200k magnification, five to seven DF images were taken at x200k magnification, and five to seven CBED images. The JEOL JEM-2100F TEM is equipped with a Schottky ZrO/W field emission gun (FEG) and a bottom-mounted Gatan 2k UltraScan CCD camera. HRTEM images were taken by this camera. For obtaining the SPED datasets of the **0-48** and **20-48** conditions, the JEOL JEM-2100F was operated by Dr. Sigurd Wenner in NBD mode. The alignment of the double-rocking probe was done following the procedure described by Barnard et al. [51] using NanoMEGAS DigiSTAR control software. The NanoMEGAS P100 scan generator controlled the precession and scanning of the electron beam. A Medipix3 MerlinEM camera from Quantum detectors recorded the SPED patterns in 12-bit mode. The parameters used in all the scans are listed in Table 3.3. The SPED calibration procedures can be found in Appendix B.

Table 3.3: Parameters used to obtain the SPED datasets. The nominal values were given by the software and the third column showcases these values after calibration.

Parameter	Nominal value	Value
Precession frequency	100 Hz	-
NBD probe size	0.5 nm	-
Convergence semi-angle	-	1.41 mrad
Precession angle	0.69°	-
Dwell time	40 ms	-
Camera length	12 cm	23.4 cm
Scan area	(400 x 400) pixels	277 nm x 277 nm
Step length	0.926 nm	0.692 nm

The JEOL JEM-ARM200F is equipped with a cold ZrO/W FEG and was operated by Dr. Sigurd Wenner. The utilized convergence angle was 27 mrad and the probe current used was ~30 pA. The HAADF-STEM images were obtained using a Gatan ADF detector with 1.5 mm camera length and collection angles between 67 mrad and 155 mrad, for the inner and outer angles, respectively. The pixel dwell time was 19 µs and each image had (1024 x 1024) pixels. All of the data was obtained under 15° total tilt of the specimen and in the [001] Al zone axis.

3.6 Data Processing and Analysis

During this thesis, a significant amount of data was collected and several processing procedures were used on various data to extract relevant information. This section will introduce and explain the different processing procedures.

3.6.1 Precipitate Quantification

This section on precipitate quantification is based on [52] and is used as reference unless stated otherwise. Taking TEM images along the [001] Al zone axis will show precipitates lying in the three $\langle 100 \rangle$ Al directions. Precipitates lying along the [100] and [010] Al directions are seen from the side, so their length can be measured. Precipitates lying along the [001] Al direction are seen as differently shaped spots, so their cross-section area can be measured. The number of precipitates per area can also be counted. The different quantities that were measured and calculated are described in Table 3.4.

Table 3.4: The quantities used in precipitate statistics and their descriptions.

Quantity	Description
$\langle CS \rangle_j$	Average precipitate cross-section area in image j
$\langle l \rangle_{\mathrm{m}_i}$	Average measured precipitate length in image i
A_i	Area of image i
t_i	Thickness of the specimen in image i
V_i	Volume of the specimen in image i
N_i	Number of counted precipitates in image i
ρ_i	Precipitate number density in image i
$\langle \rho \rangle$	Average precipitate number density across all images
$\langle l \rangle_{\mathrm{m}}$	Average measured precipitate length across all images
$\langle CS \rangle$	Average precipitate cross-section area across all images
VF	Precipitate volume fraction of the specimen

To measure the cross-section area of the precipitates, ten BF-images were taken at x400k magnification for each condition ($j = 1 - 10$). There were between $100 - 200$ precipitates in the [001] Al direction in each image. For each image, the cross-section area was measured using Fiji software [53]. In addition, Fiji has a function called *Fit Ellipse* which fits an ellipse to the precipitate and measures the major and minor axis of the ellipse. It also measures the angle at which the precipitate's major axis lies relative to the x-axis of the image. The threshold was selected manually in Fiji to include precipitates and other features that produce contrast in the images. This process is subjective, and therefore the error was estimated by taking three measurements for an image j: first with the lowest acceptable threshold, then with the highest acceptable threshold, and lastly with the appropriate threshold in between. Doing this gave an approximation of the uncertainty from using Fiji and gave an average value of the cross-section area $\langle CS \rangle_j$. $\langle CS \rangle$ and its relative error $\Delta \langle CS \rangle / \langle CS \rangle$ was then calculated for each condition from the ten images. For each precipitate, the aspect ratio was computed by dividing the major axis length of the fitted ellipse by the minor axis length [54].

The procedure to measure $\langle l \rangle_{\mathrm{m}_i}$, A_i, t_i and N_i was to first take between five to seven BF- and DF-images at x200k magnification and between five to seven CBED images for each condition. These sets of three images were all taken in one spot of the specimen. First, the BF image was taken and the tilt angles ϕ_x and ϕ_y were noted. Then without moving the specimen, the DF image was captured in Dark Tilt mode or by moving the OA. Lastly, the CBED image was acquired by tilting the sample

along either (220) or (200) Kikuchi band until the two-beam condition was fulfilled. The tilting was done in image mode, to make sure the beam was kept in the same region while tilting.

The BF-images were used to measure the length of the precipitates that were seen from the side. Between $300-400$ precipitate lengths were measured for each condition using Fiji. $\langle l \rangle_{m_i}$ was calculated from image i, and from that $\langle l \rangle_m$ and its relative error $\Delta \langle l \rangle_m / \langle l \rangle_m$ were calculated across the five to seven images. The DF-images were used to obtain N_i for image i, where the number of precipitates was measured three times automatically with three different thresholds in Fiji, in the same manner as the cross-section area. Over 400 precipitates were counted per image. The area A_i was already known from the BF- and DF-images since they had the same area. The CBED images were used to obtain the thickness t_i of the specimen, where the measurement was done in Gatan Microscopy Suite (GMS) version 3 using the profile tool [55]. The spacing between the direct and diffracted spot was measured, and then the distance between the minima in the diffracted beam. Figure 3.3 illustrates an example of how it is done. These values were put into a Python script written by PhD student Christoph Hell, which calculated the thickness of the sample using equations (2.39) and (2.43) [56]. The volume of the specimen V_i in image i is given by,

$$V_i = \frac{A_i t_i}{M_i^2},$$ (3.2)

where M_i is the magnification of the image. The volume's relative error is given by Gaussian error propagation:

$$\frac{\Delta V_i}{V_i} = \sqrt{\left(\frac{\Delta A_i}{A_i}\right)^2 + 4\left(\frac{\Delta M_i}{M_i}\right)^2 + \left(\frac{\Delta t_i}{t_i}\right)^2}.$$ (3.3)
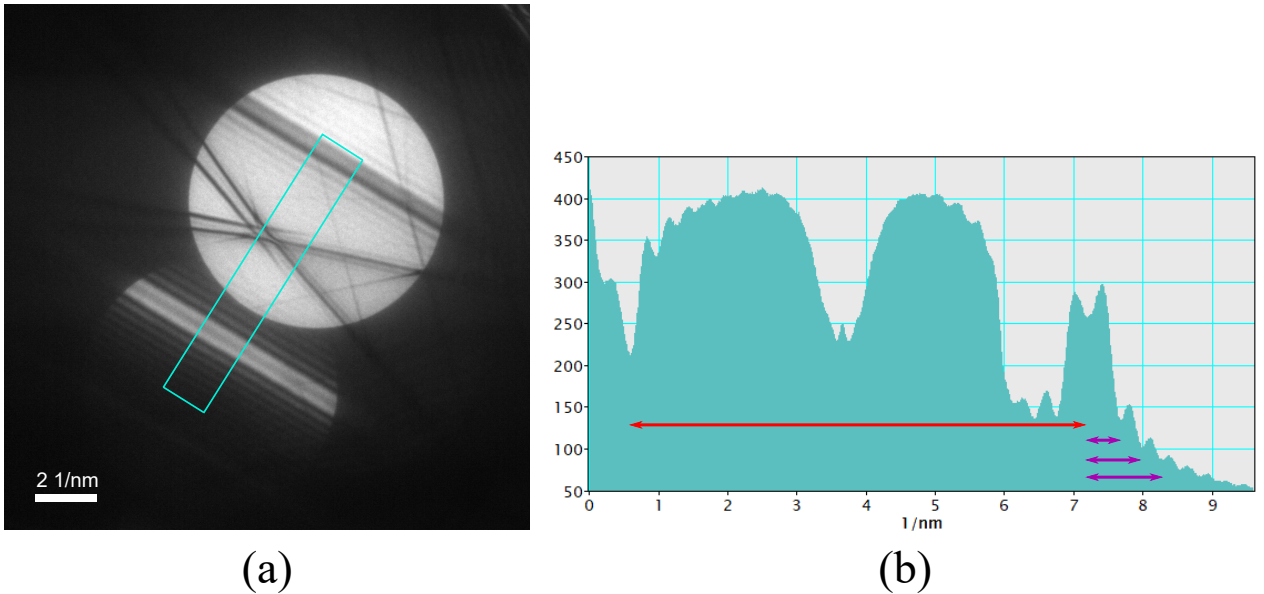

Figure 3.3: (a) A CBED image in the two-beam condition. The turquoise rectangle comes from using the GMS 3 profile tool. (b) The intensity profile given by the turquoise rectangle. Measuring the red line gives the spacing between the direct and diffracted spot. Measuring the purple lines gives the spacing between the first three minima.

Before calculating the remaining quantities, some geometrical corrections must be done. For a thin specimen, the measured precipitates might not be entirely included in the volumes V_i because they could have been partly cut during sample preparation. This requires a geometrical correction to the precipitate length and the precipitate number density. One must first know the total tilt angle Φ given by,

$$\Phi = \arccos\left(\cos\phi_x \cdot \cos\phi_y\right), \tag{3.4}$$

so that one knows which plane the precipitates were cut in. The azimuth angle θ shown in Figure 3.4(a) is assumed to be 45° in this case since the precipitates in both [100] and [010] directions had similar lengths and therefore cut equally as much. For more details on the relationship between Figures 3.4(a) and (b) and the following formulas for the corrected quantities, see [52].

The equation for the adjusted precipitate length in image i is given by,

$$\langle l \rangle_i = \frac{\langle l \rangle_{m_i}}{1 - \frac{\langle l \rangle_{m_i}}{t} \cos\theta \tan\Phi}, \tag{3.5}$$

with relative error given by,

$$\frac{\Delta\langle l \rangle_i}{\langle l \rangle_i} = \frac{\langle l \rangle_{m_i}}{t} \cos\theta \tan\Phi. \tag{3.6}$$

Subsequently, $\langle l \rangle$ and $\Delta\langle l \rangle / \langle l \rangle$ were calculated across all images for each condition.
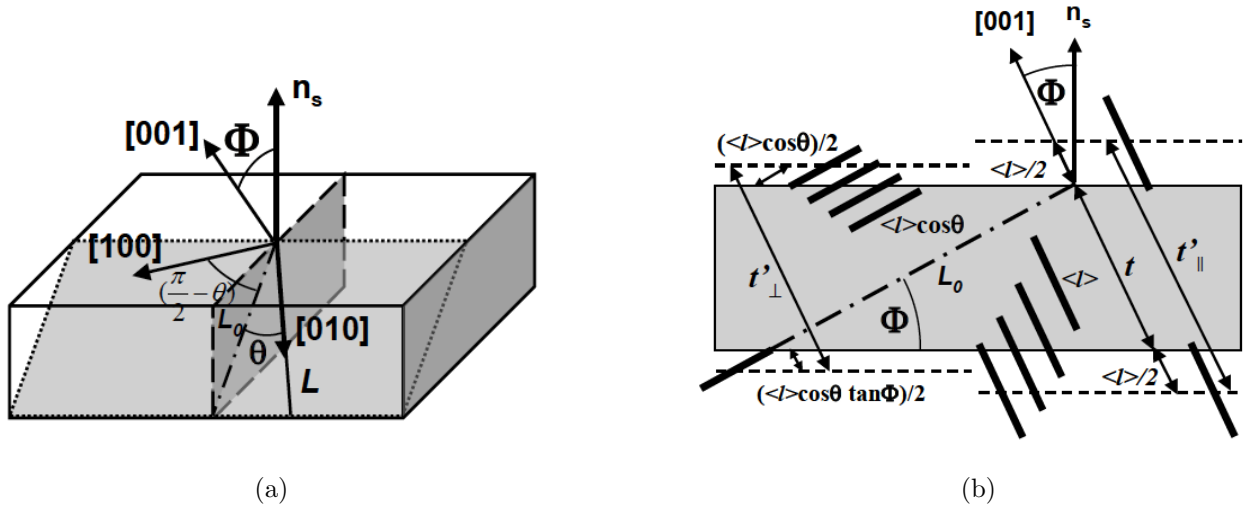

(a)   (b)

Figure 3.4: Illustration of the total tilt angle Φ, the azimuth angle θ, and the geometrical corrections needed to take into account the cut precipitates. Figures taken directly from [52].

Equation (3.5) is used in the formula for the adjusted precipitate number density which for an image i is given by,

$$\rho_i = \frac{3N_i}{A_i(t_i + \langle l \rangle_i)}, \tag{3.7}$$

where equation (3.6) is used in the formula for the relative error for ρ_i given by,

$$\frac{\Delta\rho_i}{\rho_i} = \sqrt{\left(\frac{\Delta N_i}{N_i}\right)^2 + \left(\frac{\Delta V_i'}{V_i'}\right)^2} = \sqrt{\left(\frac{\Delta N_i}{N_i}\right)^2 + \left(\frac{\Delta V_i}{V_i}\right)^2 + \frac{\left(\frac{\Delta\langle l \rangle_i}{\langle l \rangle_i}\right)^2 + \left(\frac{\Delta t_i}{t_i}\right)^2}{\left(1 + \frac{t_i}{\langle l \rangle_i}\right)^2}}. \tag{3.8}$$

Finally, the average precipitate number density across all images for each condition $\langle \rho \rangle$ was calculated, and together with the previously calculated $\langle CS \rangle$ and $\langle l \rangle_{\mathrm{m}}$ the volume fraction VF was deduced using,

$$VF = \langle CS \rangle \langle l \rangle_{\mathrm{m}} \langle \rho \rangle, \tag{3.9}$$

with its relative error given by Gaussian error propagation:

$$\frac{\Delta VF}{VF} = \sqrt{\left(\frac{\Delta \langle CS \rangle}{\langle CS \rangle}\right)^2 + \left(\frac{\Delta \langle l \rangle_{\mathrm{m}}}{\langle l \rangle_{\mathrm{m}}}\right)^2 + \left(\frac{\Delta \langle \rho \rangle}{\langle \rho \rangle}\right)^2}. \tag{3.10}$$

The five parameters VF, $\langle CS \rangle$, $\langle \rho \rangle$, $\langle l \rangle_{\mathrm{m}}$ and $\langle l \rangle$ and their error estimates for the four conditions in Table 3.2 were reported and compared.

3.6.2 SPED Data Processing and Analysis

Based on the results from the precipitate quantification, the conditions chosen to be studied with SPED were **0-48** and **20-48**. Two datasets were acquired for **0-48** because only half of the first dataset was fit for use due to a high total tilt angle. This introduced a sample height difference which destroyed the quality of half of the dataset. One dataset was acquired for **20-48**, and all three datasets were processed and analyzed. The acquired SPED datasets were quite large ($\sim$20 GB), which meant that the data processing had to be done post-session using a custom built computer with 256 GB RAM and AMD Ryzen Threadripper 3970X processor with 32 cores, 64 threads and 3.7-4.5 GHz computation speed. As mentioned before in Section 2.3.4, a SPED dataset is four-dimensional with a scanned 2D area in real space where for each position a 2D reciprocal space pattern is recorded. More specifically, the datasets obtained by Dr. Sigurd Wenner have a size of (400 x 400) pixels, where each pixel is associated with a single PED pattern containing (256 x 256) pixels.

The open source Python libraries PyXem and HyperSpy were used to process and interpret the 4D dataset [57, 58]. One of HyperSpy's features is the ability to create *virtual* BF (VBF) and DF (VDF) images from a PED pattern. This function can be compared to inserting a real aperture into the TEM, and selecting the parts of the beam that forms the BF or DF image. In place of a physical aperture, HyperSpy can create a *virtual aperture* (VA) and the user can determine its size and placement in the PED pattern stack. HyperSpy then integrates the total electron intensity of the PED pattern that lies within the VA, and assigns a colour value to the PED pattern's matching real space position. While keeping the VA fixed, this process is repeated throughout the entire PED stack until one obtains a VBF or VDF image. The placement of the VA determines which part of the virtual image is highlighted, as demonstrated in Figure 3.5.
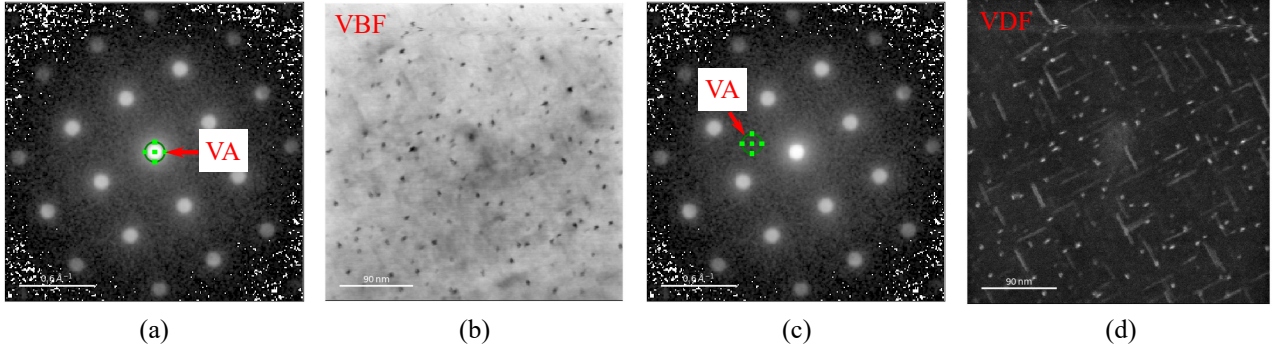
Figure 3.5: Images showing how the placement of a virtual aperture changes the virtual image. (a) The VA is situated at the (000) reflection, resulting in (b) a VBF image. (c) The VA is situated between (000) and the first Al reflections, resulting in (d) a VDF image of precipitates scattering in between Al reflections.

Phase Mapping With SPED

The Jupyter Notebook used for phase mapping was a combination of new code, a notebook written by senior engineer Dr. Emil Frang Christiansen and another notebook written by PhD student Elisabeth Thronsen. The Jupyter Notebook can be found in Appendix C. The three SPED datasets were pre-processed by a program written by Emil Frang Christiansen where they were converted to HyperSpy files. The SPED calibration was performed according to Appendix B. Each of the two and a half datasets was processed individually in the notebook. After loading a dataset into the notebook, a central beam alignment routine was performed. The bulk Al reflections in the PED stack were detected by a Scikit-image *blob detection* function and covered [59]. This can be referred to as a *signal mask* and its purpose was to enhance the signal from precipitates. A second circular cutoff mask was applied to cover the PED reflections outside of the 9 central Al reflections where precipitate reflections are too weak to be analyzed, and its purpose was to reduce the computation time.

The SPED datasets contained $\leq$160k individual PED patterns, but not all of them are unique. To obtain a phase map, one has to decompose the dataset into its unique patterns. Therefore *machine learning* was implemented to identify the main *component patterns*, which are diffraction patterns that show up throughout the dataset and are unique (e.g. precipitate phases). Component maps, also known as factor maps, come in pairs with the *loading maps* which illustrate the real space location from which the component pattern originates. Loading maps can be compared to VDF images constructed from a VA, but the difference is that they are obtained through automated machine learning. HyperSpy has many *data matrix decomposition* algorithms, also known as *factorization* algorithms, but the two algorithms implemented in this thesis were *singular value decomposition* (SVD) [60] and *non-negative matrix factorization* (NMF) [61].

To get a better understanding of the number of unique components in the dataset, SVD was performed on the datasets, first with maximum rank = 80 to obtain a *scree plot*. The scree plot shows the fraction of total variance belonging to each component in the dataset. The strategy used to determine an approximation of the correct rank was to recognize the location where the variance drops and becomes relatively low, such that in ideal cases the plot looks like an elbow or a knee [39]. This strategy assumes

that the signals are corresponding to high variance in the data, while noise corresponds to low variance. The drop in variance is interpreted as the transition between signal and noise. Based on the results from the scree plots, NMF was performed on the datasets with a lower maximum rank. In comparison to SVD, NMF forces the component and loading maps to be strictly non-negative, generating results that can be physically interpreted. Through trial-and-error, the correct maximum rank and therefore the correct number of components for each dataset was found and a phase map was generated.

Strain Mapping With SPED

The datasets analyzed for strain mapping were the same pre-processed datasets used for phase mapping, and were similarly processed individually. The Jupyter Notebook used for strain mapping was written by a previous master student Ingeborg Nævra Prestholdt [62]. It was altered slightly to suit the datasets obtained, including a central beam alignment routine and background subtraction. The adapted notebook can be found in Appendix D. A reference region without precipitates of (20 x 20) pixels was chosen, the mean intensity throughout the PED stack was calculated and the DP plotted. The averaging of DPs was done to eliminate local DP variations. The Al peak x- and y-positions were located manually from the DP and inserted into the code. Two pairs of peaks were chosen for strain mapping, the first pair being the (200) and ($\bar{2}$00) reflections and the second being the (020) and (0$\bar{2}$0) reflections. Each pair lay opposite each other with the central beam between them: one in the x-direction and one in the y-direction. The region chosen for strain mapping was the whole available real space region in the dataset. To determine the displacement of the Al peak positions due to strain, the code had to first precisely find the center of the peaks. This was done using a *center of mass* (CoM) algorithm from a PyXem library called SubpixelrefinementGenerator, a method with sub-pixel precision. The conventional cross-correlation and Gaussian fitting algorithms were attempted as well, but they did not work as well as the CoM algorithm.

The CoM of an object is the average position of all weighted pieces of the system, where the sum of the weighted position vectors adds up to zero. The positions can be weighted based on mass for a physical object, but for a DP peak, it is weighted based on intensity. The peaks in PED patterns have a disc shape, and the assumption is that the center of the discs lies at the center of intensity. The CoM formula for one dimension is given by,

$$|R| = \frac{\sum_{i=0}^{n} m_i r_i}{\sum_{i=0}^{n} m_i}, \tag{3.11}$$

where $|R|$ is the CoM position, r_i and m_i are the position and weight of an element i in the system, and n is the total number of elements [63]. To find the CoM of a DP disc, the user selects a square with an edge length large enough to accommodate the size of the disc. The algorithm calculates the sum of intensities of each pixel, and the CoM in the x- and y-direction is computed separately. The position of the CoM for the two pairs of peaks chosen for strain mapping is computed for each PED pattern in the stack. The drift between the two pairs of peaks is calculated in the strained and unstrained reference region, making it possible to compare the displacements to obtain a strain map.

Background subtraction was performed on the real space strain maps for the three SPED datasets using a Scikit-image function called *threshold local* [59]. The function creates a threshold mask on the image based on the local neighbouring pixels. All the pixels in the input image that have a higher value than the corresponding pixels in the threshold image are considered foreground, so the threshold

image is considered background. Substracting the threshold image from the original image gives the background subtracted image. An example of this process is presented in Figure 3.6. Unless stated otherwise, all the real space strain maps are processed this way.

Original image   Background   Background subtracted image
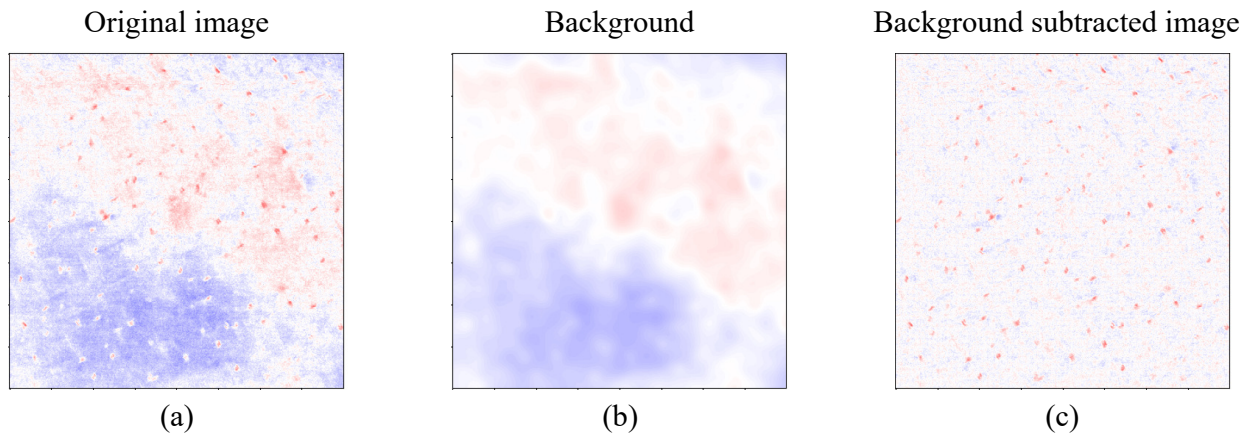

(a)   (b)   (c)

Figure 3.6: In (a) an unprocessed strain map is shown. The background of (a) acquired using Sci-kit image is shown in (b). The background was subtracted from the original image, giving (c).

3.6.3 Image Processing and Analysis

Most of the TEM images presented in this thesis are not displayed in their original form, but are processed to highlight the interesting information one can glean from them. HyperSpy or GMS 3 were utilized to adjust gamma, brightness and contrast [55, 58]. Gamma determines the brightness of each pixel, but in a non-linear way. The HAADF-STEM images were filtered by taking the Fast Fourier Transform (FFT), applying a circular band pass mask to the FFT, and taking the Inverse Fast Fourier Transform (IFFT) of the masked FFT. An example of this process is illustrated in Figure 3.7. Unless stated otherwise, all HAADF-STEM images are filtered this way.

Original Fast Fourier Transform (FFT) Low-pass filtered FFT Inverse Fast Fourier Transform (IFFT)
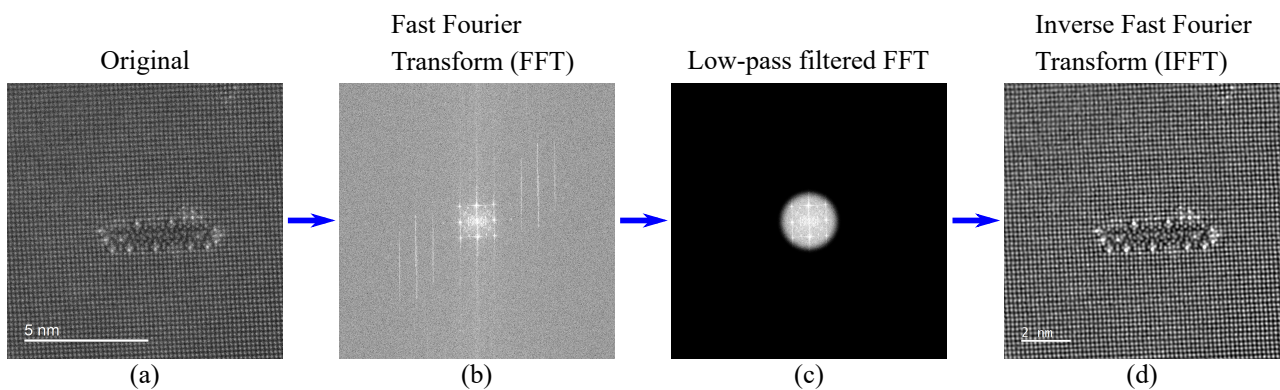
(a)   (b)   (c)   (d)

Figure 3.7: In (a) an unfiltered HAADF-STEM image is shown. The FFT of (a) is shown in (b). A mask was applied to (b) which gave the low-pass filtered FFT in (c). In (d) the IFFT of (c) is shown.

The purpose of FFT filtering was to reduce noise before importing the images into the new AutomAl 6000 software tool [64]. This software was used to determine the 3D column positions and column species of the precipitates in the acquired HAADF-STEM images. For more information on the

methodology of AutomAl 6000, consult [65]. The data from AutomAl 6000 was exported as a *scalable vector graphics* (SVG) file and imported into Inkscape [66]. Lastly, the images were skewed to correct the non-perpendicular bulk Al lattice and the overlay was exported.

4 Results

This chapter is divided into several sections. First, the hardness curves for the investigated samples, followed by an investigation of the microstructure of the four TEM conditions, including BF-images and precipitate statistics. This is followed by a section with HRTEM images, and then HAADF-STEM images, both to study the crystal structure of the precipitates. Lastly, the results from phase mapping and strain mapping utilizing SPED are presented.

4.1 Hardness Curve

The hardness of the alloy was measured for the 26 different conditions, as explained in Section 3.3. The results were plotted using a logarithmic time scale in Figure 4.1. The arrows indicate the four conditions studied with TEM: the blue arrows for the **0-6** and **0-48** conditions, and the green arrows for the **20-6** and **20-48** conditions. The hardness curve shows that the longer the samples lie in the oven, the harder they are up to peak hardness, which is at 48 h. However, the different NA times lead to the curves having different slopes.
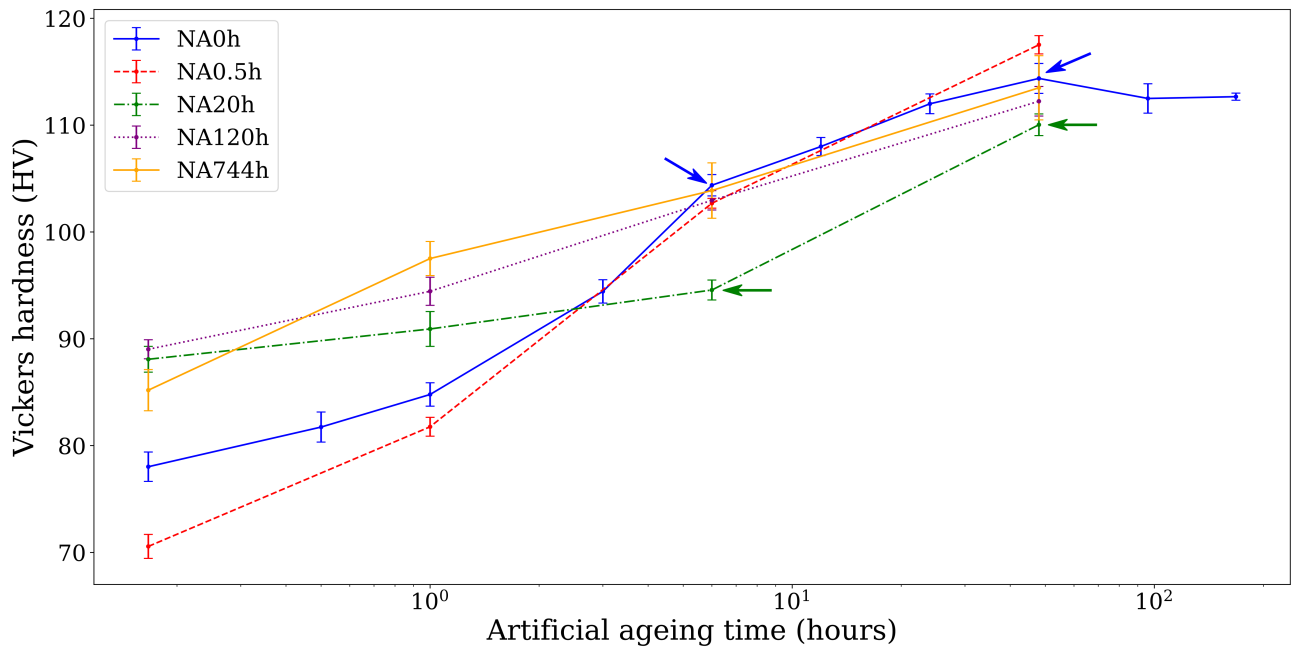

Figure 4.1: Hardness of the five different natural ageing times plotted as a function of artificial ageing times, a total of 26 conditions. The error bars are given as two standard errors. The arrows represent the four different conditions where TEM studies were conducted. The time scale is logarithmic.

4.2 Microstructure

Figure 4.2 show BF-images of the four conditions taken at x400k magnification. The images give an overview of the precipitate microstructure and show a qualitative comparison of the precipitate cross-sections shapes for these four conditions. Comparing Figure 4.2(a) and (b) the peak-aged conditions, one can see that the **20-48** condition has more lath-shaped precipitates, while the **0-48** condition has more rod-shaped precipitates. The difference is not as great when comparing Figure 4.2(c) and (d), but the **20-6** condition has a few more precipitates with elliptical cross-sections.

Figure 4.2: BF-images of the four conditions. (a) for condition **0-48**. (b) for condition **20-48**. (c) for condition **0-6**. (d) for condition **20-6**. Al orientation in (a) applies for all images. The thicknesses of the imaged areas are unknown, but comparable.

Figure 4.3 show BF-images of the four conditions taken at x200k magnification. The thicknesses of the areas the images were taken from are included. The thicknesses were found using the method explained in Section 3.6.1. Comparing Figure 4.3(a) and (b) the peak-aged conditions which have similar thickness, one can see that the **0-48** condition has a higher precipitate number density than the **20-48** condition. The areas in Figure 4.3(c) and (d) for the underaged conditions have similar thicknesses as well. The precipitate number density is higher for the **0-6** compared to the **20-6** condition.

0-48 (t = 123 nm)   20-48 (t = 118 nm)
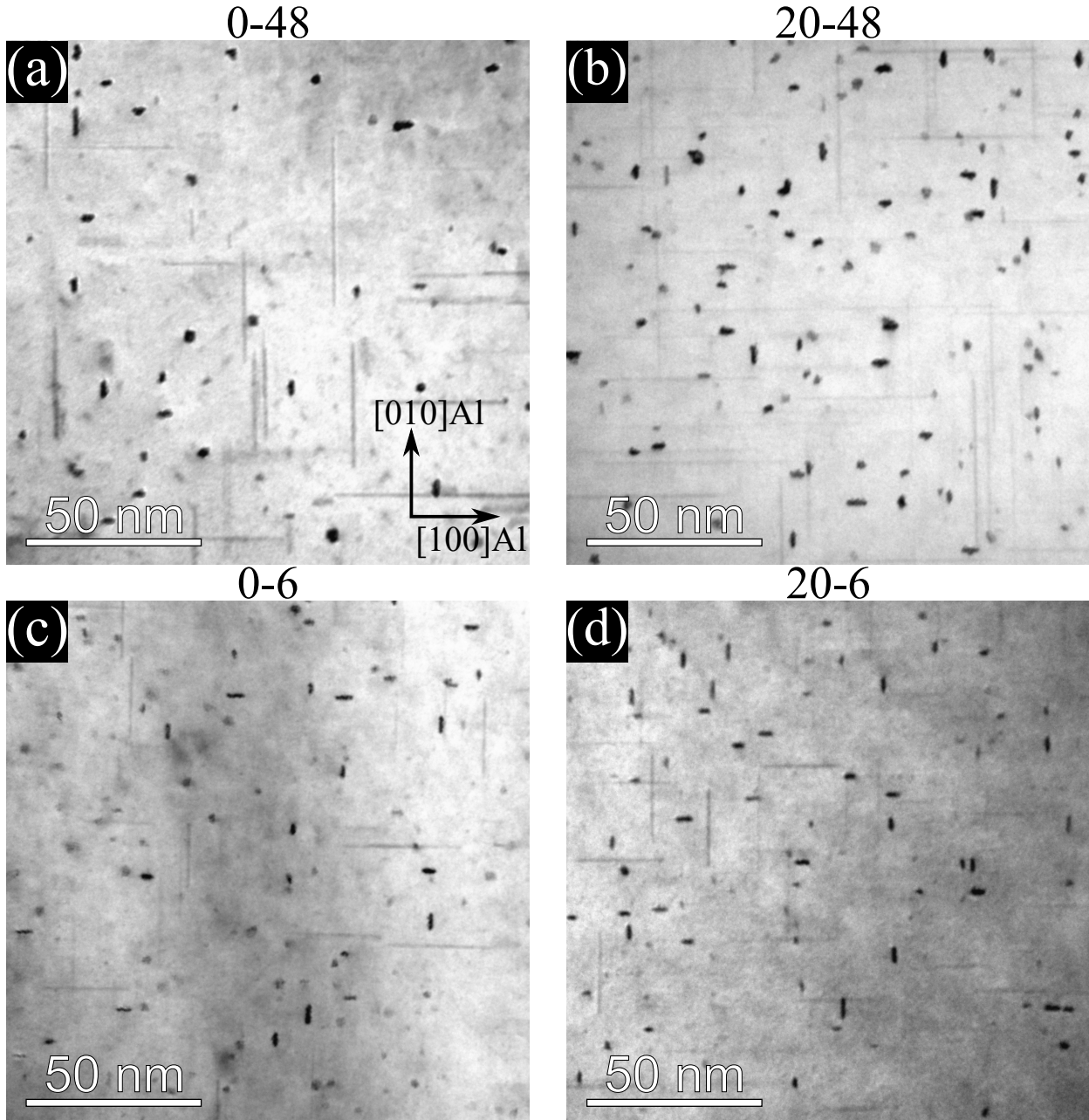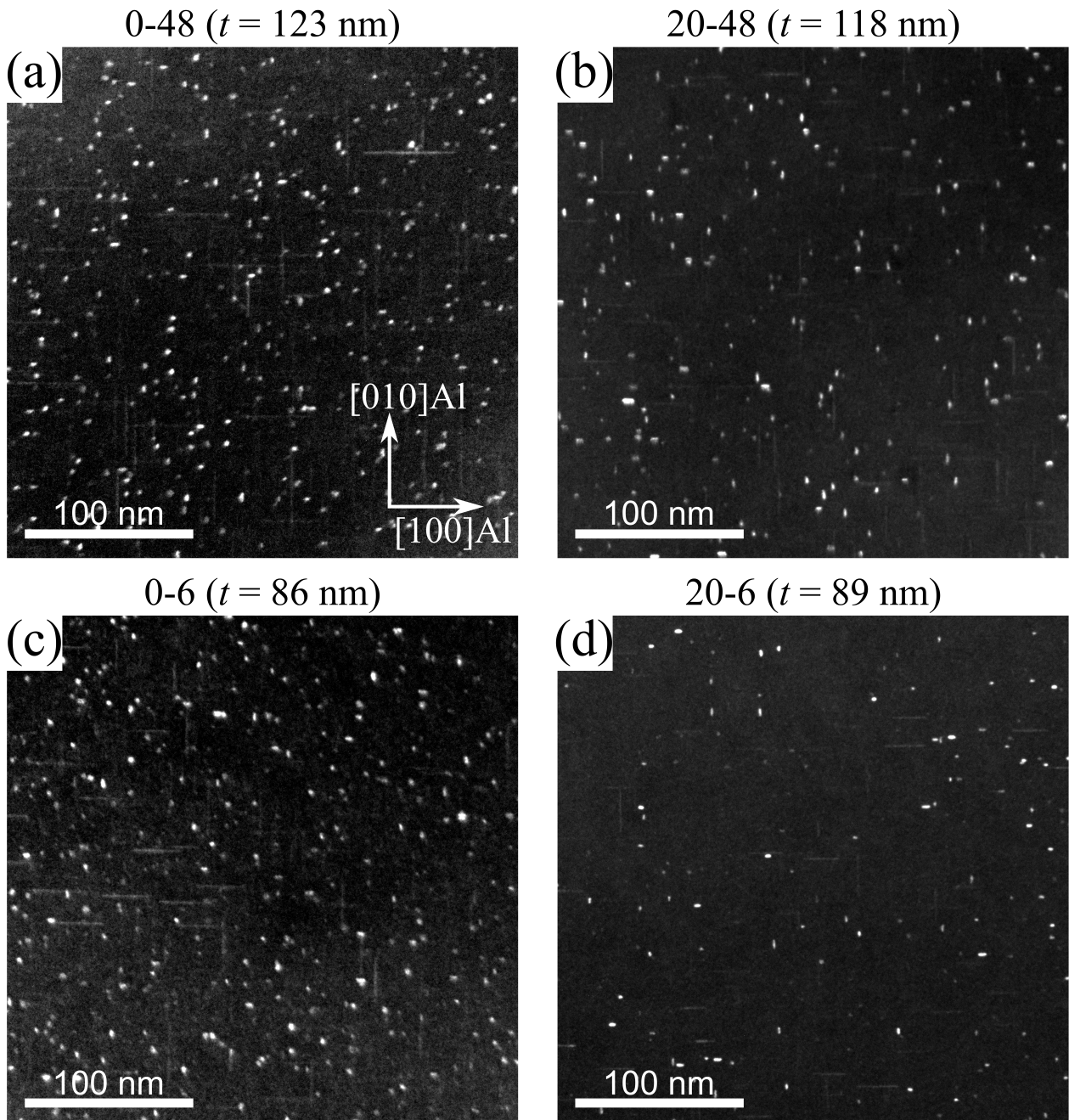
0-6 (t = 86 nm)   20-6 (t = 89 nm)

Figure 4.3: DF-images of the four conditions. (a) for condition **0-48**. (b) for condition **20-48**. (c) for condition **0-6**. (d) for condition **20-6**. Al orientation in (a) applies for all images. The thickness t is given above each image.

The calculated precipitate statistics for the four conditions are presented in Table 4.1. Comparing the peak-aged conditions **0-48** and **20-48**, one sees that the VF, $\langle\rho\rangle$, $\langle l\rangle_{\mathrm{m}}$, $\langle l\rangle$ are higher for the **0-48** condition. The average cross-section area is similar for the two. Comparing the underaged conditions **0-6** and **20-6**, it is also the case that VF, $\langle\rho\rangle$, $\langle l\rangle_{\mathrm{m}}$, $\langle l\rangle$ are higher for the condition without NA. However, the difference in the average precipitate length, both measured and geometrically corrected, is not as great. The average cross-section area is also similar for the two.

Table 4.1: Calculated precipitate statistics and errors for the four conditions.

Variable	0-48	20-48	0-6	20-6
VF (%)	1.21 ± 0.11	0.75 ± 0.06	0.69 ± 0.05	0.48 ± 0.04
$\langle CS\rangle$ (nm^2)	5.1 ± 0.2	5.0 ± 0.2	4.3 ± 0.1	4.6 ± 0.2
$\langle\rho\rangle$ (µm^{-3})	$(70 \pm 4)\cdot 10^3$	$(60 \pm 4)\cdot 10^3$	$(70 \pm 3)\cdot 10^3$	$(49 \pm 3)\cdot 10^3$
$\langle l\rangle_{\mathrm{m}}$ (nm)	33.9 ± 2.1	25.1 ± 0.5	23.3 ± 1.2	21.6 ± 1.3
$\langle l\rangle$ (nm)	34.8 ± 2.3	25.5 ± 0.5	23.6 ± 1.2	21.7 ± 1.3

Figure 4.4 shows histograms of the measured precipitate lengths for the four conditions. The histogram of the **0-48** condition has a greater spread than the others and its center has a higher precipitate length value. The center of the **0-6** and the **20-6** histogram are quite similar, while the center of the **20-48** histogram lies further to the right.
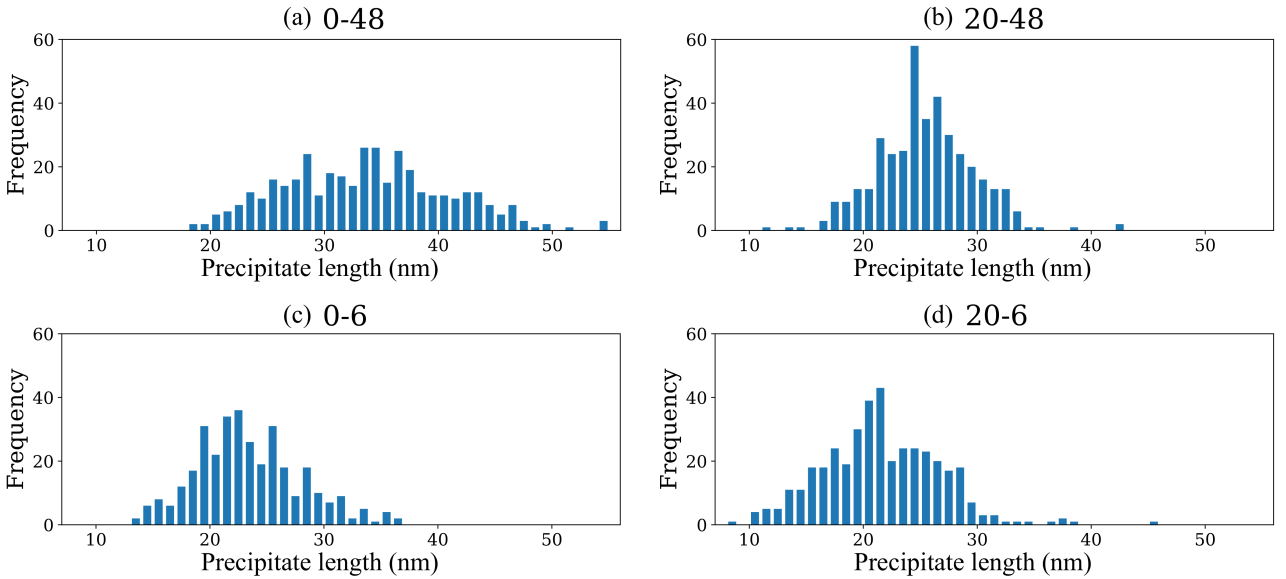

Figure 4.4: Histograms of the measured precipitate lengths for the four conditions.

As mentioned previously in Section 3.6.1, the major and minor axis of precipitates were measured and the aspect ratio was calculated by dividing the major axis by the minor axis. For perfectly circular precipitates, their aspect ratio = 1. For the four conditions, Figure 4.5 shows normalized heat maps of the aspect ratio as a function of the angle between the major axis and the x-axis of the images, denoted as the azimuth angle. The angles were adjusted to compensate for the differences in rotation of the Al lattice in the TEM images, placing the peaks at $45°$ and $135°$. From the peak-aged conditions, one can

see that more precipitates have an aspect ratio ~ 1 in (a) across all angles compared to (b). However, the heat map in (b) lights up more strongly than (a) close to the 45° and 135° peaks, suggesting that more precipitates with an elliptical cross-section are present in this condition. The underaged conditions in (c) and (d) have less of a difference, but (c) also has precipitates with aspect ratio ~ 1 across all angles. The heat map in (d) has few precipitates between 72° and 108°, and the peaks are brighter than in (c) which also suggests slightly more precipitates with an elliptical cross-section in the **20-6** condition. All four heat maps show that most lath-shaped precipitates lie 90° to each other in the Al matrix.
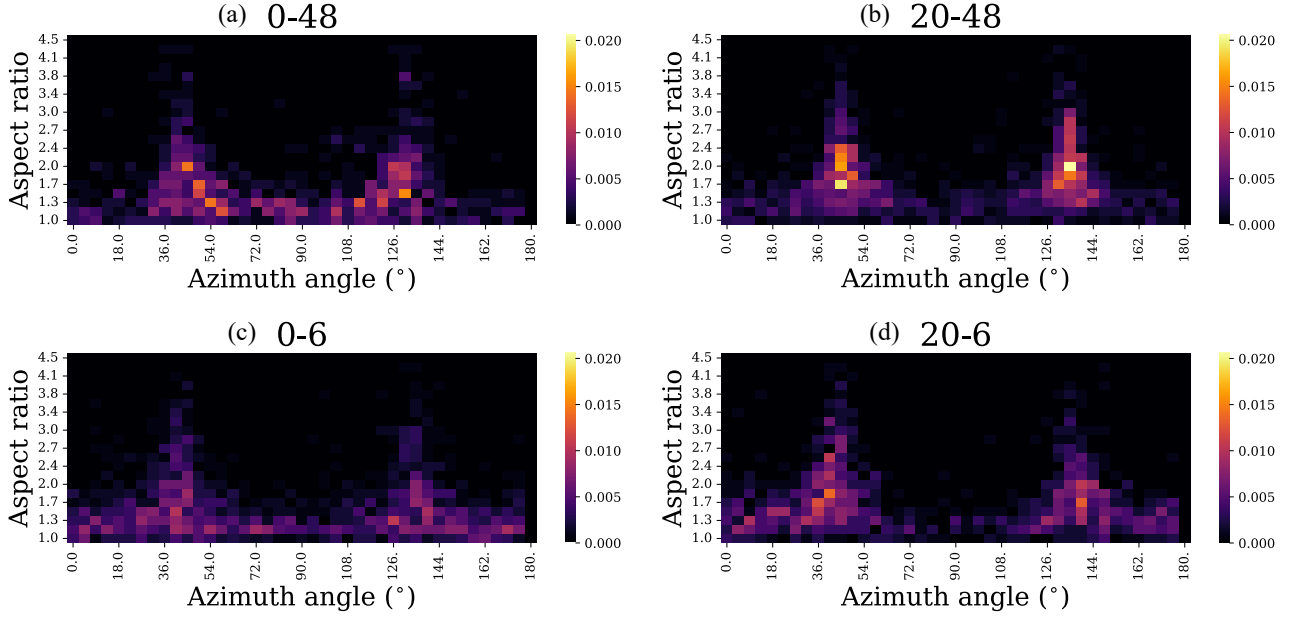

Figure 4.5: Normalized heat maps of aspect ratio and azimuth angle for the four conditions. Angles were adjusted to compensate for differences in rotation of the Al lattice in the TEM images.

The average aspect ratio and standard deviation were calculated across $0.5\,\mathrm{nm}^2$ intervals of cross-section area, and the result is presented in Figure 4.6. A linear fit of the average aspect ratio is plotted in these figures as well. To give an understanding of where precipitates with circular cross-sections would lie on the graph, a horizontal line of aspect ratio = 1 is included. For the **20-48** and **20-6** conditions with NA, the linear fit has a positive slope, suggesting that the aspect ratio of the precipitates increases as the cross-section area increases. This could mean that precipitates which have grown to a larger size are more cylindrical without NA and more plank-shaped with NA.
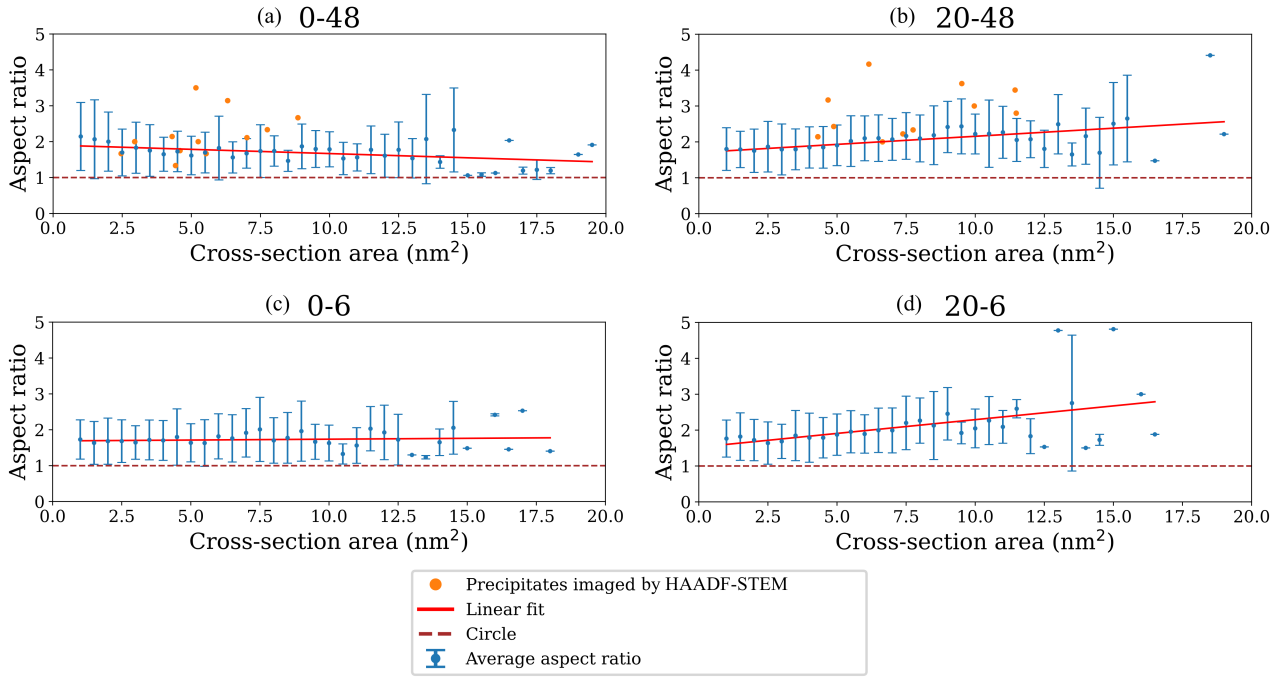
Figure 4.6: Plot of average aspect ratio across several intervals of width $0.5\,\mathrm{nm}^2$ of cross-section area. The error bars represent the standard deviation. A linear fit of the average aspect ratio is included. Precipitates imaged by HAADF-STEM were measured manually and plotted for the peak-aged conditions. A horizontal line of aspect ratio = 1 is plotted to show where precipitates with circular cross-sections would lie.

The major and minor axes lengths and cross-section area of the precipitates imaged by HAADF-STEM were measured manually by counting atomic columns, and ten of these precipitates were measured with Fiji as well. When measuring the cross-section area manually, one usually assumes the cross-section to be rectangular in shape for lath-shaped precipitates. Therefore the cross-section area was approximated by multiplying the major and minor axes' lengths. The precipitates that were measured manually are represented by orange dots in Figure 4.6. The HAADF-STEM images of the first two precipitates from each condition are shown in Section 4.4. The remaining six precipitates are presented in Appendix A.3. Table 4.2 illustrates the difference between the results from measuring with Fiji and measuring manually. For the aspect ratio measurements, the difference in results is quite similar with under a 19 % difference. For the cross-section area measurements, the difference is significant where the greatest percentage difference is 59 %.

Table 4.2: The cross-section area and the aspect ratio of a selection of precipitates imaged by HAADF-STEM measured manually and with Fiji.

Precipitate nr.	Condition	Measured manually		Measured with Fiji	
		CS (nm^2)	Aspect ratio	CS (nm^2)	Aspect ratio
1	**0-48**	5.5	1.7	3.0	1.6
2	**0-48**	8.9	2.7	6.2	2.7
3	**0-48**	7.0	2.1	4.0	2.1
4	**0-48**	6.3	3.1	5.3	2.6
5	**0-48**	5.2	3.5	4.0	3.0
1	**20-48**	4.7	3.2	2.8	2.9
2	**20-48**	9.5	3.6	5.8	3.7
3	**20-48**	8.0	4.0	5.8	3.3
4	**20-48**	3.7	2.5	2.8	2.4
5	**20-48**	6.0	3.0	6.3	3.0

4.3 HRTEM

Figure 4.7(a) and (c) show HRTEM images of L phase precipitates from the **0-48** and **20-48** conditions, respectively. Their corresponding FFTs are shown in Figure 4.7(b) and (d). Since the L phase is disordered, it can only be recognized by the appearance of the projected hexagonal Si-network aligned along the $\langle 100 \rangle$ Al direction. In the FFT, there is usually an elongation/smearing of spots on both sides of the central spot as well. Other precipitates imaged using HRTEM from these conditions appeared similar and were determined to be the L phase as well. See Appendix A.1 for more HRTEM images.
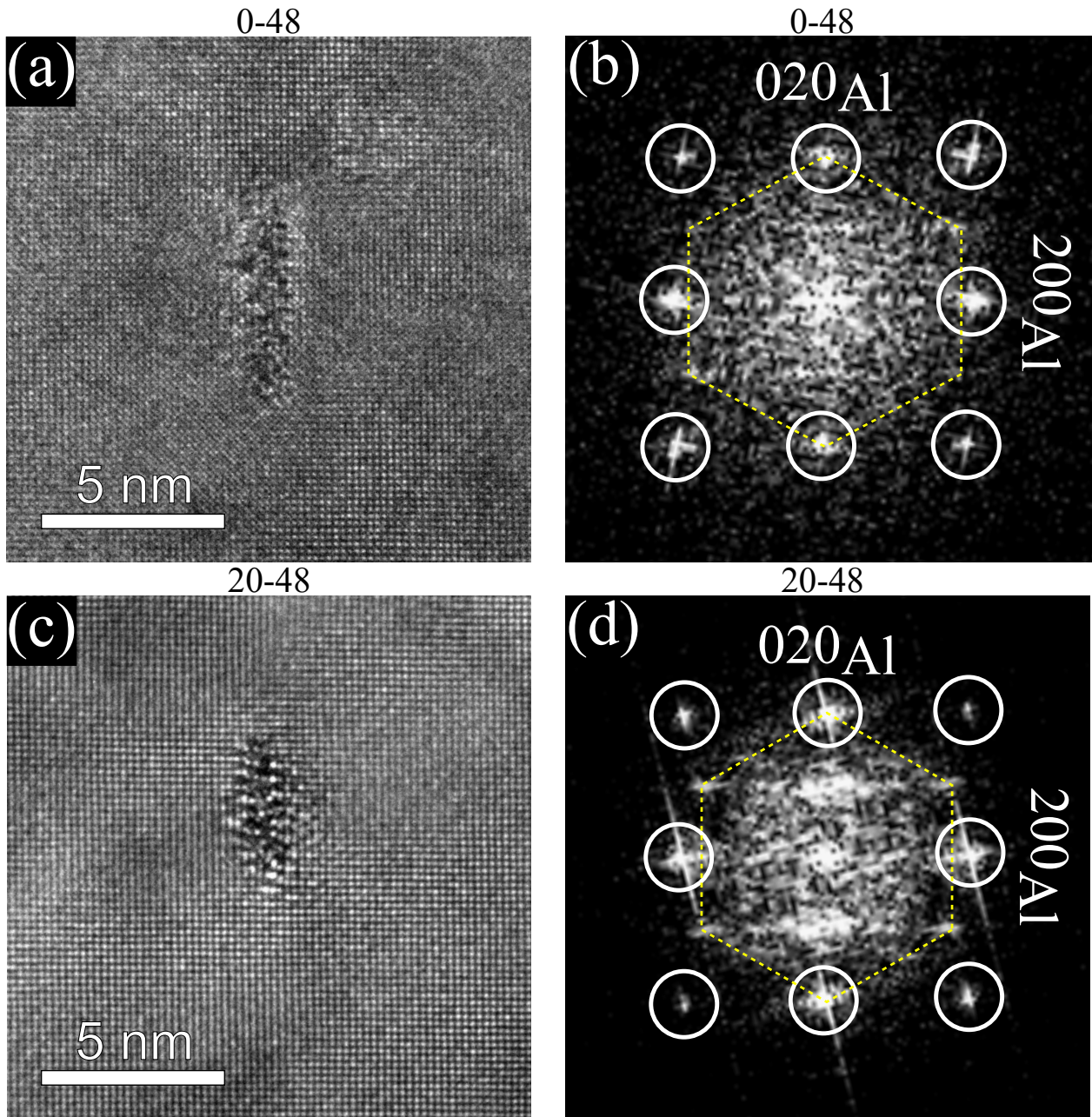
Figure 4.7: (a) HRTEM image of the L phase from the **0-48** condition and its FFT in (b). (c) HRTEM image of the L phase from the **20-48** condition and its FFT in (d). The Al reflections are marked with white circles, except for the center spot. The Si-network is marked with yellow dashed lines.

4.4 HAADF-STEM

A selection of HAADF-STEM images of precipitates from the peak-aged conditions **0-48** and **20-48** are shown in Figures 4.8 and 4.9, respectively. Their corresponding FFTs are also presented here with the Si-network visible. The precipitates were overlaid using AutomAl 6000 as mentioned in Section 3.6.3 and the legend for these overlaid images are presented in Table 4.3.

Table 4.3: Legend for the overlay images presented in this section, where z is the longitudinal displacement and a is the Al lattice constant = 4.05 Å.

Element	$z = 0$	$z = a/2$
Al	🟢	🟢
Cu	🟡	🟡
Mg	🟣	🟣
Si	🔴	🔴
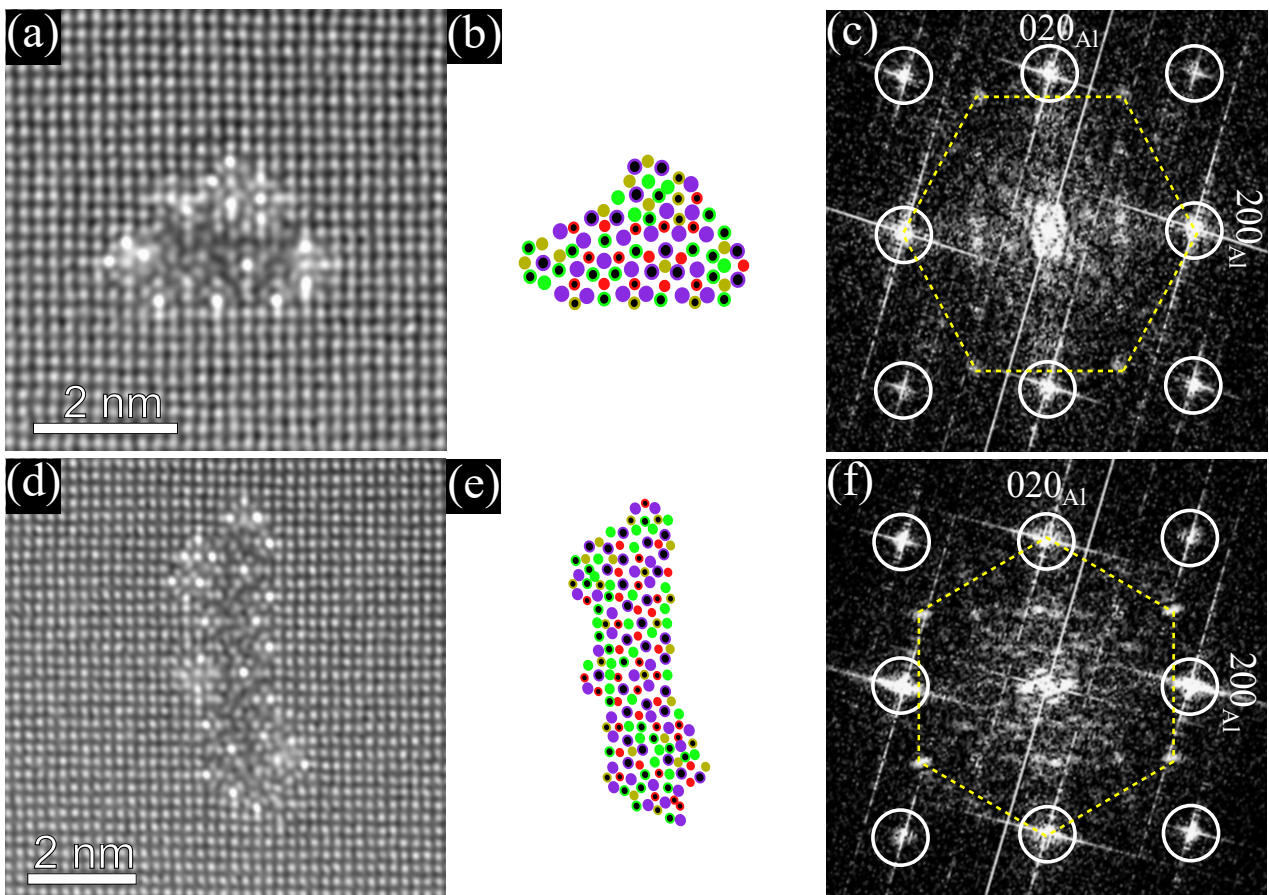
Figure 4.8: HAADF-STEM images in (a) and (d) for the **0-48** condition. Overlays in (b) and (e) with the same scale bar as in (a) and (d), respectively. The FFTs of (a) and (d) are shown in (c) and (f), respectively. The Al reflections are marked with white circles, except for the center spot. The Si-network is marked with yellow dashed lines. The HAADF-STEM images were obtained by Dr. Sigurd Wenner.
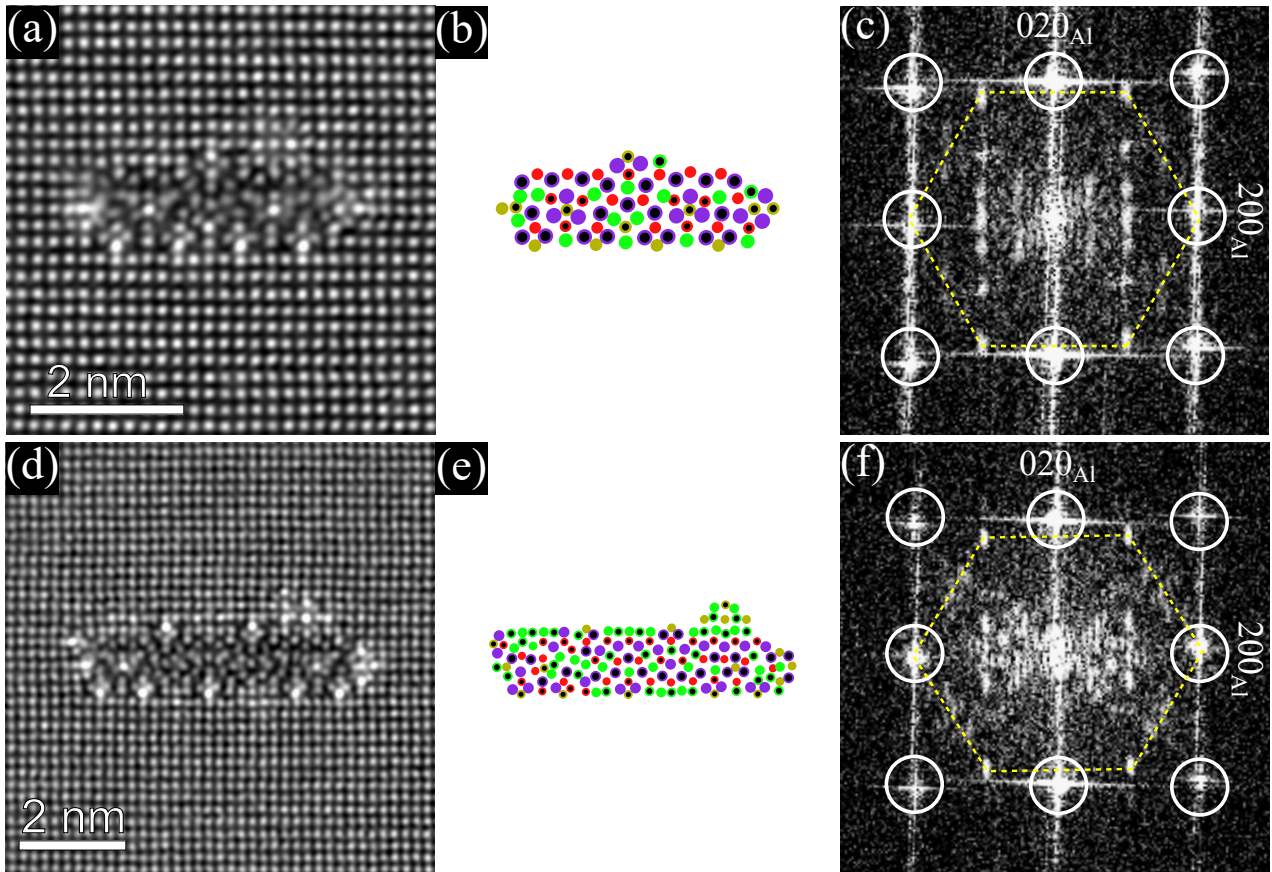
Figure 4.9: HAADF-STEM images in (a) and (d) for the **20-48** condition. Overlays in (b) and (e) with the same scale bar as in (a) and (d), respectively. The FFTs of (a) and (d) are shown in (c) and (f), respectively. The Al reflections are marked with white circles, except for the center spot. The Si-network is marked with yellow dashed lines. The HAADF-STEM images were obtained by Dr. Sigurd Wenner.

4.5   Phase Mapping With SPED

The maximum of the SPED datasets was taken using Hyperspy's function called *max*, which iterates through the entire PED stack and finds the pixel with the highest intensity over the specified axes. This returns an image which contains the pixels with maximum intensity throughout the stack and will show reflections of all phases present in the datasets, regardless of how rarely the phases appear. Figure 4.10 shows the maximum results from the obtained SPED datasets: one from the **20-48** condition and two from the **0-48** condition. The two SPED datasets from the **0-48** condition were taken from two different samples. They are denoted by Sample 1 and Sample 2 to differentiate between the two datasets. There are more spots in Figure 4.10(b) compared to (a) and (c), which points to there being an extra phase in (b).
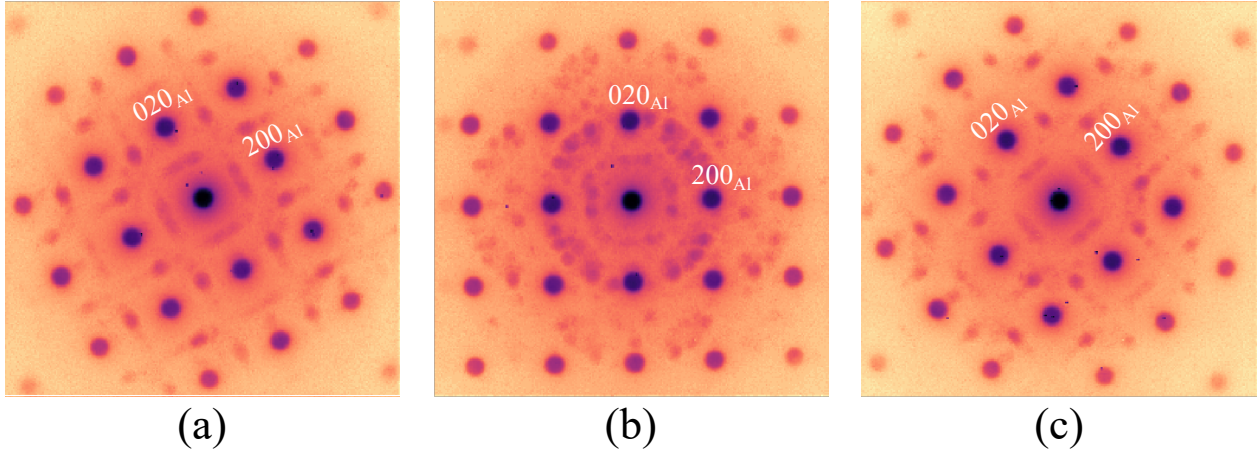
Figure 4.10: The maximum taken through the entire SPED dataset. (a) for condition **20-48**. (b) for Sample 1 of condition **0-48**. (c) for Sample 2 of condition **0-48**. The contrast has been inverted.

To investigate the origin of the individual patterns in Figure 4.10, the three datasets were processed with NMF decomposition. Figure 4.11 show the relevant components given by NMF decomposition for Sample 1 from the **0-48** condition. The loading maps are presented (a), (c), (e), (g) and (i), and the factor maps are presented in (b), (d), (f), (h) and (j). One can see that the factors in (b) and (d) are 90° rotations of each other. This is also the case for the factors in (f) and (h). The precipitates giving the signal in the (b) and (d) factor maps also show the Si-network and were determined to be the L phase. The precipitates with the (f) and (g) components were determined to be L phase precipitates seen from the side. The two precipitates in loading (i) that gave the signal in (j) were determined to be the β'' phase, which is the peak hardness phase of the Al-Mg-Si system.

Figure 4.12 and 4.13 display the phase maps for the **20-48** and **0-48** conditions, respectively. Similarly to Figure 4.11, the relevant components from NMF decomposition were found. For both the **20-48** sample and Sample 2 from **0-48**, the procured factors were identical to Figure 4.11(b), (d), (f) and (h). However, Figure 4.11(b) and (d) are not unique patterns, since they are 90° rotations of each other. Same with Figure 4.11(f) and (h). Therefore, for the phase maps in Figure 4.12 and 4.13, the factors (b) and (d) were coloured red, and the factors (f) and (h) were coloured turquoise. The precipitates in the NMF loadings that emitted the red signals were coloured red in the real space image, and the precipitates that emitted the blue signals were coloured turquoise. Although it appears that there are two different precipitate phases in these phase maps, they were determined to be the L phase, but with different orientations.
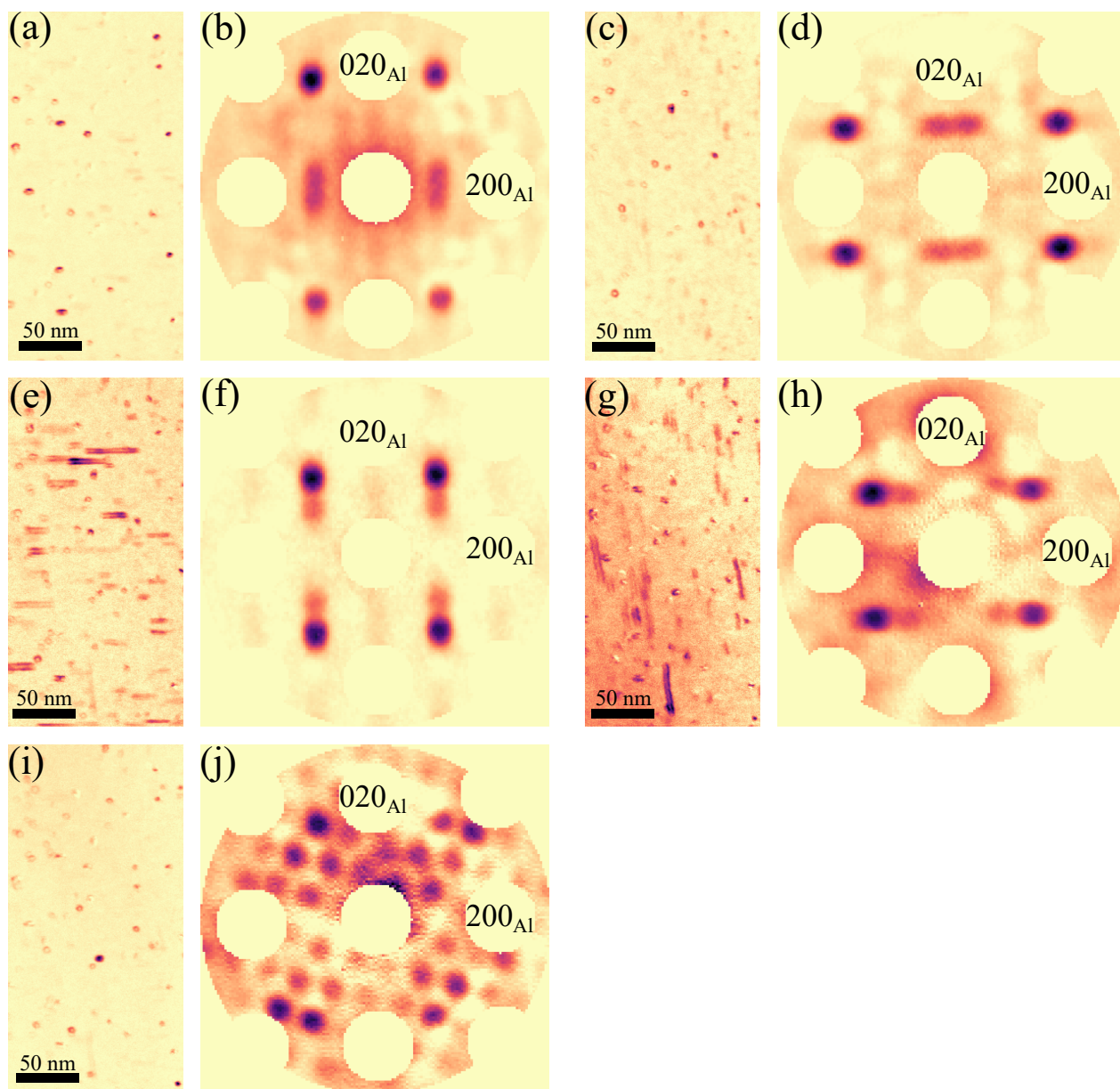
Figure 4.11: Loading and factor maps for Sample 1 of the **0-48** condition. Loadings in (a), (c), (e), (g), (i). Factors in (b), (d), (f), (h), (j). The Al reflections were masked out before NMF decomposition and the contrast has been inverted.
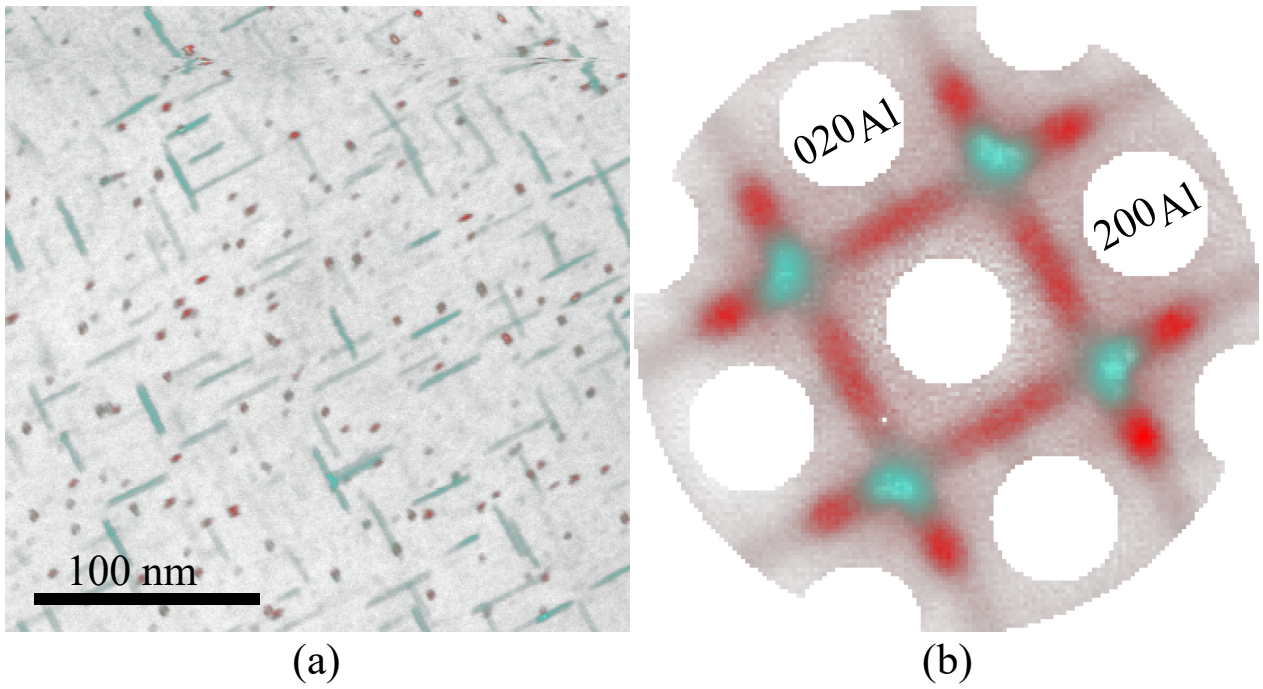
Figure 4.12: Phase map for condition **20-48**. (a) shows a combined coloured loading map in real space. (b) shows a combined coloured factor map in reciprocal space. The Al reflections were masked out before NMF decomposition. The turquoise precipitates in real space give the turquoise signal in reciprocal space. The red precipitates in real space give the red signal in reciprocal space.
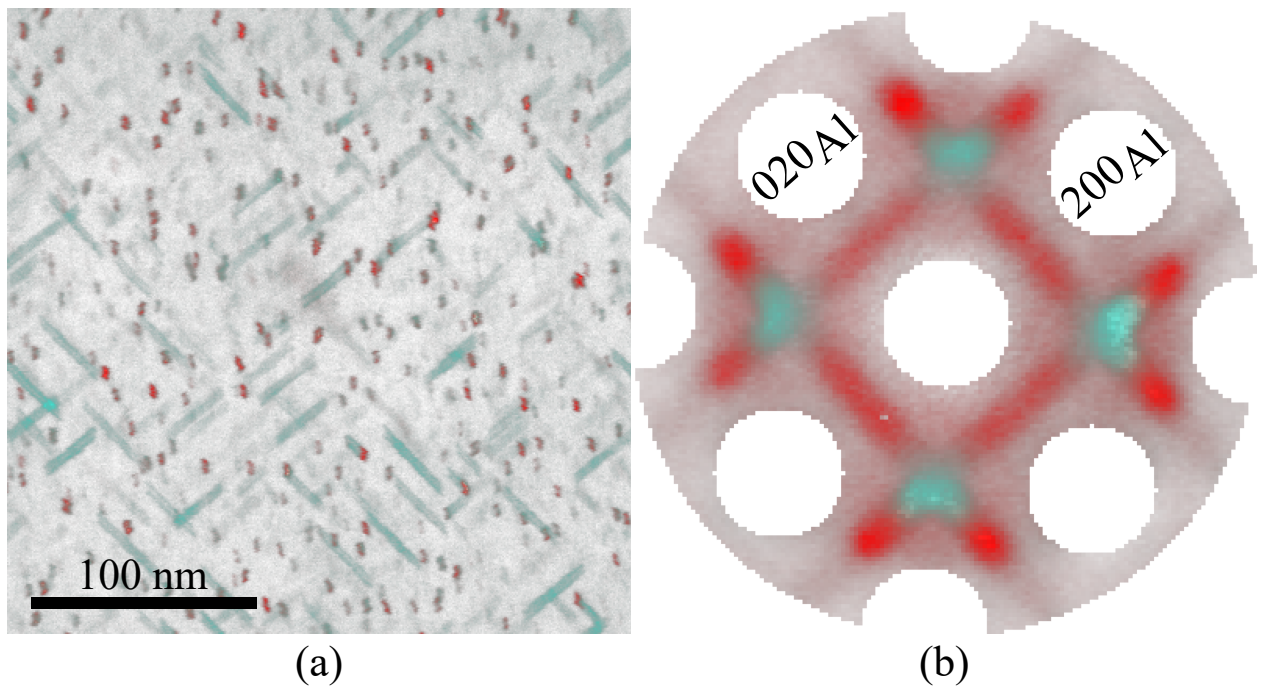
Figure 4.13: Phase map for Sample 2 of the **0-48** condition. (a) shows a combined coloured loading map in real space. (b) shows a combined coloured factor map reciprocal space. The Al reflections were masked out before NMF decomposition. The turquoise precipitates in real space give the turquoise signal in reciprocal space. The red precipitates in real space give the red signal in reciprocal space.

4.6 Strain Mapping With SPED

The strain maps obtained for Sample 1 from the **0-48** condition and for the **20-48** condition are presented in Figure 4.14 and 4.15, respectively. The strain map for Sample 2 from the **0-48** condition can be found in Appendix A.2. The strain maps consist of the three strain components: ε_{xx}, ε_{yy} and ε_{xy}. As mentioned previously ε_{xx} and ε_{yy} are the normal strains, and ε_{xy} is the shear strain given as a fraction of change in the distance between the Al reflections. The two β'' precipitates found in Sample 1 using NMF decomposition are enlarged for all of the strain components in Figure 4.14. A region of interest for all of the strain components in Figure 4.15 with L phase precipitates has been enlarged. Comparing Figures 4.14 and 4.15, one can see that the strain field components around the unique precipitates types are different. For the β'' precipitates, the strain field components take on the shape of a "butterfly" pattern with a pair of blue wings on opposing sides of the precipitates, and/or red wings perpendicular to the blue. For the **20-48** condition, the L phase precipitates do not have this butterfly pattern surrounding them. The strain field in the precipitates is either coloured red or blue, while the surrounding strain field has weaker shades of both red and blue.
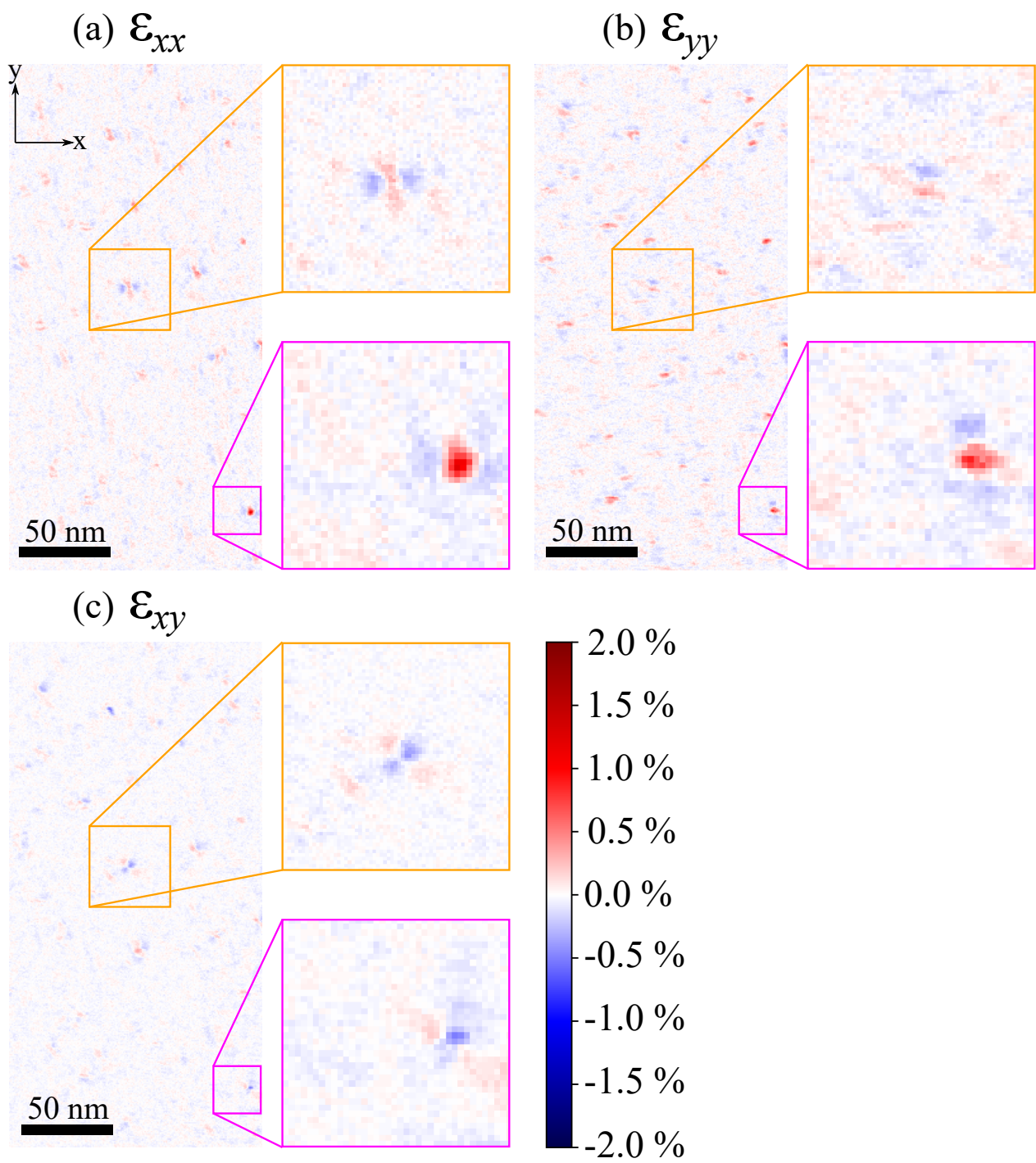
Figure 4.14: Strain map for Sample 1 from the **0-48** condition. The colour bar and the x- and y-axis in (a) applies to all three strain components.
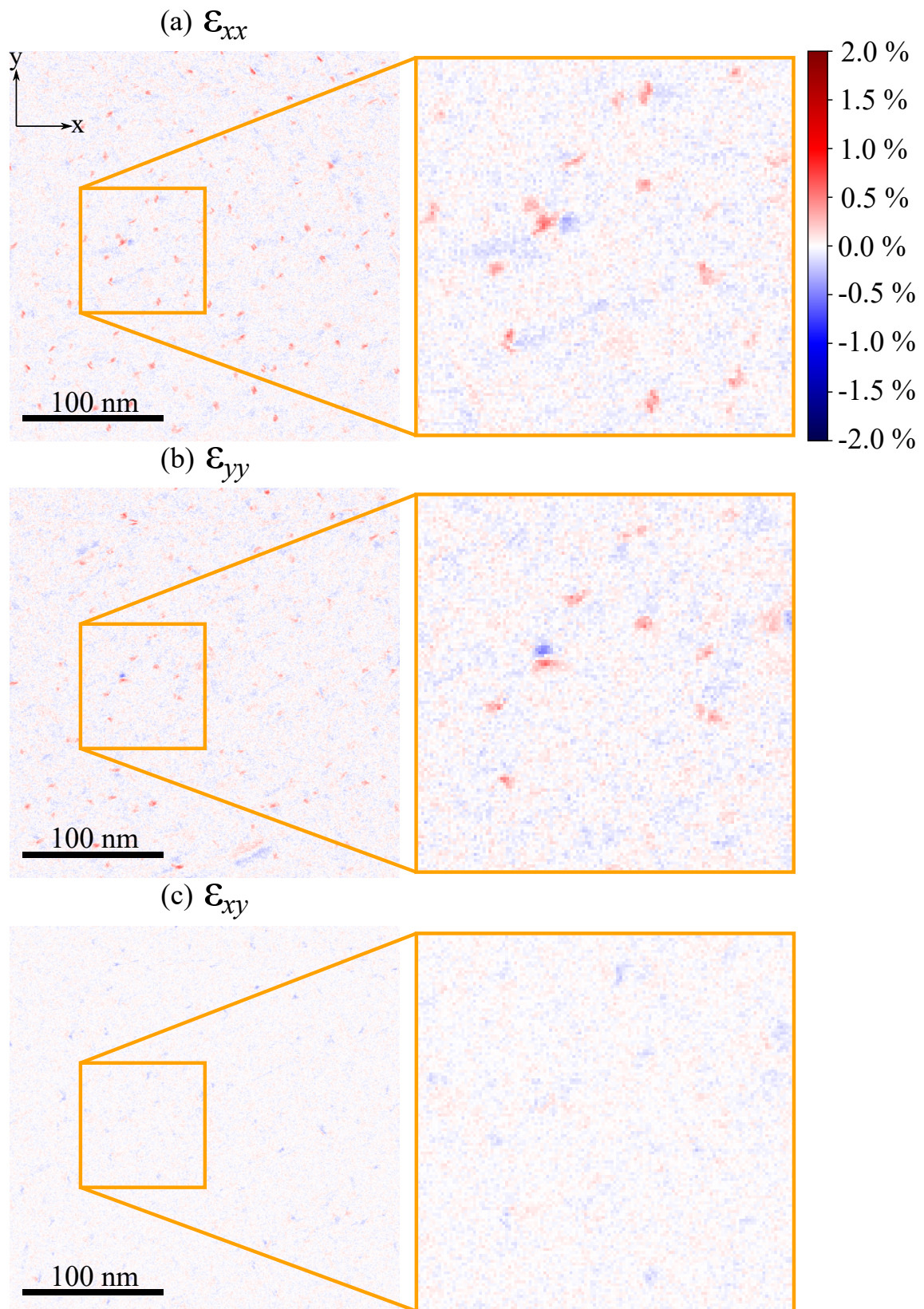
Figure 4.15: Strain map for condition **20-48**. The colour bar and the x- and y-axis in (a) applies to all three strain components.

5 Discussion

This section starts with a discussion of the results and their significance, which relies on previous studies with similar topics and the theory presented in Chapter 2. This is followed by an evaluation of some of the methods used in this study. Lastly, this section ends with a summary of the discoveries and how these relate to the processing conditions during zipper manufacturing at YKK.

5.1 Alloy Composition

The composition of the alloy was presented in Table 3.1 and is the same alloy that was studied [8, 9, 10, 11]. These studies focused on heavily deformed samples, while this study's main focus lies on non-deformed samples. The EPMA measurements differ from the ICP-OES measurements in Table 3.1, most likely because it was not possible to take into account the Al-Fe-Si particles. This could explain why the measured Si is lower with EPMA than with ICP-OES. Based on YKK's measurements, the Mg/Si ratio is 2.7 and Mg + Si = 1.39 wt.%, while the measurements taken at NTNU gave an Mg/Si ratio of 4.1 and Mg + Si = 1.69 wt.%. An important thing to note is that ICP-OES measures a larger volume compared to EPMA, which is an average of measurements taken from 1 µm areas. EPMA is not able to take into account inhomogeneities in the material, while ICP-OES can if a large enough volume is measured. As seen from Table 3.1, this alloy is a 6xxx alloy with a high Cu content. The addition of Cu has been shown to increase thermal stability and hardness in many Al-Mg-Si alloys [24, 25].

"The negative NA effect" is a phenomenon where an alloy's strength is reduced after resting at RT and placed in an oven for AA. Torsæter et al. used APT studies on Al-Mg-Si alloys without Cu to understand the complex clustering process that occurs during NA [67]. They revealed that the alloys with high cluster number density (as a result of direct pre-ageing) mainly had clusters with Mg/Si ratios close to 1. These clusters often called Cluster (2) were associated with the positive NA effect in alloys with low solute content [67, 68]. Alloys with low cluster number density (as a result of NA) had a significant number of clusters with Mg/Si ratios different from 1 [67]. These clusters often called Cluster (1) were associated with the negative NA effect [67, 68]. Torsæter et al. also studied Al-Mg-Si alloys with Cu using APT to see how Cu affects the clusters formed during NA [69]. It was revealed that the strong decrease in cluster number density was impeded by the addition of Cu. They suggested that this was due to a higher number of nucleation sites surviving during AA. Kim et al. found that the addition of Cu hinders the formation of Cluster (1) associated with the negative effect of NA [68]. In addition, Torsæter et al. found that Cu atoms were incorporated into the NA clusters, stabilizing them and preventing them from dissolving at higher temperatures. These clusters seemed to enhance precipitate formation by lowering the formation barrier, which would reduce the negative effect of NA [69]. By these findings, it is reasonable to assume that the high Cu content in the investigated alloy would suppress the negative NA effect.

5.2 Hardness and Microstructure

5.2.1 Hardness Evolution

Hardness tests are used because they are quick to conduct, the machine is relatively inexpensive, and the small indentations made by the machine are non-destructive. It is also possible to test the tensile strength by elongating the specimen at a constant rate until it is permanently deformed to generate a stress-strain plot. A bend test and a compressive test are other methods to test the material's strength as well [13]. By executing a combination of these different tests, one will get a better overview of how the alloy behaves under an applied load. In this thesis, only the Vickers hardness test was used to test a material's resistance to plastic deformation. Therefore, keep in mind that the discussion on hardness reflects only a part of the alloy's behaviour.

As mentioned previously, the hardness curve in Figure 4.1 shows that with increased AA time the hardness of the sample increases until peak hardness is reached. After peak hardness, the hardness curve for the states without NA drops, suggesting that these two samples were slightly overaged. These results are in agreement with the theory presented in Section 2.2.3. At 160 °C, it took 48 h to reach peak hardness, while at 170 °C peak-age was 10 h for the undeformed sample from the same alloy in [9]. This shows that the AA temperature decides the precipitation kinetics.

One can see from Figure 4.1 that before the 6 h AA mark, the NA20h, NA120h, and NA744h samples have a higher hardness than the NA0h samples. At the 6 h AA mark and after, the NA20h, NA120h, and NA744h samples have a lower hardness than the NA0h samples. The NA0.5h samples, however, have a lower hardness compared to the NA0h samples up until the 48 h AA mark. At peak-age, the NA0.5h point lies above the NA0h point with a hardness difference of 3.2 HV ($+2.7\%$). The alloy is a dense alloy since Mg + Si > 1 wt.% (see Section 5.1), and previous studies have found that reduced strength after NA+AA occurs in dense alloys [21, 70]. The results at the 6 h AA and 48 h AA mark seem to be affected by the negative NA effect, except for the NA0.5h sample at peak-age. It may be that a short NA time of 30 min is not enough to affect the strength of the material at peak-age. For AA times under 6 h, there seems to be a positive NA effect. The cause for this might be that a greater amount of Cluster (2) formed during NA than Cluster (1) for these samples as explained in Section 5.1, or the high Cu content suppressed the negative NA effect as explained in Section 5.1.

Focusing on the states studied with TEM, the hardness measured at the **0-6** and **20-6** conditions were 94.6 HV and 104.4 HV, respectively. This is a 9.8 HV difference ($+9.8\%$ difference). The negative effect of NA is prominent when comparing these two states. This might also be related to the types of clusters formed during NA, where Cluster (1) could have dominated. For the **0-48** and the **20-48** conditions, the hardnesses measured were 114.4 HV and 110.0 HV, respectively. This is a lower difference compared to the underaged states at 4.4 HV ($+3.9\%$). The reduction in hardness due to NA is not as significant for these two peak-aged states. The amount of Cluster (1) formed during NA might be less for the peak-age conditions compared to the underaged conditions.

5.2.2 Precipitate Quantification

To find the correlation between the hardness evolution and the microstructure, precipitate quantification was conducted with TEM on the **0-6**, **0-48**, **20-6** and **20-48** conditions. The quantification results in Table 4.1 can give some insight into the hardness measurements of these four states. By comparing the peak-aged conditions, the average precipitate number density for **0-48** and **20-48** are $70 \times 10^3 \, \mu m^{-3}$ and $60 \times 10^3 \, \mu m^{-3}$, respectively. There is a greater difference between the underaged conditions, since the average density for **0-6** is $70 \times 10^3 \, \mu m^{-3}$ and $49 \times 10^3 \, \mu m^{-3}$ for **20-6**. A previous microstructural study related the negative NA effect to a reduced precipitate number density [71]. This can explain why the states with NA have decreased strength compared to the directly aged conditions.

These results can also be related to the DF-TEM images in Figure 4.3. For the **0-48** and **20-48** conditions, the images in Figure 4.3(a) and (b) were chosen with similar thicknesses of 123 nm and 118 nm to justify visually comparing the precipitate number density per area. This was also the case for the **0-6** and the **20-6** conditions, where the imaged region had thicknesses of 86 nm and 89 nm, respectively. These DF-TEM images are in agreement with the findings in Table 4.1, since the image from the **0-48** condition has a higher density of precipitates compared to the **20-48** condition. Similarly, the DF-image from the **0-6** condition had a higher density than the **20-6** condition.

The differences in the precipitate volume fraction and lengths are unfortunately not possible to see with the naked eye in the DF-TEM images in Figure 4.3. The results in Table 4.1, however, show that when comparing the peak-aged conditions, the VF, $\langle l \rangle$ and $\langle l \rangle_m$ are higher in the condition without NA, compared to the condition with NA. This was also the case for the underaged conditions. As mentioned in Section 2.2.3, the precipitate-dislocation interaction determines the hardness of a material. Therefore, increasing the points of contact between dislocations and precipitates per volume would increase the hardness. Greater precipitate number density would lead to more collisions, as well as longer precipitates. In addition, the VF is a function of length, number density and cross-section area. Therefore, longer and more numerous precipitates lead to a higher VF. It has been previously discovered that increased VF leads to increased hardness [25, 72]. This corresponds well with the hardness measurements of the four conditions in Figure 4.1.

The histograms presented in Figure 4.4 were created to understand the distribution of the measured precipitate lengths for the four conditions. The centers of the histograms match well with their corresponding $\langle l \rangle_m$ in Table 4.1. The histogram for the **0-48** condition ranges from 18 nm to around 50 nm, which has a greater spread compared to the other three conditions. As mentioned in Section 2.2.3, the diffusion rate during NA is slow so the small clusters that form at RT are fewer than in the DA case. The rate at which the clusters dissolve into solutes and move to locate other clusters/solutes to form precipitates could therefore also be slower with NA. Since the process is faster with DA due to increased free energy in the system, the probability that the clusters/solutes find each other at random places increases, and could therefore form precipitates with a range of different lengths. In the case of NA, the clusters have lower free energy and might not move around as much, so the probability of generating precipitates with dissimilar lengths could be less. This could also explain why the conditions without NA have longer precipitate lengths than the conditions with NA.

There seem to be several negative effects of NA for this alloy: decreased precipitate length, precipitate number density and therefore decreased volume fraction of precipitates in the alloy. It is still not quite understood why NA leads to a lower precipitate number density, but it was proposed that NA decreases the number of quenched-in vacancies and nucleation sites inhibiting the formation of precipitate phases [67, 71]. Despite the addition of Cu, it is likely a greater number of clusters associated with the negative NA effect similar to those in [67] (Cluster (1)) have formed in the samples with NA. It has also been suggested that long NA times lead to clusters that have little to no structural connection to precipitate phases, which are difficult to dissolve during AA [22, 73]. Since these clusters do not fit into the precipitation sequence, they obstruct GP zone formation [22]. These occurrences result in fewer solute atoms that can be used to nucleate precipitates [73]. This in turn would impede the growth of precipitates in the alloy, both in size and quantity.

5.2.3 Aspect Ratio of Precipitates

By using Fiji, ellipses were fitted to the precipitates' cross-section and their major and minor axes were measured. The normalized heat maps in Figure 4.5 show the calculated aspect ratio plotted as a function of azimuth angle. The peaks of the four heat maps are separated by 90°, and a reasonable explanation for this is the Si-network in the precipitates. The presence of the Si-network is supported by the overlays in Figures 4.8 and 4.9 where it is clearly visible. Assuming that the TEM images were taken along [001] Al direction, the projected Si-network in the precipitate cross-sections could be oriented along [100]Al or [010]Al in C and L phases. The direction along which a precipitate grows is determined by the Si-network's orientation, due to coherency [7]. This means that if the projected Si-network lies along [100]Al, the precipitate's cross-section will be longest along [100]Al [24]. Therefore, precipitates with elliptical cross-sections will lie 90° to each other much like the projected Si-network. This is reflected in the placement of the heat map peaks in Figure 4.5 and the orientation of the lath-shaped precipitates in Figure 4.2.

Even though the thicknesses of the areas imaged in Figure 4.2 are unknown, they are comparable. The microstructure of the peak-aged conditions is different in the sense that there is a greater number of precipitates with elliptical cross-sections in the **20-48** condition compared to the **0-48** condition. The difference is not as prominent in the underaged conditions, but the **20-6** condition has slightly more elongated precipitates. This is in agreement with the heat maps in Figure 4.5, where there is a clear difference between the peak-aged conditions and a smaller difference between the underaged conditions. The **0-6** condition has a larger quantity of precipitates with aspect ratio ~ 1 across all angles, while the **20-48** condition lights up at the peaks of the heat map due to many precipitates with aspect ratio > 1.7. The heat maps for the underaged conditions are similar, except for the **20-6** condition having brighter peaks and therefore a slightly greater number of lath-shaped precipitates, which supports the result from the TEM images in Figure 4.2(c) and (d).

The differences between the conditions with and without NA become more noticeable when studying Figure 4.6. The change in slope for the **20-48** and **20-6** conditions is positive, while the slope in **0-48** is negative and the slope in **0-6** is close to zero. The **20-48** and **20-6** conditions have shorter (see Table 4.1 and Figure 4.4) and more plank-shaped ("flatter") precipitates compared to the **0-48**

and **0-6** conditions. The reason for this is unknown, but a theory can be explained by the side of a precipitate having a greater surface area than the end of the precipitate. The clusters and solutes in the alloy have higher free energy under DA than under NA, because the diffusion rate for NA is lower, in addition to the temperature under DA being higher than RT. The number of collisions is lower during NA and the edge of a precipitate is easier for clusters/solutes to find than the end because of the greater surface area. Since the solutes have greater kinetic energy under DA, the probability that they meet the end of a precipitate is greater than in the NA case, because more collisions occur. When the precipitate grows in size, it might be more likely that the precipitate grows wider during NA because more solutes collide with the edge, while it grows longer without NA. This is however just a hypothesis, but the fact that NA has a slower diffusion rate is visible in Figure 4.1, because the green NA20h curve has a gentle slope for the first three AA times, until it suddenly increases at peak-age. This supports that it takes a longer time to form a larger quantity of precipitates under NA.

In Figure 4.6, most of the precipitates imaged by HAADF-STEM lie within the error bars of the average aspect ratio save for a few exceptions. However, compared to Figure 4.5 one can see that there are several precipitates with a high aspect ratio and Figure 4.6 showcases only the average. It, therefore, makes sense that these exceptions lie above the average. One also has to take into account that larger precipitates are easier to spot in the microscope, and longer precipitates that go through the sample are easier to image with HAADF-STEM since they are not buried in the Al matrix. This contributes to a selection bias, so these precipitates do not necessarily represent the norm.

5.3   Precipitate Crystal Structure

One of the goals of this thesis was to determine the morphology of the precipitates in the alloy, more specifically their phase types. This was done by using three different TEM techniques on the peak-aged conditions: HRTEM, HAADF-STEM and SPED. It is difficult to interpret HRTEM images without the help of CTF simulations, as mentioned in Section 2.3.4. However, it is possible to see if there is order or disorder in a precipitate based on the contrast. The precipitates in Figure 4.7(a) and (c) appear disordered, which points to them being the L phase. This is supported by their FFTs in (b) and (d) which have a significant amount of noise around the (000) reflection. This noise consists of several spots in random places because disordered precipitate crystal structures have no long-range order. Some order is visible in the FFT due to the projected Si-network in the precipitate, which gives a hexagonal pattern marked with yellow dashed lines in Figure 4.7(b) and (d). There also seem to be some spots ordering themselves in a diffused straight line on both sides of the central beam.

The FFTs of the HAADF-STEM images in Figures 4.8 and 4.9 appear similar to the FFTs of the HRTEM images, though some have a 90° orientation difference. This is due to the precipitates having different orientations in the Al matrix, as discussed in Section 5.2.3. For an example comparison between the FFTs of HRTEM and HAADF-STEM, see Figure 5.1(a) and (b). The FFTs have the Si-network visible and spots ordering themselves in a diffuse straight line as well, in addition to noise. The projected hexagonal Si-network emerges in the overlays of Figures 4.8 and 4.9 by joined red triangles along the growth direction. Between the Si columns, the atomic columns have arranged themselves

with no periodicity which implies that it is the L phase. By comparing most of the HAADF-STEM images, HRTEM images and their FFTs to similar results in [8, 9, 28, 46], the precipitates were confirmed to be the L phase.

To check if there were any hints of unique types of precipitate phases in the three SPED datasets, the maximum intensity throughout the stack was computed after the alignment of the central beam. This was done because the maximum reveals the reflection of all phases present in the dataset, despite how seldom the phases appear. The results in Figure 4.10(a) and (c) appear identical, just with different rotations of the Al lattice, which implies that the same precipitate phases can be found in the **20-48** and **0-48** conditions. Figure 4.10(b) comes from Sample 1 in the **0-48** condition and has the same pattern as (a) and (c), but with extra spots in several places. This indicates that there are one or more precipitate phases in this sample that can not be found in the other two datasets.

After performing NMF decomposition on the three datasets, the unique PED patterns and the loadings maps that illustrate where the DP originated from in real space were extracted from the datasets. The combination of the factors in Figure 4.11(b) and (d) is easily recognized in the maximum plots in Figure 4.10(a) and (c). The factors in Figure 4.11(f) and (h) are however not visible in Figure 4.10(a) and (c). The explanation for this could be that their intensity signal was too weak compared to factors (b) and (d). Even though the results in Figure 4.11 is from Sample 1 of the **0-48** condition, which corresponds to Figure 4.10(b), these factors were found in the other two datasets as well (see the DPs in Figures 4.12 and 4.13). This makes it possible to compare the Sample 1 results to Figure 4.10(a) and (c). The component shown in Figure 4.11(j) is unlike the other components, and does not appear in Figures 4.12 and 4.13. It is therefore reasonable to assume that this component accounts for the extra spots in Figure 4.10(b). Unfortunately, it is not possible to recognize this component directly in the maximum plot, but that is most likely a consequence of the reduced quality of the Sample 1 dataset.

To determine which type of precipitate phase the NMF components correspond to, the loading maps were studied and the factor maps were compared to previous literature. The factor maps in Figure 4.11(b) and (d) are similar to the SPED component patterns presented in [9, 46, 74] where this phase was characterized as the L phase. Based on this, the precipitates that emitted this signal in Figure 4.11(a) and (c) were determined to be the L phase. Since the same DP was found in Figures 4.12(b) and 4.13(b), the red-coloured precipitates were characterized as the L phase as well. The factor maps in Figure 4.11(f) and (h) were slightly more challenging to discern since they appear similar to the SPED component patterns of the C phase shown in [8, 9]. From the coloured loading maps in Figures 4.12(a) and 4.13(a), one can see that the turquoise precipitates which emit the (f) and (h) components are lying along the [100] and [010] Al directions and seen from the side. This differs from the SPED component patterns in [8, 9] because these signals came from cross-sections of the C phase. Therefore the factor maps in Figure 4.11(f) and (h) most likely correspond to L phase precipitates but seen from the side. As mentioned in Section 2.2.4, Torsæter et al. proposed that the L phase is a disordered version of the C phase [29], so if the L phase precipitates have fragments of the C phase in them, that would explain why the components of the L phase with a different orientation appears similar to components of the C phase.

As mentioned previously, since the L phase is disordered, a method to identify it is by the presence of the projected Si-network. This network is visible in the NMF components in Figure 4.11(b), (d), (f) and (h), which supports the theory that they correspond to the L phase. In addition, the factor maps in (b) and (d) have similar traits with the FFTs of the precipitate cross-sections in Figures 4.7, 4.8 and 4.9. Figure 5.1 illustrates the similarities and differences between the factor maps and the FFTs. The Si-network and the smeared-out straight lines on both sides of the central beam are similar, while the noise around the (000) reflection is not present in SPED. This is because SPED covers a larger area with many precipitates, while HRTEM and HAADF-STEM image individual precipitates. Since the L phase is disordered, each precipitate will have a unique DP. Therefore, the DP of several precipitates combined will have no constructive interference, so the noise around the central beam from individual precipitates will not be visible in SPED. Despite this, the similarities between the HRTEM and HAADF-STEM images with the factor maps in Figure 4.11(b) and (d), further corroborate that the L phase is present in the **20-48** and the **0-48** conditions.
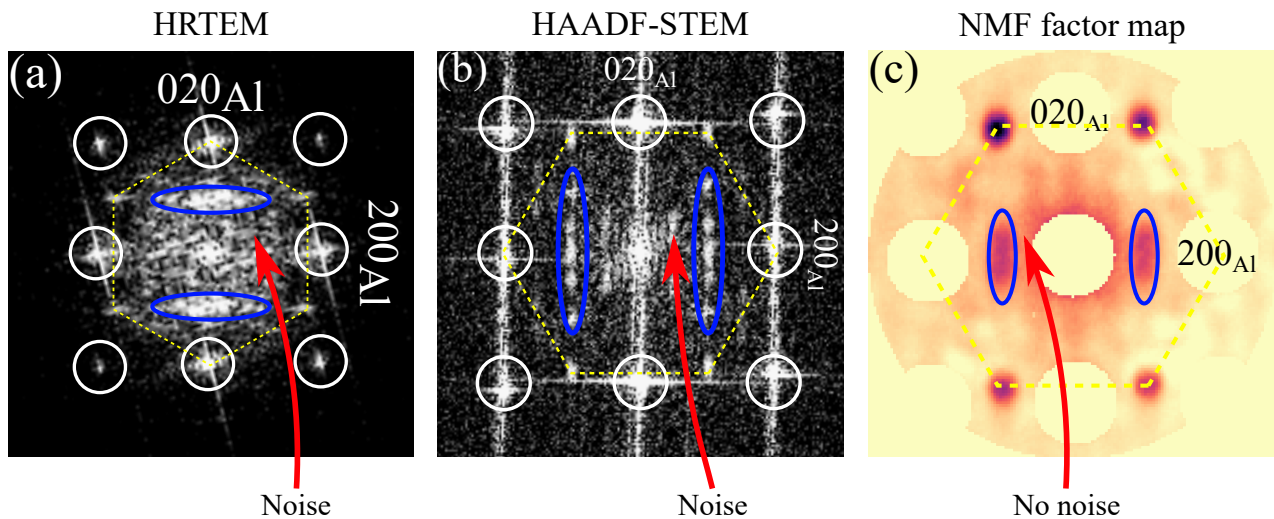
Figure 5.1: (a) FFT of the L phase from a HRTEM image (Figure 4.7(d)). (b) FFT of the L phase from a HAADF-STEM image (Figure 4.9(c)). (c) NMF factor map from L phase precipitates (Figure 4.11(b)). The Si-network is marked with yellow dashed lines. The smeared-out straight lines on both sides of the central beam are marked with blue ellipses. The red arrows point to the area around the (000) reflection.

To determine which precipitate phase the factor map in Figure 4.11(j) corresponds to, the component was compared to previous studies done by Sunde et al. [46, 74]. The component is similar to the NMF components for the β'' phase in these papers, but with a different orientation. Previous master student Øyvind Paulsen presented simulated kinematic DPs in the [001] Al direction for the four possible β'' orientations [37]. Figure 4.11(j) and the DP for β'' oriented along the [230] Al direction are alike, which supports that these precipitates consist of the β'' phase. It is uncertain if the two precipitates that emitted this signal in Figure 4.11(i) are pure β'' or a hybrid since they were not found with HRTEM and HAADF-STEM. However, their factor map in (j) does not show signs of any other phase present, which makes it plausible that these precipitates are pure. Since there were only two β'' precipitates found by SPED and none were found by HRTEM and HAADF-STEM, it indicates that

the volume fraction of β'' in the **0-48** condition is low. This can be explained by the presence of Cu in the alloy, as Cu is known to reduce the presence of the β'' phase [24, 25]. Thronsen et al.'s study on the same but deformed alloy did not identify any β'' phase [9], but we have shown here that it is possible to form the phase in Al-Mg-Si alloys with up to 1.27 wt.% Cu in undeformed conditions.

5.4 Strain Maps

As mentioned in Section 2.2.4, the β'' phase has the shape of a needle, which has a more equiaxed cross-section than the lath-shaped L phase. The ε_{yy} and ε_{xy} strain field components in Figure 4.14(b) and (c) are consistent with the results found by Douin et al. for rod-shaped precipitates [75]. Their experimental strain results also ranged between $2\,\%$ and $-2\,\%$, in addition to having similar butterfly patterns. The article mentions that "the ε_{xx} component is equivalent to ε_{yy} through a 90° rotation", which appears to be the case in Figure 4.14(a) and (b). Furthermore, experimental strain measurements have been done on the β'' phase specifically in [32, 76], and measured with density functional theory (DFT) in [77]. These studies show the butterfly pattern as well, which agrees with the results presented in Figure 4.14. Ninive et al. explain that the strain is caused by precipitate pressing the Al atoms outwards because the precipitate has a larger average interatomic spacing compared to Al, also known as a positive lattice misfit [77]. The butterfly pattern appears in the shear strain ε_{xy} for all coherent, near rod-shaped precipitates but it is particularly clear for β'' because of the four sharp edges of the β'' cross-section. These edges are difficult for the Al matrix to adjust to, resulting in increased strain. These strain results support the conclusion from phase mapping where two precipitates emitted β'' signals.

L phase precipitates have a larger unit cell than Al, similar to β'', which presses the Al atoms outwards generating strain. For the L phase precipitates in Figure 4.15, the ε_{xy} and ε_{yy} strain fields are clearly visible in the precipitates due to the strong red colour. The strain field surrounding them however is not as prominent because there is no distinct shape. This makes it challenging to compare with the results for lath-shaped precipitates in [75]. They found that the ε_{xx} strain has a butterfly pattern, and the ε_{yy} and ε_{xy} have a wing pattern but with a different structure than the butterfly. Those patterns are not visible for any strain components in Figure 4.15. An explanation for this can be that the L phase is semi-coherent while the β'' is fully coherent with the Al matrix. As stated previously in Section 2.2.5, fully coherent phases induce a higher lattice strain on the host matrix compared to semi-coherent phases, because the one-to-one matching of lattice planes requires higher atomic displacements. In addition, the L phase does not have sharp edges like β'' does, so the Al atoms are not displaced to the same extent as with β''. The combination of precipitate shape and coherency could be why the strain around the two β'' precipitates is higher in magnitude and easier to see than around the L phase precipitates.

The presence of β'', which is the peak hardness phase in the Al-Mg-Si system, in the **0-48** condition could explain why the hardness is higher compared to the **20-48** condition. Coherent boundaries are considered more effective at stopping dislocation motion than non-coherent boundaries, as stated in Section 2.2.5, so a sample with β'' precipitates might have greater strength. However, it is worth mentioning that rod-shaped precipitates have a higher strain around them compared to lath-shaped

precipitates regardless of phase type [75]. The **0-48** condition has a greater quantity of precipitates with near-circular cross-section than the **20-48** condition according to Figure 4.5. This would also explain why the hardness is higher for the **0-48** condition. This explanation is more plausible than the hardness increasing due to the presence of β'' precipitates, since only two of them were found throughout this study while several rod-shaped precipitates were identified.

5.5 Evaluation of Methods

5.5.1 Automatic Precipitate Measurements

The main advantage of using Fiji or any software for automatic precipitate measurements is speed since it can measure several precipitates at once, which saves time. Measuring many precipitates also increases the sample size for statistics. However, automated measurements do not come without sources of error. The first is that the BF-TEM images taken for cross-section area measurements most likely did not have high enough magnification. These BF images should generally include ten to thirty precipitates each to make it easier to measure the cross-section manually [52]. The BF-images utilized in this study to measure cross-section area had 100-200 precipitates in each. Therefore, precipitates with small cross-section areas could have been missed, which would mean that the calculated $\langle CS \rangle$ is larger than it should be. In addition, using thresholding in Fiji often gave measurements of single pixels that did not belong to a precipitate. It was therefore necessary to decide on a minimum measured area of $1\,\mathrm{nm}^2$ to filter out noise from these single pixels. Precipitates with a cross-section area less than $1\,\mathrm{nm}^2$ were not included in the automated measurements. These factors together result in a VF that is greater than it should be, since it is directly proportional to $\langle CS \rangle$. All four conditions that were studied with TEM were measured in the same way, which implies that their VF and $\langle CS \rangle$ are higher. If they are overestimated in all the TEM conditions, the measurements are still relatively correct when compared to each other.

The second source of error in using automatic procedures is that choosing the threshold value is subjective. Different people would generate different results because they might choose different threshold values in Fiji which will affect the result. This error was estimated by choosing three thresholds for an image: the lowest acceptable threshold, the highest acceptable threshold, and lastly an appropriate threshold in between. What is defined as "acceptable" varies from person to person, which would also generate errors. A possible way to counteract this is to try more than three thresholds to reduce the standard error or to take images with higher magnification and measure the precipitates manually. Note that the maximum relative error of $\langle CS \rangle$ was 4.3 % when using the three thresholds method which is within an acceptable range, so one can consider if there is a need to reduce this error.

To get a better evaluation of the automated procedure with Fiji, this method was compared to the manual procedure by measuring ten precipitates imaged by HAADF-STEM, five from each peak-aged condition, using both methods. The precipitates measured manually are represented as orange dots in Figure 4.6, and the comparison between the two methods is found in Table 4.2. The method of using three different thresholds was not used because the precipitates were overlaid with a manually defined mask to define the position of the interface to make thresholding simpler in Fiji. The difference

in the aspect ratio when comparing these two methods in Table 4.2 does not seem large. Three of them happen to have identical aspect ratios. The significant difference lies in the cross-section area measurements. Measuring manually generally results in larger cross-section areas than when measuring automatically with Fiji. There can be several reasons for this. The first is the assumption that the precipitates have rectangular cross-sections which leads to an increased cross-section area if the precipitates have rounded edges. If the precipitates have a circular cross-section, this error can be corrected by multiplying the cross-section area with $\pi/4$, which is the area of an ellipse divided by the area of a rectangle. The second source of error is caused by drift when implementing HAADF-STEM to image precipitates. Drift leads to the images becoming skewed so the Al columns in the bulk are not perpendicular to each other. This skewness was not corrected before measuring in Fiji, because the resolution of the image would become unknown and setting the scale for the image would not be possible. When measuring manually, atomic columns were counted so the measured major and minor axes were perpendicular to each other. However, the skewness of the lattice in the HAADF-STEM image would result in Fiji measuring major and minor axes that are not truly perpendicular to each other. This would affect the result of the cross-section area, but it is difficult to say if Fiji would measure a too high or too low value since it depends on the degree of skewness.

5.5.2 CBED for Measuring Thickness

When acquiring CBED images, one has to tilt off zone and take care not to stray away from the area that the BF and DF images were taken from. Otherwise, the thickness measurement would be taken at the wrong region and give a wrong answer. To counteract this source of error, the tilting was done in image mode, though it was still challenging to stay put. However, as long as one stays within the region the image was taken, it does not make much of a difference if the thickness was measured at the center of the image or near the edge. This is based on the assumption that the thickness does not vary greatly from the center to the edge of the imaged area.

As mentioned in Section 3.6.1, the code that PhD student Christoph Hell wrote used equations (2.39) and (2.43) to calculate the thickness based on the fringe spacings measured in the CBED image. An example of the output from the code is given in Figure 5.2. As seen from the figure, there are three different options to choose from based on which iterator n_k from equation (2.43) is used. Choosing the wrong iterator n_k means choosing the incorrect thickness, which gives consequences for the volume calculation and further for the precipitate volume fraction. To help with this, research scientist Ruben Bjørge at SINTEF simulated the two-beam condition for the (200) and (220) cases in Al [78]. The extinction distance ξ is equal to the thickness when the first intensity minimum in the diffracted beam appears for $\mathbf{s} = 0$. The extinction distances for aluminium at $200\,\text{kV}$ for the (220) and (200) cases are $\sim146\,\text{nm}$ and $\sim85\,\text{nm}$, respectively, which is observed in the simulations. To help choose the correct iterator these values were used in addition to the R^2 value in Figure 5.2. The closer the R^2 value is to one, the better the linear fit is. For Figure 5.2, the center image for $n_k = 2$ has the highest R^2 value and the extinction distance is the value closest to $85\,\text{nm}$. Thus, the thickness was determined to be $94.7\,\text{nm}$ for this case.
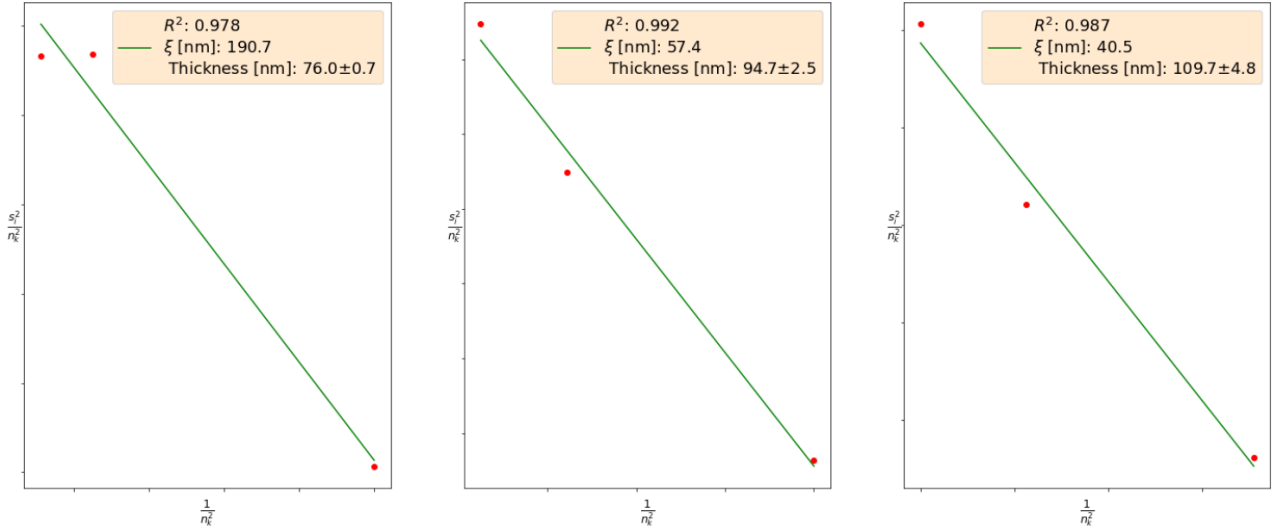
Figure 5.2: The output from PhD student Christoph Hell's Python script used to determine the thickness of an area in the **20-6** sample. The CBED image was taken along the 200 Kikuchi band in this case.

PhD student Christoph Hell and Dr. Sigurd Wenner tested the reliability of the Python script [79]. Wenner acquired CBED images from a conical sample with known thickness and Hell utilized the script to measure the thickness. What they found was that for thicknesses close to the extinction distance, the script generated the wrong result, but the reason for this is still unknown [79]. This means that if the thicknesses of the samples were close to $\sim$146 nm or $\sim$85 nm depending on which Kikuchi band was chosen, the script would have trouble. In this thesis, the electropolished samples were unfortunately quite thick so this problem came up often and choosing the correct iterator was challenging. Therefore, in uncertain cases, a second check was utilized to see if the correct iterator was chosen, by comparing the measured fringe spacings with the CBED pattern generated by Ruben Bjørge's simulations. Electropolished Al samples are usually under 100 nm thick, so it is recommended to tilt to the (220) Kikuchi band since the extinction distance 146 nm > 100 nm. The (200) Kikuchi band is not recommended due to the risk that the thickness is close to 85 nm.

The importance of the thickness for the precipitate quantification results can be discussed by using Figure 5.2 as an example. The choice of the wrong iterator n_k could result in a thickness that is either too high or too low. Assume that 76.0 nm ($n_k = 1$) was chosen in Figure 5.2 instead of 94.7 nm ($n_k = 2$). A thinner thickness would result in a volume decrease, which in turn would give an increased precipitate number density (from 53×10^3 µm^{-3} to 64×10^3 µm^{-3} in this case). Since the volume fraction is directly proportional to the precipitate number density, the volume fraction would also increase (from 0.48 % to 0.5 % in this example). One can see that getting the thickness slightly wrong does not affect the volume fraction greatly as 0.5 % lies within the margin of error ($\pm$ 0.04 %). This is because the thickness was changed for one out of six thickness measurements and since the volume fraction is calculated from the averaged values of precipitate number density, length and cross-section area, it has little impact. In addition, the precipitate number density does not solely depend on the thickness, it depends on other parameters as well. However, if the wrong iterator was chosen for all six measurements, the volume fraction would most likely be wrong and lie outside the

margin of error. Given that one utilizes the extinction distance, the R^2 value and the simulations to choose the correct iterator and thickness, CBED can be a reliable method to determine the thickness of the imaged area. EELS is an easy alternative, but it requires an expensive spectrometer, while the advantage of CBED is that it can be done on any TEM.

5.5.3 AutomAl 6000 for the L Phase

It is evident from the results in Section 4.4 that there are mistakes in the overlays presented. The most noticeable mistake from AutomaAl 6000 is the replacement of a few Si-network atoms with Al in the overlays. Furthermore, Figure 4.9(e) has a few more Al columns overlaid than expected in a precipitate. Errors similar to this can easily occur if the quality of the HAADF-STEM images has been affected by drift or contamination. Atomic columns that should be separate could easily merge in the image and be interpreted as one column by the software. It is also impossible to separate Al, Si and Mg based on the contrast with the naked eye since their atomic numbers Z are close to each other. Only the heaviest element Cu (with the atomic number $Z = 29$) is possible to distinguish from the others since Cu columns are brighter. AutomAl 6000 first uses the rules explained in Section 2.2.6 to determine the atomic columns, and second puts a slight weight on intensity where Mg, Al and Si have somewhat increasing intensities [65]. However, this method is not foolproof since contamination could affect the contrast in the image. The four precipitates in Figures 4.8 and 4.9 were overlaid because the goal was to identify the local atomic arrangements. The disorder of the L phase is apparent in these precipitates, despite the errors from AutomAl 6000. This leads to the conclusion that AutomAl 6000 is reliable for identifying the L phase. However, if one wanted to calculate the fraction of the different atomic columns in the L phase precipitates, AutomAl 6000 would generate an incorrect result due to the previously mentioned errors. Therefore, perfect images are recommended but challenging to obtain if fraction calculation with AutomAl 6000 is required.

5.5.4 SPED for Measuring Strain

Figure 5.3 shows a BF-TEM image where the SPED scan area for the **20-48** dataset is marked by green dashed lines. Figure 5.3 supports the results in Figure 4.2: that several precipitates in the **20-48** condition have an elliptical cross-section. By looking closely, the green dashed lines in Figure 5.3 do not form a perfect square while the SPED dataset is assumed to be a perfect square: (400 x 400) pixels. This scan distortion can be caused by specimen drift due to the long acquisition time of SPED scans (2 h in this case). In virtual images, the distortion affects the angles between objects and consequently the shape of the strain fields in the strain maps. This means that the butterfly patterns could be stretched out in one direction or be oriented at a different angle than they should. Similar issues were discussed in [80]. It might be possible to correct the distortions during post-processing by comparing to the BF image or using prior knowledge that precipitates seen from the side are 90° to each other, but such changes are not trivial with SPED and would require much work. It is unfortunately not possible to avoid drift, but for this study, the distortion does not have a significant effect. The first reason is that the scan area is close to a perfect square, so the distortion is not as prominent. The second reason is that the goal of the strain mapping was to identify any difference in strain between

the L phase and the β'' phase. Therefore, deviations from exact measurements are less significant.

Another source of error to consider is the fact that these 2D strain maps are a projection of 3D strain fields. The strain in the z-direction was also not taken into account in [32, 75, 76]. This was done based on the assumption that the lattice strain is uniform throughout the sample, or that the ε_{zz} component is negligible compared to the other components. Unfortunately, this entails that one cannot get the whole picture and should interpret the strain maps with this in mind. For example, the precipitates with weaker strain field signals are most likely precipitates that are buried in the Al matrix. Meanwhile, precipitates that extend through the entire specimen would probably have a stronger strain field signal.
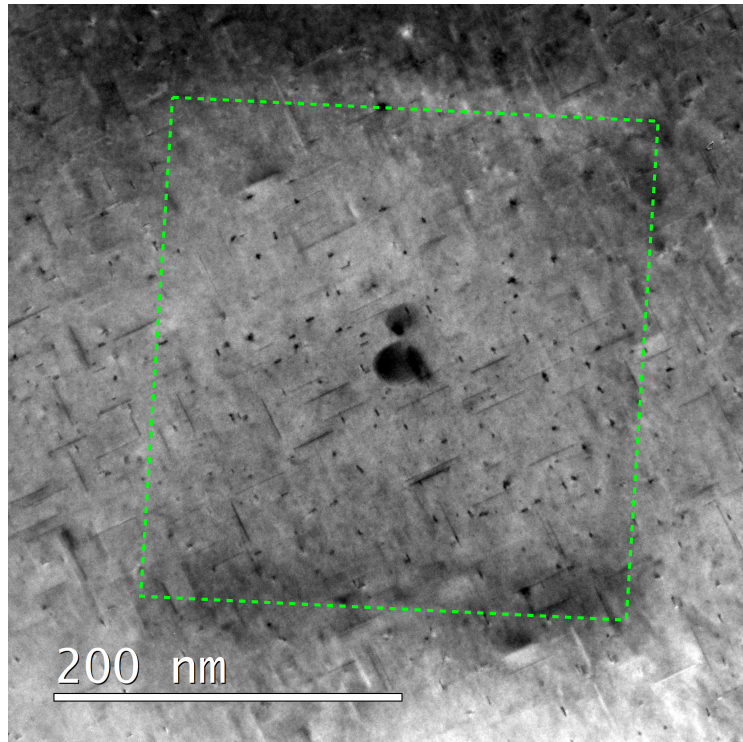
Figure 5.3: A BF-TEM image showing the SPED scan area for the **20-48** dataset. The green dashed lines mark approximately where the scan was acquired. The black dots in the middle are hydrocarbon contamination produced from a stationary electron beam.

5.5.5 Comparing TEM Techniques for Phase Identification

Three techniques were implemented for identifying phases in this thesis: HRTEM, HAADF-STEM and SPED. An advantage of HRTEM is the ability to acquire several images of precipitates in a short amount of time. These real space images are challenging to interpret due to the CTF not monotonously decreasing or increasing (as opposed to HAADF-STEM) with spatial frequency, and simulations are required to understand the atomic structure. Even so, the FFTs of these images generate the same results as the FFTs of the HAADF-STEM images and the NMF components. The FFTs from HRTEM had slightly more noise, but it was still possible to interpret them and compare them to literature. Moreover, one can simulate the DPs of different precipitate phases to compare, although the L phase

is difficult to simulate due to the disorder.

HAADF-STEM is the technique with the highest resolution and has Z-contrast, as well as the CTF monotonously decreasing or increasing with spatial frequency. This is the main advantage of this technique because it is possible to determine the atomic columns in the precipitate. Furthermore, the FFTs of HAADF-STEM images were easier to comprehend, since they had less noise than the FFTs of HRTEM images. If the goal is to study the atomic structure of precipitates, HAADF-STEM is recommended. The disadvantage of HAADF-STEM is that it takes a long time to acquire several images of precipitates, so this technique is not recommended for precipitate statistics. Beam contamination is another problem with HAADF-STEM, which affects the quality of the images. Drift affects all three techniques but in different ways. HRTEM images become blurry, HAADF-STEM images become skewed and SPED scans become distorted with drift.

If the goal is to study over a hundred precipitates, SPED is the most effective technique. For these samples, a SPED scan took 2 h given that the quality was acceptable. SPED's main advantage is the ability to cover a larger area and gives a great deal of interesting information, but the disadvantage is the post-processing of datasets which is challenging and requires time. It is also not trivial to determine the thickness of a scan area if the goal is precipitate statistics using SPED, especially if the scan area is large where inhomogeneities are expected. The components from NMF decomposition had similar DPs to the HRTEM and HAADF-STEM FFTs, and it was possible to identify them by comparing them to literature. Therefore, it is reasonable to conclude that SPED is a reliable method for phase identification as well.

Another TEM technique not utilized in this thesis to identify phases is BF-TEM imaging. Examples of studies using this technique are [24, 28, 37]. These studies compared the shape of the precipitate cross-sections to literature to determine which phases their alloys had. This technique is recommended if the precipitate phases are ordered and/or easy to recognize. The BF-images similar to the ones in Figure 4.2 were not easy to interpret which is why HRTEM, HAADF-STEM and SPED were used.

5.5.6 Selection Bias

Selection bias is a source of error that arises in all TEM studies. Al TEM samples are usually thin 3 mm in diameter discs made from a larger sample, so eventual inhomogeneity throughout the material is not taken into account. Additionally, the volume studied with TEM is even smaller than the total volume of the sample. For the **20-48** condition, 6 sets of DF images were taken at 426.69 nm x 426.69 nm areas with thicknesses close to 100 nm giving a volume of approximately $0.109\,\mu m^3$. Multiplying with $0.75\,\%$ which is the volume fraction of precipitates for this condition (see Table 4.1) gives $8.2 \times 10^{-4}\,\mu m^3$. Imagine if the Al alloy sample had the same dimensions as a sugar cube, which has a volume of approximately $1\,cm^3 = 1 \times 10^{12}\,\mu m^3$. Multiplying this with the same volume fraction gives a precipitate volume of $7.5 \times 10^9\,\mu m^3$. The cube has a precipitate volume that is 10^{15} orders larger than the precipitate volume studied in the TEM, which puts into perspective how small the volume studied with TEM is. Choosing an area to image in the TEM is affected by selection bias as well. Generally, usable images require thin and flat areas because it is impractical to tilt the specimen often. The specimen consists of several grains with different orientations, so there are

probably inhomogeneous areas in the specimen as well. Therefore, the collected precipitate statistics and the TEM images only describe a small area of the sample and the variations throughout the sample are unknown.

5.6 Summary

Undeformed samples of an Al-Cu-Mg-Si alloy from YKK were studied in this thesis by hardness tests and varying TEM techniques. It was discovered that NA did not make a significant difference in hardness at peak-age, but NA affected the hardness of the underaged conditions. This was supported by the collected precipitate statistics for the four TEM conditions. It was speculated that the cause of these differences was the high Cu content of the alloy which is said to reduce the negative effect of NA. It might also have been that the peak-age and underaged conditions had different fractions of Cluster (1) and Cluster (2) formed during NA. This study also found that when a precipitate grows large, its cross-section shape was most likely to be elliptical with NA and circular without NA. This could also explain the difference in hardness because the strain around rod-shaped precipitates is higher than around lath-shaped precipitates. It is therefore assumed that rod-shaped precipitates are greater obstacles to dislocation motion. For the peak-aged conditions, HRTEM, HAADF-STEM and SPED revealed that NA did not affect the fraction of precipitate phases to a large extent. Only two β'' precipitates were found in the **0-48** and the rest consisted of the L phase. The addition of Cu in Al-Mg-Si alloys is known to reduce the presence of the β'' phase, so a low fraction is expected. The strain maps are in agreement with the results from the phase maps because the precipitates determined to be the β'' phase had a unique strain field pattern that the L phase did not have. This supports the slight difference in hardness between **0-48** and **20-48** as well, since the β'' phase induces a greater strain on the Al matrix compared to the L phase which results in increased strength.

During the production of YKK zippers, the alloys are heavily deformed during milling and forging. This study focused on undeformed samples and is maybe more of academic interest, but can serve as a reference for YKK when they conduct studies on deformed samples in the future. The **0-48** and **0-6** conditions without NA were measured to have a higher hardness than the **20-48** and **20-6** conditions, which shows the negative effect of NA. Unfortunately, NA is unavoidable in the aluminium industry and it is impractical for YKK to implement DA into their procedures. It is however possible to suggest decreasing the NA time for this particular alloy if the goal is to retain strength. On the positive side, the negative effect of NA was not as prominent at peak-age for any of the NA times based on Figure 4.1, with a 3.9 % difference between the **0-48** and **20-48** conditions. This is promising for the production of this alloy as long as YKK continues to anneal the alloy to peak-age, since NA seems to have little effect there. However, the peak-age for deformed samples is only known for 20 h NA and 120 h NA from [8, 9, 10]. Mørkeseth used 18 h NA in her master's thesis for both deformed and undeformed samples but kept the AA time fixed at 5 h, which might not have been peak-age [11]. Therefore, for other NA times, the peak-age for deformed samples is unknown and should be studied if YKK were to decrease the NA time. Another important thing to note is that the conditions with NA in this study were not artificially aged for longer than 48 h, so it is possible that peak-hardness has not been reached yet for these conditions. This limitation was unfortunately caused by a lack of material, but this would have been interesting to check.

6 Conclusion

An investigation of the effect of natural ageing was conducted on undeformed Al-Cu-Mg-Si alloy samples from YKK. The samples underwent a range of heat treatments with and without natural ageing, and their hardness was tested. Different TEM techniques were implemented to study the underlying reason for the differences in hardness. In addition, precipitate morphology and the strain surrounding precipitates were studied. A summary of the results is given as follows:

1. For the four conditions studied by TEM, the **20-6** and **20-48** conditions showed negative effects of natural ageing with decreased strength due to lower volume fraction, precipitate number density and precipitate length. The **0-48** and the **20-48** conditions only had a 3.9 % difference in hardness, suggesting that natural ageing does not have a significant effect on the alloy at peak-age. This is significant for YKK where natural ageing is unavoidable in production.

2. Measuring the aspect ratio of precipitates with Fiji showed that the conditions with natural ageing had more precipitates with elliptical cross-sections than the conditions without natural ageing, which had more circular cross-sections. The lath-shaped precipitates oriented themselves in the $\langle 100 \rangle$ Al direction due to the projected Si-network. As a precipitate grew in size, the likelihood that it had an elliptical cross-section was higher with natural ageing, while it most likely had a near-circular cross-section with direct ageing.

3. Investigations with HRTEM, HAADF-STEM and SPED determined that most of the precipitates were the L phase, but a **0-48** SPED dataset showed two $\beta^{''}$ precipitates after NMF decomposition. This was supported by the butterfly patterns around these precipitates in the strain maps. The low fraction of the $\beta^{''}$ phase was likely caused by the high Cu content in the alloy.

4. HRTEM and SPED were established to be effective methods to identify precipitate phases because one can gather a large sample size in a short amount of time. HAADF-STEM was determined to be better for studying details in the atomic structure. All three techniques generated FFTs and DPs of acceptable quality such that phase identification was possible.

7 Further Work

One method that has been applied in previous studies to differentiate precipitate phases is to take BF-TEM images at high magnification or HRTEM images and compare the cross-section of the precipitates to literature [24, 28, 37]. The L phase is then recognized by a "thin rectangular cross-section elongated in the $\langle 100 \rangle$ Al direction" [24]. By measuring the aspect ratio of precipitates throughout this study and discovering that most of the precipitates in the alloy are the L phase, the idea of using the aspect ratio to identify precipitate phase types came to mind. Further work would be to measure the aspect ratio of varying precipitate phases in other alloys and compare the results to this study on the L phase. The heat maps in Figure 4.5 show that the L phase has varying degrees of ellipticity, so there might not be an aspect ratio fingerprint for the L phase. However, if further work could check if there is an aspect ratio fingerprint for other precipitate types, it could become a useful tool to differentiate between these precipitate types in TEM images.

Secondly, it would be interesting to get to the root of why the aspect ratio of the L phase increases as the cross-section area increases in the condition with NA. This could be done by a systematic study of crystal structure and composition for disordered precipitates with different aspect ratios. AutomAl 6000 might be useful in this case if better images can be acquired (either with thinner, more uniform samples or a different TEM operator). It is also of interest to check if this phenomenon is present in other types of aluminium alloys when subjected to NA.

As mentioned previously, the strain field analysis in this present work is a 2D projection of a 3D strain. This is because the generated PED patterns are 2D projections themselves, which makes it challenging to extract information about the 3D structure from a dataset. Tovey et al. proposed a tomographic model to reconstruct a full 3D strain tensor field from a series of 2D SPED datasets collected in a tilt series for multiple angles [81]. In this study, they demonstrated their model analytically and numerically, but in 2017 a demonstration of tomographic reconstruction was done experimentally on nanowires in [82]. Further work would be to check if this method can be implemented on aluminium alloys to study the 3D strain field around precipitates. It would be interesting to investigate if the assumption that the lattice strain is uniform throughout the sample is correct. If possible, it could be of interest to see how the morphology of precipitates and the strain fields surrounding them change during AA by conducting in situ experiments in the TEM. Strain field analysis on samples with deformation is also intriguing, both the 2D and the 3D case, to see how it differs from the undeformed case.

Lastly, since this work was based on undeformed samples with varying NA and AA times, it can be used as a reference for future studies on this alloy. Thronsen, Erga and Mørkeseth looked at deformed samples naturally aged for $20\,\mathrm{h}$, $120\,\mathrm{h}$ and $18\,\mathrm{h}$ in [8, 10, 11], so the next step could be to study samples with deformation but with $0\,\mathrm{h}$, $30\,\mathrm{min}$, and $144\,\mathrm{h}$. These were the NA times used in this thesis other than $20\,\mathrm{h}$ and $120\,\mathrm{h}$, which makes it possible to compare future results with the present work.

References

[1]   OEC World. *Norway*. Retrieved from `https://oec.world/en/profile/country/nor`. Accessed 09.06.2022.

[2]   T. Geller. *Aluminum: Common Metal, Uncommon Past*. Retrieved from `https://www.scienc ehistory.org/distillations/magazine/aluminum-common-metal-uncommon-past`. 2007.

[3]   F. M. Mazzolani. *Aluminium Alloy Structures*. E & FN spon., 1995.

[4]   J. Hirsch, B. Skrotzki, and G. Gottstein. *Aluminium Alloys: The Physical and Mechanical Properties*. Wiley, 2008.

[5]   I.J. Polmear. "Aluminium Alloys – A Century of Age Hardening". In: *Materials Forum* 28 (Jan. 2004), pp. 1–14.

[6]   B. C. Carter and D. B. Williams. *Transmission Electron Microscopy: A Textbook for Materials Science*. Springer, 2009.

[7]   S. J. Andersen, C. D. Marioara, J. Friis, S. Wenner, and R. Holmestad. "Precipitates in aluminium alloys". In: *Advances in Physics: X* 3.1 (2018), p. 1479984. DOI: `10.1080/23746149.2 018.1479984`.

[8]   E. Thronsen. "The effect of deformation and natural ageing in an Al-Mg-Si-Cu alloy with high Cu-content: A transmission electron microscopy study". MA thesis. NTNU, 2018.

[9]   E. Thronsen, C. Marioara, J. Sunde, K. Minakuchi, T. Katsumi, I. Erga, S. Andersen, J. Friis, K. Marthinsen, K. Matsuda, and R. Holmestad. "The effect of heavy deformation on the precipitation in an Al-1.3Cu-1.0Mg-0.4Si wt.% alloy". In: *Materials & Design* (Sept. 2019). DOI: `10.1016/j.matdes.2019.108203`.

[10]   I. Erga. "The Mechanical Properties During Thermomechanical Treatment of an Al-Cu-Mg-Si alloy Intended for Zippers". MA thesis. NTNU, 2018.

[11]   H. Mørkeseth. "The effect of Fe and Mn on precipitation in an Al-Cu-Mg-Si alloy. A transmission electron microscopy study". MA thesis. NTNU, 2020.

[12]   C. Kittel. *Introduction to Solid State Physics*. Wiley, 2005.

[13]   W. D. Callister and D. G. Rethwisch. *Materials Science and Engineering: An Introduction*. 8th. Wiley, 2009.

[14]   S. Wenner. "Transmission Electron Microscopy and Muon Spin Relaxation Studies of Precipitation in Al-Mg-Si Alloys". PhD thesis. NTNU, 2014.

[15]   J. R. Davis. *Aluminum and Aluminum Alloys*. ASM International, 1993.

[16]   J. E. Hatch. *Aluminum: Properties and Physical Metallurgy*. American Society for Metals, 1998.

[17]   *Ptable*. Retrieved from `https://www.ptable.com/?lang=no`. Accessed 11.04.2022.

[18]   Royal Society of Chemistry. *Periodic Table*. Retrieved from `http://www.rsc.org/periodic-t able`. Accessed 11.04.2022.

[19]   D. S. MacKenzie and G. E. Totten. *Handbook of Aluminum*. Vol. 1: Physical Metallurgy and Processes. Marcell Dekker, Inc., 2003.

[20] D. A. Porter, K. E. Easterling, and M. Y. Sherif. *Phase Transformations in Metals and Alloys.* 3rd. CRC Press, 2009.

[21] J. Royset, T. Stene, J. A. Sæter, and O. Reiso. "The Effect of Intermediate Storage Temperature and Time on the Age Hardening Response of Al-Mg-Si Alloys". In: *Aluminium Alloys 2006 - ICAA10.* Vol. 519. Materials Science Forum. Trans Tech Publications Ltd, July 2006, pp. 239–244. DOI: `10.4028/www.scientific.net/MSF.519-521.239`.

[22] F. A. Martinsen, F. J. H. Ehlers, M. Torsæter, and R. Holmestad. "Reversal of the negative natural aging effect in Al-Mg-Si alloys". In: *Acta Materialia* 60.17 (Oct. 2012), pp. 6091–6101. DOI: `10.1016/j.actamat.2012.07.047`.

[23] P. Osuch, M. Walkowicz, T. Knych, and S. Dymek. "Impact of the Direct Ageing Procedure on the Age Hardening Response of Al-Mg-Si 6101 Alloy". In: *Materials (Basel, Switzerland)* 11 (July 2018), p. 1239. DOI: `10.3390/ma11071239`.

[24] C. D. Marioara, S. J. Andersen, J. Røyset, O. Reiso, S. Gulbrandsen-Dahl, T. Nicolaisen, I. Opheim, J. F. Helgaker, and R. Holmestad. "Improving Thermal Stability in Cu-Containing Al-Mg-Si Alloys by Precipitate Optimization". In: *Metallurgical and Materials Transactions A* 45.7 (June 2014), pp. 2938–2949. DOI: `10.1007/s11661-014-2250-0`.

[25] C. D. Marioara, S. J. Andersen, T. N. Stene, H. Hasting, J. Walmsley, A. T. J. Van Helvoort, and R. Holmestad. "The Effect of Cu on Precipitation in Al–Mg–Si alloys". In: *Philosophical Magazine* 87.23 (2007), pp. 3385–3413. DOI: `10.1080/14786430701287377`.

[26] M.A. van Huis, J.H. Chen, M.H.F. Sluiter, and H.W. Zandbergen. "Phase stability and structural features of matrix-embedded hardening precipitates in Al–Mg–Si alloys in the early stages of evolution". In: *Acta Materialia* 55.6 (2007), pp. 2183–2199. DOI: `https://doi.org/10.1016/j.actamat.2006.11.019`.

[27] J. H. Chen, E. Costan, M. A. van Huis, Q. Xu, and H. W. Zandbergen. "Atomic Pillar-Based Nanoprecipitates Strengthen AlMgSi Alloys". In: *Science* 312.5772 (2006), pp. 416–419. DOI: `10.1126/science.1124199`.

[28] L. Ding, Z. Jia, J. Nie, Y. Weng, L. Cao, H. Chen, X. Wu, and Q. Liu. "The structural and compositional evolution of precipitates in Al-Mg-Si-Cu alloy". In: *Acta Materialia* 145 (Dec. 2017).

[29] M. Torsæter, W. Lefebvre, C.D. Marioara, S.J. Andersen, J.C. Walmsley, and R. Holmestad. "Study of intergrown L and Q' precipitates in Al–Mg–Si–Cu alloys". In: *Scripta Materialia* 64.9 (2011), pp. 817–820. DOI: `https://doi.org/10.1016/j.scriptamat.2011.01.008`.

[30] J. M. Zuo and J. C. Spence. *Advanced Transmission Electron Microscopy: Imaging and Diffraction in Nanoscience.* Springer, 2017.

[31] J.D. Verhoeven. *Fundamentals of Physical Metallurgy.* Wiley, 1975.

[32] S. Wenner and R. Holmestad. "Accurately measured precipitate–matrix misfit in an Al–Mg–Si alloy by electron microscopy". In: *Scripta Materialia* 118 (2016), pp. 5–8. DOI: `https://doi.org/10.1016/j.scriptamat.2016.02.031`.

[33] S. J. Andersen, C. D. Marioara, J. Friis, R. Børge, Q. Du, I.G. Ringdalen, S. Wenner, E. A. Mørtsell, R. Holmestad, T. Saito, J. Røyset, and O. Reiso. "Directionality and Column Arrangement Principles of Precipitates in Al-Mg-Si-(Cu) and Al-Mg-Cu Linked to Line Defect in Al". In: *Materials Science Forum* 877 (Nov. 2016), pp. 461–470.

[34] C. Taylor. *Diffraction*. Adam Hilger, 1987.

[35] Retrieved from `https://en.wikipedia.org/wiki/Transmission_electron_microscopy#/media/File:Scheme_TEM_en.svg`. Accessed 21.02.2022.

[36] Y. Leng. *Materials Characterization: Introduction to Microscopic and Spectroscopic Methods*. Wiley, 2013.

[37] Ø. Paulsen. "Transmission Electron Microscopy Study of Two Peak Hardened Al-Mg-Si-Cu Alloys". MA thesis. NTNU, 2017.

[38] B. Fultz and J. Howe. *Transmission Electron Microscopy and Diffractometry of Materials*. Springer, 2013.

[39] T. Bergh. "Electron microscopy of intermetallic phases in aluminium-steel joints". PhD thesis. NTNU, 2021.

[40] R. Vincent and P. A. Midgley. "Double conical beam-rocking system for measurement of integrated electron diffraction intensities". In: *Ultramicroscopy* 53.3 (1994), pp. 271–282. DOI: `https://doi.org/10.1016/0304-3991(94)90039-6\%7D`.

[41] P. A. Midgley and A. S. Eggeman. "Precession electron diffraction – a topical review". In: *IUCrJ* 2.1 (Jan. 2015), pp. 126–136. DOI: `10.1107/S2052252514022283`.

[42] N. Tanaka. *Scanning Transmission Electron Microscopy Of Nanomaterials: Basics Of Imaging And Analysis*. Imperial College Press, 2014.

[43] E. A. Mørtsell. "Precipitation in multicomponent, lean, Al-Mg-Si alloys". PhD thesis. NTNU, 2016.

[44] R. Bierwolf, M. Hohenstein, F. Phillipp, O. Brandt, G.E. Crook, and K. Ploog. "Direct measurement of local lattice distortions in strained layer structures by HREM". In: *Ultramicroscopy* 49.1 (1993), pp. 273–285. DOI: `https://doi.org/10.1016/0304-3991(93)90234-O`.

[45] M.J. Hÿtch, E. Snoeck, and R. Kilaas. "Quantitative measurement of displacement and strain fields from HREM micrographs". In: *Ultramicroscopy* 74.3 (1998), pp. 131–146. DOI: `https://doi.org/10.1016/S0304-3991(98)00035-7`.

[46] J.K. Sunde, C.D. Marioara, A.T.J. van Helvoort, and R. Holmestad. "The Evolution of Precipitate Crystal Structures in an Al-Mg-Si(-Cu) Alloy Studied by a Combined HAADF-STEM and SPED Approach". In: *Materials Characterization* (2018). DOI: `https://doi.org/10.1016/j.matchar.2018.05.031`.

[47] J. L. Rouviere, A. Béché, Y. Martin, T. Denneulin, and D. Cooper. "Improved strain precision with high spatial resolution using nanobeam precession electron diffraction". In: *Applied Physics Letters* 103 (Dec. 2013), p. 241913. DOI: `10.1063/1.4829154`.

[48] A. M. F Muggerud, Y. Li, R. Holmestad, and S. J. Andersen. "Mackay icosahedron explaining orientation relationship of dispersoids in aluminium alloys". In: *Acta Crystallographica* 70.5 (2014), pp. 888–896.

[49]   H. Chandler et al. *Hardness testing*. ASM International, 1999.

[50]   Python Software Foundation. *Python*. Retrieved from `https://www.python.org/`. Accessed 09.05.2022.

[51]   J. S. Barnard, D. N. Johnstone, and P. A. Midgley. "High-resolution scanning precession electron diffraction: Alignment and spatial resolution". In: *Ultramicroscopy* 174 (2017), pp. 79–88. DOI: `https://doi.org/10.1016/j.ultramic.2016.12.018\%7D`.

[52]   S. Wenner. *Quantification of metastable precipitates in Al-Mg-Si alloys*. SINTEF procedure with document number 08139. SINTEF, 2021.

[53]   J. Schindelin, I. Arganda-Carreras, and E. et al. Frise. "Fiji: an open-source platform for biological-image analysis". In: *Natur Methods* 9 (July 2012), pp. 676–682. DOI: `10.1038/nmeth.2019`.

[54]   W.D. Smith and N.C. Wormald. "Geometric separator theorems and applications". In: *Proceedings 39th Annual Symposium on Foundations of Computer Science (Cat. No.98CB36280)*. 1998, pp. 232–243. DOI: `10.1109/SFCS.1998.743449`.

[55]   Gatan. *Gatan Microscopy Suite*. Retrieved at `https://www.gatan.com/products/tem-analysis/gatan-microscopy-suite-software`. Accessed 09.05.2022.

[56]   C. M. Hell. *CBED-ThicknessDetermination*. Version 3.0. June 2022. DOI: `10.5281/zenodo.6602265`. URL: `%5Curl%7Bhttps://github.com/TEM-Gemini-Centre/ThicknessDeterminationTEM%7D`.

[57]   *PyXem*. DOI: `10.5281/zenodo.2649351`.

[58]   *HyperSpy*. DOI: `10.5281/zenodo.6492919`.

[59]   S. van der Walt, J. L. Schönberger, J. Nunez-Iglesias, F. Boulogne, J. D. Warner, N. Yager, E. Gouillart, T. Yu, and the scikit-image contributors. "Scikit-image: image processing in Python". In: *PeerJ* 2 (June 2014), e453. DOI: `10.7717/peerj.453`.

[60]   S. Banerjee and A. Roy. *Linear Algebra and Matrix Analysis for Statistics*. Taylor & Francis Group, 2014.

[61]   A. S. Eggeman, R. Krakow, and P. A. Midgley. "Scanning precession electron tomography for three-dimensional nanoscale orientation imaging and crystallographic analysis". In: *Nature Communications* 6.1 (2015), p. 7267. DOI: `10.1038/ncomms8267`.

[62]   I. N. Prestholdt. "Strain mapping based on scanning (precession) electron diffraction of heterostructured semiconductor nanowires: set-up and analysis". MA thesis. NTNU, 2021.

[63]   H. D. Young and R. A. Freedman. *University Physics with Modern Physics*. 13th. Addison-Wesley, 2012.

[64]   H. Tvedt. *AutomAl 6000*. Retrieved from `http://automal.org`. Accessed 29.04.2022.

[65]   H. Tvedt, C. D. Marioara, E. Thronsen, C. Hell, S. J. Andersen, and R. Holmestad. "AutomAl 6000: Semi-automatic structural labelling of HAADF-STEM images of precipitates in Al–Mg–Si(–Cu) alloys". In: *Ultramicroscopy* 236 (2022), p. 113493. DOI: `https://doi.org/10.1016/j.ultramic.2022.113493`.

[66]   *Inkscape*. Retrieved from `https://inkscape.org/`. Accessed 09.05.2022.

[67] M. Torsæter, H. S. Hasting, W. Lefebvre, C. D. Marioara, J. C. Walmsley, S. J. Andersen, and R. Holmestad. "The influence of composition and natural aging on clustering during preaging in Al–Mg–Si alloys". In: *Journal of Applied Physics* 108.7 (2010), p. 073527. DOI: `10.1063/1.3481090`.

[68] J. H. Kim and T. Sato. "Effects of Cu Addition on Nanocluster Formation and Two-Step Aging Behaviors of AlMgSi Alloys". In: *Journal of Nanoscience and Nanotechnology* 11.2 (2011), pp. 1319–1322. DOI: `doi:10.1166/jnn.2011.3344`.

[69] M. Torsæter. "Quantitative studies of clustering and precipitation in Al-Mg-Si(-Cu) alloys". PhD thesis. NTNU, 2011.

[70] C.S.T. Chang, I. Wieler, N. Wanderka, and J. Banhart. "Positive effect of natural pre-ageing on precipitation hardening in Al–0.44at% Mg–0.38at% Si alloy". In: *Ultramicroscopy* 109.5 (2009), pp. 585–592. DOI: `https://doi.org/10.1016/j.ultramic.2008.12.002`.

[71] C. Marioara, S. Andersen, J. Jansen, and H. W. Zandbergen. "The influence of temperature and storage time at RT on nucleation of the β'' phase in a 6082 Al–Mg–Si alloy". In: *Acta Materialia* 51 (Feb. 2003), pp. 789–796. DOI: `10.1016/S1359-6454(02)00470-6`.

[72] S. Wenner, C. D. Marioara, S. J. Andersen, and R. Holmestad. "Effect of room temperature storage time on precipitation in Al–Mg–Si(–Cu) alloys with different Mg/Si ratios". In: *International Journal of Materials Research* 103.8 (2012), pp. 948–954. DOI: `doi:10.3139/146.110795`.

[73] J. Banhart, C.S.T. Chang, Z. Liang, N. Wanderka, M. D. H. Lay, and A. J. Hill. *Natural Aging in Al-Mg-Si Alloys - A Process of Unexpected Complexity*. In: *Advanced Engineering Materials* vol. 12.7 (July 2010), pp. 559–571. DOI: `10.1002/adem.201000041`.

[74] J. K. Sunde, Ø. Paulsen, S. Wenner, and R. Holmestad. "Precipitate statistics in an Al-Mg-Si-Cu alloy from scanning precession electron diffraction data". In: *Journal of Physics: Conference Series* 902 (Sept. 2017), p. 012022. DOI: `10.1088/1742-6596/902/1/012022`.

[75] J. Douin, P. Donnadieu, and F. Houdellier. "Elastic strain around needle-shaped particles embedded in Al matrix". In: *Acta Materialia* 58.17 (2010), pp. 5782–5788. DOI: `https://doi.org/10.1016/j.actamat.2010.06.053`.

[76] L. Jones, S. Wenner, M. Nord, P. H. Ninive, O. M. Løvvik, R. Holmestad, and P. D. Nellist. "Optimising multi-frame ADF-STEM for high-precision atomic-resolution strain mapping". In: *Ultramicroscopy* 179 (2017), pp. 57–62. DOI: `https://doi.org/10.1016/j.ultramic.2017.04.007`.

[77] P. H. Ninive, A. Strandlie, S. Gulbrandsen-Dahl, W. Lefebvre, C. D. Marioara, S. J. Andersen, J. Friis, R. Holmestad, and O. M. Løvvik. "Detailed atomistic insight into the β'' phase in Al–Mg–Si alloys". In: *Acta Materialia* 69 (2014), pp. 126–134. DOI: `https://doi.org/10.1016/j.actamat.2014.01.052`.

[78] R. Bjørge. Private communication. 2022.

[79] C. M. Hell and S. Wenner. Private communication. 2022.

[80] E. Christiansen, C. D. Marioara, B. Holmedal, O. S. Hopperstad, and R. Holmestad. "Nano-scale characterisation of sheared β'' precipitates in a deformed Al-Mg-Si alloy". In: *Scientific Reports* 9.1 (2019), p. 17446. DOI: `10.1038/s41598-019-53772-4`.

[81]   R. Tovey, D. N. Johnstone, S. M. Collins, W. R. B. Lionheart, P. A. Midgley, M. Benning, and C.-B. Schönlieb. "Scanning electron diffraction tomography of strain". In: *Inverse Problems* 37.1 (Dec. 2020), p. 015003. DOI: 10.1088/1361-6420/abc961.

[82]   D. N. Johnstone, A. T. J. van Helvoort, and P. A. Midgley. "Nanoscale Strain Tomography by Scanning Precession Electron Diffraction". In: *Microscopy and Microanalysis* 23.S1 (2017), pp. 1710–1711. DOI: 10.1017/S1431927617009217.

Appendices

A   Supporting Results

A.1   HRTEM Images

Figure A1: HRTEM images of the L phase from the **0-48** condition are shown in (a) and (c). Their corresponding FFTs are shown in (b) and (d). The Al reflections are marked with white circles, except for the center spot. The Si-network is marked with yellow dashed lines.

20-48

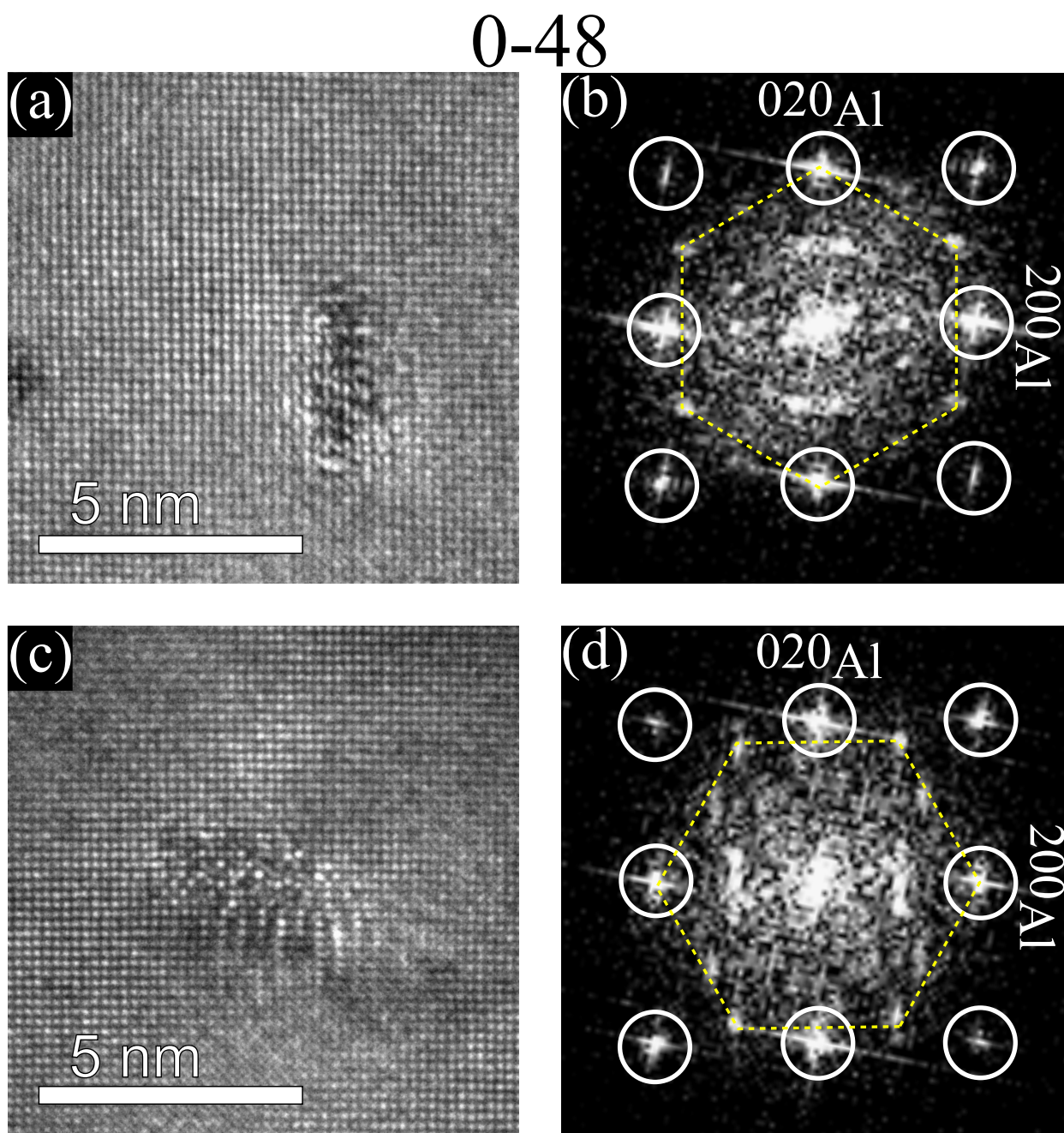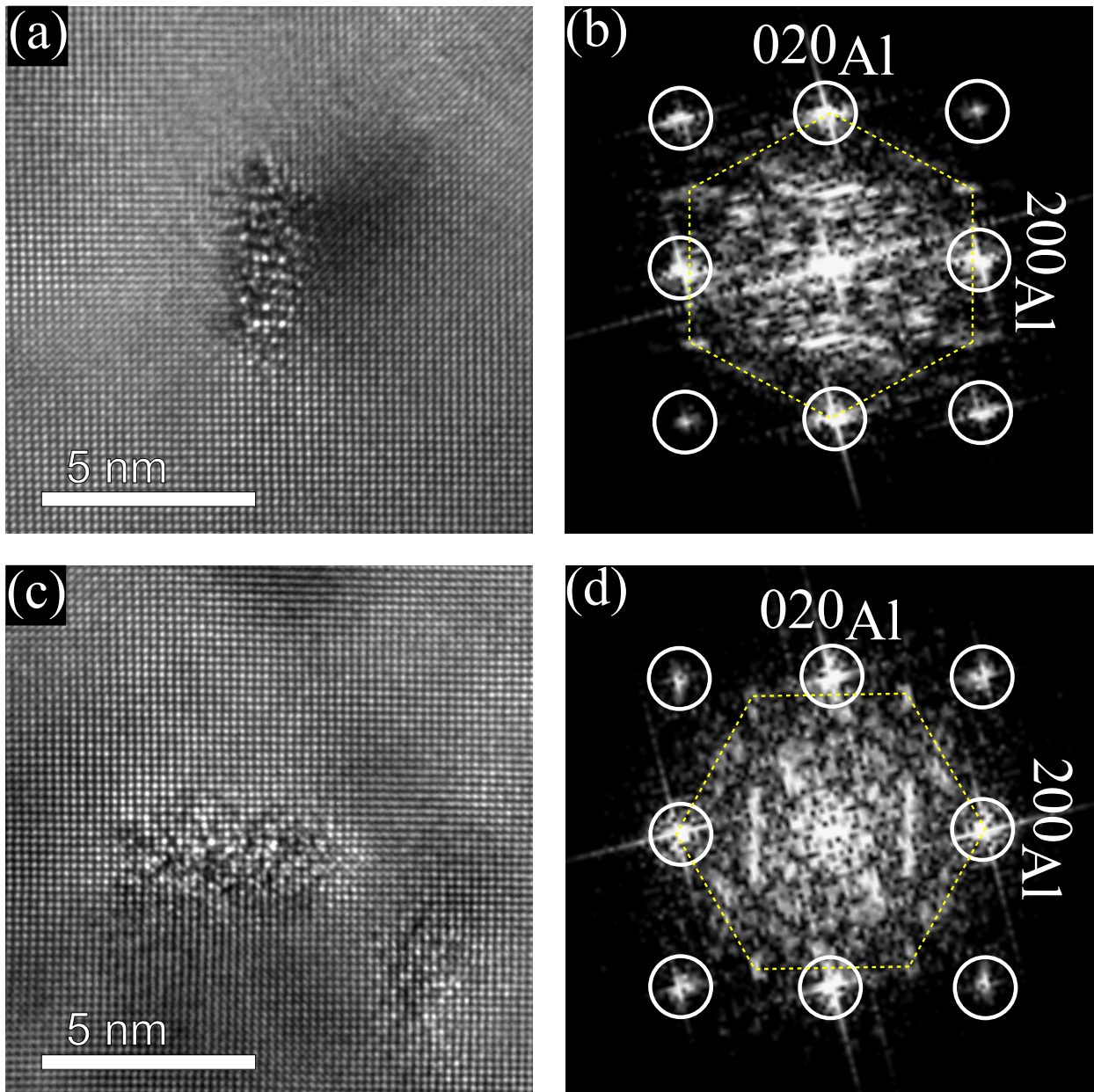Figure A2: HRTEM images of the L phase from the **20-48** condition are shown in (a) and (c). Their corresponding FFTs are shown in (b) and (d). The Al reflections are marked with white circles, except for the center spot. The Si-network is marked with yellow dashed lines.
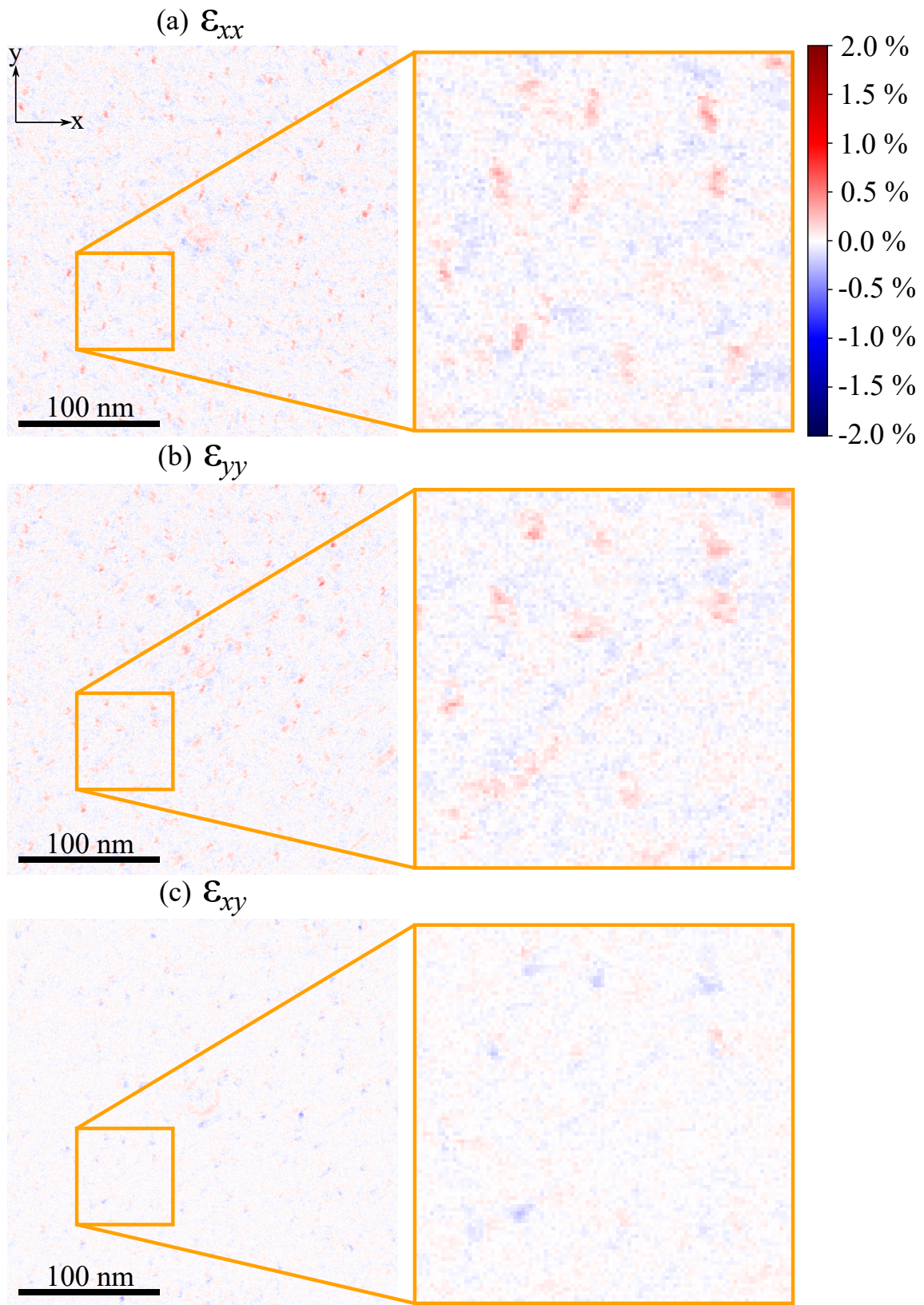
Figure A3: Strain map for Sample 2 from the **0-48** condition. The colour bar and the x- and y-axis in (a) applies to all three strain components.

A.3 HAADF-STEM Images

<center>0-48</center>
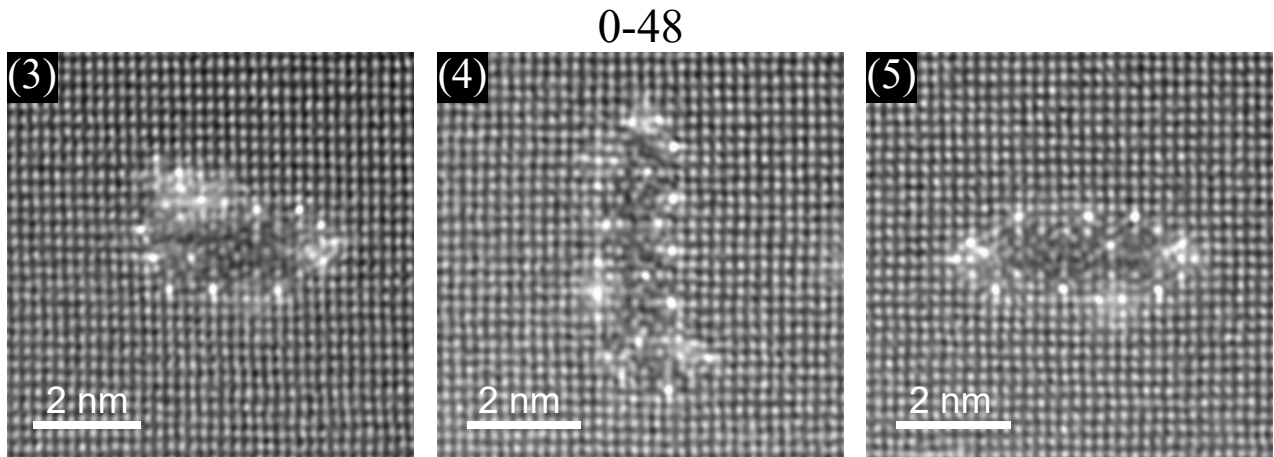
Figure A4: HAADF-STEM images for the **0-48** condition. These are the precipitates nr. 3, 4 and 5 in Table 4.2 for the **0-48** condition. The HAADF-STEM images were obtained by Dr. Sigurd Wenner.
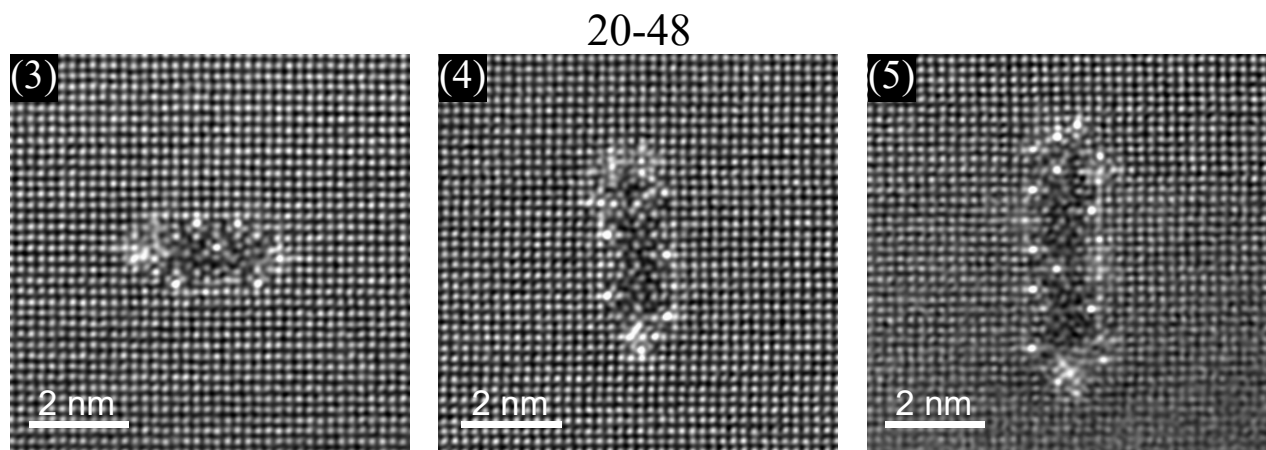
<center>20-48</center>

Figure A5: HAADF-STEM images for the **20-48** condition. These are the precipitates nr. 3, 4 and 5 in Table 4.2 for the **20-48** condition. The HAADF-STEM images were obtained by Dr. Sigurd Wenner.

B SPED Calibration

The SPED calibration was done on the **20-48** dataset, and since all three datasets were taken by the same operator with the same parameters and within a close time frame, the values were assumed to apply to the remaining two datasets from the **0-48** condition.

B.1 Diffraction

The scale of the DPs taken at a camera length of 23.4 cm was calculated by using the PED pattern of Al oriented at the [001] zone axis. The distance from the center of the central beam to the center

of the (200) reflection was measured to be 52.7 pixels. The reciprocal distance between the peaks was calculated using $g_{200} = 1/d_{200} = 0.4938\,\text{Å}^{-1}$. This gave the calibration value of $0.009\,37\,\text{Å}^{-1}$/pixel.

B.2 Camera Length, L

By using trigonometry, the equation for the camera length L is given by,

$$L = \frac{R_g}{\tan(2\theta_{\mathrm{B}})}, \tag{A1}$$

where R_g is the real space distance between the central beam and the (200) reflection in this case, and θ_{B} is the Bragg angle. One can express Bragg's law from equation (2.28) as $\lambda = 2d\sin(\theta_{\mathrm{B}})$, and since θ_{B} is small, one can approximate $2\sin(\theta_{\mathrm{B}}) \approx 2\theta_{\mathrm{B}} \approx 2\tan(\theta_{\mathrm{B}})$. The equation for the camera length then becomes

$$L = \frac{R_g d}{\lambda}, \tag{A2}$$

where R_g was calculated by using detector specifications saying that one pixel equals $55\,\mu\text{m}$, giving $2.8985\,\text{mm}$ for 52.7 pixels. Equation (2.3) was used to calculate $d = 2.025\,\text{Å}$, and $\lambda = 2.508\,\text{pm}$ is the wavelength of electrons accelerated by a voltage of $200\,\text{kV}$. The nominal value of the camera length was $12\,\text{cm}$, but equation (A2) found the true camera length to be $23.4\,\text{cm}$.

B.3 Convergence Semi-Angle, α

The electron beam used during SPED was not parallel but had a convergence semi-angle α. The equation for α is given by,

$$2\alpha = 2\theta_{\mathrm{B}}\frac{a}{b}, \tag{A3}$$

where θ_{B} is the Bragg angle from equation (2.28) for a given reflection, a is the diameter of a diffraction disc in the PED pattern, and b is the distance between the central beam and the (200) reflection in this case. By using equation (A3), the resulting convergence semi-angle was calculated to be $1.41\,\text{mrad}$.

B.4 Scan (nm/pixel)

A BF-TEM image was taken of the SPED scan area (see Figure 5.3) and by comparing it to the virtual real space image from SPED dataset, two precipitates were identified in both images. These precipitates were chosen as far apart from each other as possible. The distance between the precipitates in the BF-image was measured to be $185.9\,\text{nm}$, and 268.5 pixels in the SPED scan. The resulting scan calibration was calculated to be $0.692\,\text{nm/pixel}$, so the scan area of 400 x 400 pixels was $276.8\,\text{nm}$ x $276.8\,\text{nm}$ in real space.

Phase mapping

June 3, 2022

1   Code for phase mapping of YKK alloy

A combination of code written by senior engineer Emil Frang Christiansen, PhD student Elisabeth Thronsen and master student Elisabeth Savitri Thrane.

1.0.1   Import important libraries

```python
import matplotlib.pyplot as plt
import matplotlib as mpl
%matplotlib qt5
plt.ion()
import numpy as np
from scipy import sqrt
import hyperspy.api as hs
import pyxem as px
from skimage.feature import blob_log, blob_dog
from pathlib import Path
import os

directory = r'/mnt/d6fb6352-6539-4ae7-a82a-04732c3cfc12/Elisabeth ST/
 ↪archive_20220125/zipped' # Directory where you have the data
os.chdir(r'/home/elisasth/Documents'.replace('\\', '\\\\')) # Directory with␣
 ↪ClusterAnalysis
import ClusterAnalysis as ca
os.chdir(directory) # Change back to directory where you have the files.

from ClusterAnalysis import VDF_mask_methods as vdfm
from skimage import (
    color, feature, filters, io, measure, morphology, segmentation, util
)

%config Completer.use_jedi = False
from math import isnan
from matplotlib import cm
from scipy.constants import pi
from matplotlib.patches import Circle
from scipy.optimize import curve_fit
```

1.0.2 Masking tools

```python
def radial_coordinates(signal, axes = [0, 1], offset_x = 0, offset_y = 0):
    """
    Generate a radial coordinate grid for the signal in its signal space.

    :param signal: The signal to generate the grid for
    :type signal: hyperspy.signals.BaseSignal
    :param axes: The axes that define the signal space. Default is [2, 3].
    :type axes: array-like
    :param offset_x: Offset of radial coordinates along x. Default is 0
    :type offset_x: float
    :param offset_y: Offset of radial coordinates along y. Default is 0
    :type offset_y: float
    """
    X, Y = np.meshgrid(signal.axes_manager[axes[0]].axis, signal.
 ↪axes_manager[axes[1]].axis)
    return np.sqrt((X-offset_x)**2 + (Y-offset_y)**2)

def plot_masks_on_data(data, mask, *args, log_scale = False, patches=None,
 ↪extent = 'auto', **kwargs):
    """
    Plots masks on top of data.

    :param data: The data to plot together with the masks
    :type data: numpy.ndarray
    :param mask: The mask to plot on top of the data
    :type mask: numpy.ndarray
    :param log_scale: Whether to plot data in log-scale or not.
    :type log_scale: bool
    :param patches: List of patch objects to add to plot, e.g. patches marking
 ↪the masks.
    :type patches: list
    :param args: Positional arguments passed to matplotlib.pyplot.figure()
    :param kwargs: Keyword arguments passed to matplotlib.pyplot.figure()
    """

    figure = plt.figure(*args, **kwargs)
    ax1 = figure.add_subplot(131)#, xticks=[], yticks=[], title = 'Summed
 ↪pattern')
    if log_scale:
        ax1.imshow(np.log(data), cmap='inferno_r', extent=extent,
 ↪origin='lower')
    else:
        ax1.imshow(data, cmap='inferno_r', extent=extent, origin='lower')
    if patches is not None:
```

```python
        [ax1.add_patch(patch) for patch in patches]#[Circle((blob[1], blob[0]),␣
↪radius=blob[2] * radius_scale, fill=False, edgecolor='r') for blob in blobs]]

    ax2 = figure.add_subplot(132, xticks=[], yticks=[], title='Mask')
    ax2.imshow(mask, cmap='RdBu_r', extent=extent, origin='lower')

    ax3 = figure.add_subplot(133, xticks=[], yticks=[], title='Input to NMF')
    if log_scale:
        ax3.imshow(np.log(data * mask), cmap='inferno_r', extent=extent,␣
↪origin='lower')
    else:
        ax3.imshow(data * mask, cmap='inferno_r', extent=extent, origin='lower')

    plt.tight_layout()
    return figure, [ax1, ax2, ax3]

class Blob(object):
    def __init__(self, x, y, r):
        """
        Create a blob
        """

        self.x = float(x)
        self.y = float(y)
        self.r = abs(float(r))

    def __repr__(self):
        return '{self.__class__.__name__}({self.x!r}, {self.y!r}, {self.r!r})'.
↪format(self=self)
    def __format__(self, format_spec):
        return '{self.__class__.__name__} at ({self.x:{f}}, {self.y:{f}}) with␣
↪radius {self.r:{f}}'.format(self=self, f=format_spec)

    def __str__(self):
        return '{self:.2f}'.format(self=self)

    def __add__(self, other):
        if isinstance(other, type(self)):
            return Blob(self.x + other.x, self.y + other.y, max([self.r, other.
↪r]))
        elif isinstance(other, (list, tuple, np.ndarray)):
            return Blob(self.x + other[0], self.y + other[1], self.r)
        else:
            return Blob(self.x+other, self.y+other, self.r)

    def __radd__(self, other):
        return self + other
```

```python
    def __neg__(self):
        return Blob(-self.x, -self.y, self.r)

    def __sub__(self, other):
        return self + (-other)

    def __rsub__(self, other):
        return other + (-self)

    def __mul__(self, other):
        if isinstance(other, type(self)):
            return Blob(self.x * other.x, self.y * other.y, self.r * other.r)
        elif isinstance(other, (list, tuple, np.ndarray)):
            return Blob(self.x * other[0], self.y * other[1], self.r * other[2])
        else:
            return Blob(self.x * other, self.y * other, self.r * other)

    def __rmul__(self, other):
        return self * other

    def __truediv__(self, other):
        if isinstance(other, type(self)):
            return Blob(self.x / other.x, self.y / other.y, self.r / other.r)
        else:
            return Blob(self.x / other, self.y / other, self.r / other)

    def __rtruediv__(self, other):
        return 1/(self/other)


    def draw(self, ax, *args, **kwargs):
        """
        Draw the blob into an axis
        """
        ax.add_patch(Circle((self.x, self.y), radius=self.r, *args, **kwargs))


def detect_blobs(image, blob_detection=blob_dog, scale = 1, offsets = [0, 0],
 ↪**kwargs):
    blobs = [Blob(blob[1], blob[0], blob[2]) for blob in blob_detection(image,
 ↪**kwargs)]
    return [blob * scale + offsets for blob in blobs]
```

```python
def create_diffraction_mask(signal, cutoff=None, radius_scale=2, minimum_radius
↪= 15, plot_results = True, plot_log=False, fit_gaussians=False,
↪blob_detection=blob_dog, **kwargs):
    """
    Create a diffraction pattern mask.

    :param signal: Signal (diffraction pattern) to use as template for the mask
    :type signal: Union[hyperspy.signals.BaseSignal, numpy.array]
    :param cutoff: Radius of general cutoff, in scaled units. Default is None,
↪in which case no general cutoff is performed
    :type cutoff: Union[None, float]
    :param radius_scale: Scaling for detected radius. Default is 2.
    :type radius_scale: float
    :param minimum_radius: Minimum radius to use in pixels. Radii below this
↪value is increased to this value.
    :type minimum_radius: float
    :param plot_results: Whether to plot results or not. Default is True
    :type plot_results: bool
    :param plot_log: Whether to plot results in log scale or not. Default is
↪False.
    :type plot_log: bool
    :param fit_gaussians: Whether to fit 2D gaussians to features detected by
↪blobs or not. Default is False
    :type fit_function: bool
    :param blob_detection: Blobdetection algorithm. Default is skimage.feature.
↪blob_dog
    :type blob_detection: function
    :param kwargs: keyword arguments passed to blob detection function.

    :returns: Masks
    :rtype: numpy.ndarray
    """

    if cutoff is not None:
        mask = ~(radial_coordinates(signal) <= cutoff)
    else:
        mask = np.zeros(np.shape(signal), dtype=bool) #take all of image

    #Create new pixel grid in pixel coordinates
    blobs = detect_blobs(signal.data, scale = signal.axes_manager[0].scale,
↪offsets=[signal.axes_manager[0].offset, signal.axes_manager[1].offset],
↪**kwargs)
    print('Found blobs:')
    [print(blob) for blob in blobs]
    for blob in blobs:
        if fit_gaussians:
```

```python
            try:
                G, (popt, pcov) = fit_gaussian(signal.data, p0=[1e3, blob.x,
 ↪blob.y, blob.r, blob.r, 0, 0], bounds = ([0, blob.x-blob.r, blob.y-blob.r,
 ↪blob.r, blob.r, 0, 0], [np.inf, blob.x+blob.r, blob.y+blob.r, 5*blob.r,
 ↪5*blob.r, 2*np.pi, np.inf]))
                print('Successfully fitted {G:.2f} to {blob:.2f}'.format(G=G,
 ↪blob=blob))
                blob.x, blob.y, blob.r = G.x, G.y, np.sqrt(2*np.log(2))*np.
 ↪max([G.sx, G.sy])
            except Exception as e:
                print('Error when fitting gaussian to blob {blob}: {e}'.
 ↪format(blob=blob, e=e))
        blob.r *= radius_scale
        if blob.r < minimum_radius*signal.axes_manager[0].scale:
            blob.r = minimum_radius*signal.axes_manager[0].scale
        #blob.r += 2*signal.axes_manager[0].scale

        mask += (radial_coordinates(signal, offset_x=blob.x, offset_y=blob.y) <
 ↪blob.r)

    if plot_results:
        #fig, axes = plot_masks_on_data(signal.data, mask, log_scale=True,
 ↪extent = [min(signal.axes_manager[0].axis), min(signal.axes_manager[1].
 ↪axis), max(signal.axes_manager[0].axis), max(signal.axes_manager[1].axis)])
        fig, axes = plot_masks_on_data(signal.data, mask, log_scale=True,
 ↪extent = [min(signal.axes_manager[0].axis), max(signal.axes_manager[0].
 ↪axis), min(signal.axes_manager[1].axis), max(signal.axes_manager[1].axis)])
        [blob.draw(axes[0], fill=False, edgecolor='r') for blob in blobs]

    return mask
```

1.0.3 Load data

```python
#data_path = Path("/mnt/d6fb6352-6539-4ae7-a82a-04732c3cfc12/Elisabeth ST/
 ↪archive_20220125/zipped/NA20hAA48h.hspy")
#data_path = Path("/mnt/d6fb6352-6539-4ae7-a82a-04732c3cfc12/Elisabeth ST/
 ↪20220201 131253/NA0hAA48h.hspy")
data_path = Path("/mnt/d6fb6352-6539-4ae7-a82a-04732c3cfc12/Elisabeth ST/
 ↪20220307_135854/0hNA2dAA.hspy")
sliced=False
```

```python
non_centered_signal = hs.load(data_path)
```

```python
non_centered_signal.set_signal_type('electron_diffraction')
non_centered_signal.axes_manager
```

```
[ ]: if sliced:
         non_centered_signal = non_centered_signal.inav[200:400,:].deepcopy()
         non_centered_signal.plot()
```

1.0.4 Center direct beam

Create maximum plot

```
[ ]: cmap = mpl.cm.get_cmap("magma").copy()
     maximums = non_centered_signal.max(axis=[0,1])
     maximums.plot(scalebar=False,axes_off=True,colorbar=False,cmap=cmap.reversed())
     roi = hs.roi.CircleROI(cx=0,cy=0, r_inner=0, r=0.07)
     roi.add_widget(maximums)
```

Find radius and cx, cy

```
[ ]: radius = roi.r/maximums.axes_manager[0].scale
     print(radius)
     cx = (roi.cx-maximums.axes_manager[0].offset)/maximums.axes_manager[0].scale
     cy = (roi.cy-maximums.axes_manager[1].offset)/maximums.axes_manager[1].scale
     print(cx, cy) #128 128
     center = (cx, cy)
```

Find center of mass (CoM)

```
[ ]: com = non_centered_signal.center_of_mass(mask = (cx,cy,radius))
```

Calculate shifts

```
[ ]: shift_x = (com.inav[0]-cx)
     shift_y = (com.inav[1]-cy)
```

```
[ ]: signal_centered = non_centered_signal.shift_diffraction(shift_x=shift_x,⌴
     ↪shift_y=shift_y, inplace=False)
```

```
[ ]: signal_centered.plot()
```

```
[ ]: plt.close('all')
     cmap = mpl.cm.get_cmap("magma").copy()
     Maximums = signal_centered.max(axis=[0,1])
     Maximums.plot(scalebar=False,axes_off=True,colorbar=False,cmap=cmap.reversed())
```

1.0.5 Create virtual BF/DF

```
[ ]: try:
         DP_scale
     except:
         DP_scale = signal_centered.axes_manager[2].scale
```

```
roi = hs.roi.CircleROI(cx=center[0]*DP_scale/256,cy=center[1]*DP_scale/256,
 ↪r_inner=0*DP_scale, r=30*DP_scale)
plt.close('all')
signal_centered.plot_integrated_intensity(roi=roi)
```

```
[ ]: # Save the virtual image created with the interactive aperture:
     vdf = signal_centered.get_integrated_intensity(roi)
```

```
[ ]: vdf.plot()
```

1.0.6 Prepare data for SVD and NMF

Set a cutoff, crop the signal space, and mask out reflections. Optionally (and advisable), add a circular cutoff to take of asymmetric cropping (square).

```
[ ]: plt.close('all')
     cutoff = 0.7
     signal_cutoff = signal_centered.isig[-cutoff:cutoff, -cutoff:cutoff]
     summed_signal = signal_cutoff.sum(axis=(0,1))
     summed_signal.plot()
     mask = create_diffraction_mask(summed_signal, cutoff=0.7, threshold=1E-15,
      ↪min_sigma=5, max_sigma=20)
```

```
[ ]: plt.close('all')
     signal_cutoff.plot()
```

```
[ ]: plt.close('all')
     signal = signal_cutoff*~mask
     signal.plot()
```

1.0.7 Perform SVD/NMF decomposition

```
[ ]: plt.close('all')
     signal.change_dtype('float32')

     algo = 'NMF' #SVD 'NMF'
     components = 10 #80 for SVD #9 for NMF, 10 for sliced
     #max_iter = 200
```

```
[ ]: signal.decomposition(normalize_poissonian_noise=True, algorithm=algo,
      ↪output_dimension=components)
```

```
[ ]: signal.plot_decomposition_results()
```

```
[ ]: if algo == 'SVD':
         signal.plot_explained_variance_ratio()
```

```python
from ClusterAnalysis import plot as caplt
output_directory = r'/mnt/d6fb6352-6539-4ae7-a82a-04732c3cfc12/Elisabeth ST/
 ↪Output_data_NA0hAA48h'
```

Save figures as tiff with viridis colormap. Saves also loadings and factors as hdf5 files. Uses code from Elisabeth

```python
factors = signal.get_decomposition_factors()
loadings = signal.get_decomposition_loadings()
#Save the images
caplt.save_component_maps(signal, factors, loadings, algo, output_directory,
 ↪components, scalebar=False,
                          saveFactorsLoadings=True) # Scalebar only works if you
 ↪have matplotlib-scalebar package installed (https://pypi.org/project/
 ↪matplotlib-scalebar/)
```

Save decomposed data

```python
signal.save(data_path.with_name(f'{data_path.
 ↪stem}_{algo}_{components}_decomposed'))
```

1.0.8 Plot loadings and factors using magma colormap, and save figures as png

```python
plt.close("all")
cmap = mpl.cm.get_cmap("magma").copy()
```

```python
plt.close("all")
from matplotlib import colors

for i in range(0,components):
    print(i)
    fig, axes = plt.subplots(nrows=1, ncols=2)
    axes[0].imshow(loadings.inav[i], cmap=cmap) #norm=colors.LogNorm() for
 ↪logarithmic colorscale
    axes[1].imshow(factors.inav[i], cmap=cmap)
    axes[0].set_title(f'Loading {i}')
    axes[1].set_title(f'Factor {i}')
    axes[0].axis("off")
    axes[1].axis("off")
    path = output_directory + f'/{algo}_{components}_components/
 ↪{algo}_decompresult{i}.png'
    print(path) #check if path is correct
    plt.savefig(path) #to save figures
```

```python
plt.close("all")
```

1.0.9 Load pre-decomposed dataset

```python
from ClusterAnalysis import plot as caplt
#file_path = Path("/mnt/d6fb6352-6539-4ae7-a82a-04732c3cfc12/Elisabeth ST/
 →20220307_135854/0hNA2dAA_NMF_7_decomposed.hspy")
#file_path = Path("/mnt/d6fb6352-6539-4ae7-a82a-04732c3cfc12/Elisabeth ST/
 →20220201 131253/NA0hAA48h_NMF_10_decomposed.hspy")
file_path = Path("/mnt/d6fb6352-6539-4ae7-a82a-04732c3cfc12/Elisabeth ST/
 →archive_20220125/zipped/NA20hAA48h_NMF_9_decomposed.hspy")
#output_directory = Path('/mnt/d6fb6352-6539-4ae7-a82a-04732c3cfc12/Elisabeth
 →ST/Output_data_NA0hAA48h')
output_directory = Path('/mnt/d6fb6352-6539-4ae7-a82a-04732c3cfc12/Elisabeth ST/
 →Output_data_NA20hAA48h')
pre_signal = hs.load(file_path)
```

```python
loadings = pre_signal.get_decomposition_loadings()
factors = pre_signal.get_decomposition_factors()
```

1.0.10 Save as loadings and factors as svg

```python
plt.close("all")
from matplotlib import colors
components= 7#9, 10, 7, 15
algo="NMF"
cmap = mpl.cm.get_cmap("magma").copy()

for i in range(0,components):
    print(i)
    fig, axes = plt.subplots(nrows=1, ncols=2)
    axes[0].imshow(loadings.inav[i], cmap="Greys") #norm=colors.LogNorm() for
→logarithmic colorscale cmap.reversed() "Greys"
    axes[1].imshow(factors.inav[i], cmap="Greys") #norm=colors.LogNorm() cmap.
→reversed() "Greys"
    axes[0].set_title(f'Loading {i}')
    axes[1].set_title(f'Factor {i}')
    axes[0].axis("off")
    axes[1].axis("off")
    path = output_directory + f'/{algo}_{components}_components/
→{algo}_decompresult{i}_greys.svg'
    print(path) #check if path is correct
    #plt.savefig(path, format="svg", dpi=800) #to save figures
```

```python
plt.close("all")
```

1.0.11 Give phases each own colour and plot it

```python
pre_signal = signal.deepcopy()
phases = {
    'A': [1,3,7],
    'B': [5,8],
    #'C': [9]
}
#For NA2OhAA48h: [1,3,7], [5,8]
#For NAOhAA48h with beta'': [1,3,4,7], [6,8], [9]
#For NAOhAA48h with no beta'': [1,3,4], [5,6]
```

```python
plt.close("all")

from matplotlib.colors import to_rgba
from matplotlib.colors import LinearSegmentedColormap

color_names = ['red','turquoise']

colors = [to_rgba(c) for c in color_names]

cmap = LinearSegmentedColormap.from_list('gt_cmap', colors, N=len(color_names))

fig = plt.figure(figsize=(6, 6), dpi=1200)
ax = fig.add_axes([0, 0, 1, 1], xticks=[], yticks=[], frameon=False)

loading_rgb = np.zeros((np.shape(pre_signal)[:2]+(4,)))
factor_rgb = np.zeros((np.shape(pre_signal)[2:])+(4,))

comps = ['A','B'] #['A','B','C']
for phase_number, phase in enumerate(comps):
    phase_components = phases[phase]
    if cmap is None:
        color = [0, 0, 0, 1]
        color[phase_number%3] = 1
    else:
        color = cmap(int(phase_number*255/len(comps)))
    print(color)
    component_loading_rgb = np.zeros(np.shape(loading_rgb))
    component_factor_rgb = np.zeros(np.shape(factor_rgb))
    for comp in phase_components:
        for color_index, c in enumerate(color):
            component_loading_rgb[:, :, color_index] += c*loadings.inav[comp].
 data
            component_factor_rgb[:, :, color_index] += c*factors.inav[comp].data
    loading_rgb += component_loading_rgb/np.max(component_loading_rgb)
    factor_rgb += component_factor_rgb/np.max(component_factor_rgb)
```

```python
ax.imshow(loading_rgb-background)
ax.imshow(factor_rgb)
inset = fig.add_axes([0.7, 0.7, 0.299, 0.299], xticks=[], yticks=[],
 →frameon=False)
inset.imshow(factor_rgb)
fig_label = '_'.join([f'{phase}' for phase in comps])
fig.show()
print(f'{output_directory.stem}_{fig_label}.svg')
#fig.savefig(file_path.with_name(f'{file_path.stem}_{fig_label}.png'))
#fig.savefig(output_directory.with_name(f'{output_directory.
 →stem}_{fig_label}_diff.svg'), format="svg", dpi = 1200)
```

Strain mapping

June 3, 2022

1   Strain mapping code made by Ingeborg Nævra Prestholdt

1.0.1   Adapted by Elisabeth Savitri Thrane for the YKK alloy

Import pyxem and required libraries

```python
# For external figs
%matplotlib tk

# Div packages
import pyxem as pxm
import numpy as np
import hyperspy.api as hs
from matplotlib import pyplot as plt
from pathlib import Path

# For strain mapping
from pyxem.generators.subpixelrefinement_generator import␣
 ↪SubpixelrefinementGenerator
from pyxem.signals.tensor_field import *
from pyxem.generators.displacement_gradient_tensor_generator import *

# For background subtraction
from skimage.filters import threshold_local
```

Self-made functions for easier strain mapping and use of multiple reflection peaks

```python
#Choosing which subpixelgenerator method to use, either center of mass ('com')
#or conventional cross correlation ('xc')
def SubPixGen(subpixgen,method,values):
    if method == 'com':
        return subpixgen.center_of_mass_method(values[0])
    elif method == 'xc':
        return subpixgen.conventional_xc(values[1][0],values[1][1],values[1][2])
    else:
        print('Put in either com or xc')
        return 0
```

```python
#Subtracting two opposite y peaks to create one long y vector, countering drift
 ↪effects in the y-direction
def subtract_yvecs(peak_array):
    fdarray = np.asarray(peak_array)
    arr_dim = len(fdarray.shape)
    if arr_dim == 2:
        correct_array = np.asarray([fdarray[0],fdarray[1]-fdarray[2]])
    elif arr_dim == 4:
        i_length = len(fdarray)
        j_length = len(fdarray[0])
        correct_array = np.full((i_length,j_length,2,2),0.0)
        for i in range (i_length):
            for j in range(j_length):
                x,y_plus,y_minus = fdarray[i][j][0], fdarray[i][j][1],
 ↪fdarray[i][j][2]
                correct_array[i][j][0] = x
                correct_array[i][j][1] = y_plus - y_minus
    else:
        print('You have to put in an array of the correct dimensions.')
        correct_array = [0,0]
    return correct_array

#Combining opposite x and y peaks in order to counter drift effects
def drift_correction(peak_array):
    fdarray = np.asarray(peak_array)
    arr_dim = len(fdarray.shape)
    if arr_dim == 2:
        correct_array = np.
 ↪asarray([fdarray[0]-fdarray[1],fdarray[2]-fdarray[3]])
    elif arr_dim == 4:
        i_length = len(fdarray)
        j_length = len(fdarray[0])
        correct_array = np.full((i_length,j_length,2,2),0.0)
        for i in range (i_length):
            for j in range(j_length):
                x_plus,x_minus,y_plus,y_minus = fdarray[i][j][0],
 ↪fdarray[i][j][1], fdarray[i][j][2], fdarray[i][j][3]
                correct_array[i][j][0] = x_plus - x_minus
                correct_array[i][j][1] = y_plus - y_minus
    else:
        print('You have to put in an array of the correct dimensions.')
        correct_array = [0,0]
    return correct_array
```

Load data

```
[ ]: #data_path = "/mnt/d6fb6352-6539-4ae7-a82a-04732c3cfc12/Elisabeth ST/
     ↪archive_20220125/zipped/NA20hAA48h.hspy"
     #data_path = "/mnt/d6fb6352-6539-4ae7-a82a-04732c3cfc12/Elisabeth ST/20220201␣
     ↪131253/NA0hAA48h.hspy"
     data_path = "/mnt/d6fb6352-6539-4ae7-a82a-04732c3cfc12/Elisabeth ST/
     ↪20220307_135854/0hNA2dAA.hspy"
     sliced=False
     non_centered_s = hs.load(data_path, lazy=False)
```

1.0.2 0.0.1 Preprocessing for Topspin data

Convert the data to log scale and perform background removal

```
[ ]: #Convert the data to log scale (in a figure you can convert to log scale by␣
     ↪pressing the 'l' key)
     #non_centered_s.data = np.where(non_centered_s.data > 0, np.log(non_centered_s.
     ↪data),0)

     #Background removal
     #non_centered_s = non_centered_s.subtract_diffraction_background('difference of␣
     ↪gaussians',min_sigma=3,max_sigma=10)
     #non_centered_s.compute()

     non_centered_s.set_signal_type('electron_diffraction')
     non_centered_s.plot()
     non_centered_s.axes_manager
```

```
[ ]: non_centered_s.metadata
```

```
[ ]: plt.close("all")
     if sliced:
         non_centered_s = non_centered_s.inav[200:400,:].deepcopy()
         non_centered_s.plot()
```

Center direct beam

```
[ ]: maximums = non_centered_s.max(axis=[0,1])
     maximums.plot()
     roi = hs.roi.CircleROI(cx=0,cy=0, r_inner=0, r=0.07)
     roi.add_widget(maximums)
```

```
[ ]: radius = roi.r/maximums.axes_manager[0].scale
     print(radius)
     cx = (roi.cx-maximums.axes_manager[0].offset)/maximums.axes_manager[0].scale
     cy = (roi.cy-maximums.axes_manager[1].offset)/maximums.axes_manager[1].scale
     print(cx, cy) #128 128
     center = (cx, cy)
```

```
[ ]: com = non_centered_s.center_of_mass(mask = (cx,cy,radius))
```

```
[ ]: shift_x = (com.inav[0]-cx)
     shift_y = (com.inav[1]-cy)
```

```
[ ]: s = non_centered_s.shift_diffraction(shift_x=shift_x, shift_y=shift_y,␣
     ↪inplace=False)
```

1.0.3 0.0.2 Vector Based strain mapping

Peaks found manually

Find neutral strain values from average DP from reference region.
Use either center_of_mass method(square_size) or conventional_xc(square_size, disc_radius, up-sample_factor).

square_size : int, Length (in pixels) of one side of a square the contains the peak to be refined
disc_radius: int, Radius (in pixels) of the discs that you seek to refine
upsample_factor: int, Factor by which to upsample the patterns

```
[ ]: #Manually located reference peaks for peak vectors, ref [40:60,430:450]
     #For NA20hAA48h:
     '''
     a1 = [-0.6709,-0.1883]#[-0.6709,-0.1935][-0.6556,-0.1988]
     b1 = [-0.2305,-0.4294]#[-0.2252,-0.4347][-0.2252,-0.4294]
     c1 = [0.2099,-0.6706]#[0.2151,-0.6654][0.2256,-0.6706]
     d1 = [-0.4297,0.2573]#[-0.4297,0.2521][-0.4245,0.2521]
     center = [0.01067,0.01618]#[0.01591,0.01094]
     d2 = [0.4458,-0.225]#[0.4511,-0.2302][0.4563,-0.2302]
     c2 = [-0.1938,0.6925]#[-0.1833,0.6872]
     b2 = [0.2518,0.4513]#[0.2466,0.4513][0.2623,0.4461]
     a2 = [0.6975,0.2102]#[0.7132,0.2102]

     method_values = [36,[36,14,100]] #[com values, cross-correlation values], 26,0.
     ↪35 for Gaussian fitting

     #For NA0hAA48h with beta'':
     a1 = [-0.4979,-0.4819]
     b1 = [-0.005057,-0.4871]
     c1 = [0.4878,-0.5028]
     d1 = [-0.4874,0.02142]
     center = [0.005428,0.005697]
     d2 = [0.5035,-0.004789]
     c2 = [-0.4821,0.5352]
     b2 = [0.01591,0.509]
     a2 = [0.5087,0.4985]

     method_values = [36,[36,14,100]]
```

```
'''
#For NA0hAA48h without beta'':
a1 = [-0.6918,-0.02576]
b1 = [-0.3091,-0.3718]
c1 = [0.04737,-0.6968]
d1 = [-0.372,0.3412]
center = [0.001067,0.005697]
d2 = [0.3829,-0.3298]
c2 = [-0.04176,0.7239]
b2 = [0.3357,0.3832]
a2 = [0.7132,0.04764]

method_values = [36,[36,14,100]]
```

```
[ ]: #Make position finding easier by setting diffraction calibration to 1
     #s.set_diffraction_calibration(1)

     #Define which peaks will be used for the strain mapping
     x_plus = d1
     x_minus = d2
     y_plus = b1
     y_minus = b2
     method = 'com' #Input either 'xc' or 'com', depending on what method you want␣
      ↪to use
     two_peaks = [x_plus,y_plus]
     three_peaks = [x_plus,y_plus,y_minus]
     peaks = [x_plus,x_minus,y_plus,y_minus]
```

Define, and manually find the reference peak positions from average DP from reference region

Create average DP of a reference region, e.g. 20x20 pixels:

```
[ ]: s.plot()
```

```
[ ]: plt.close("all")
     #For NA20hAA48h:
     #s_ref = s.inav[160:180,305:325]
     #s_ref = s.inav[285:305,145:165] #ref2
     #s_ref = s.inav[55:75,120:140] #ref3

     #For NA0hAA48h with beta'':
     #s_ref = s.inav[110:130,105:125]
     #s_ref = s.inav[140:160,270:290]
     #s_ref = s.inav[145:165,95:115] #Too red

     #For NA0hAA48h without beta'':
     s_ref = s.inav[140:160,258:278]
```

```
s_refm = s_ref.mean((0,1))
```

Plot DP and manually locate the peak positions

```
[ ]: s_refm.plot(vmax=500)
```

Find peak positions with sub-pixel precision in the reference region, using one of the three peak
finding routines; Center of mass, cross-correlation or Gaussian fitting

```
[ ]: spg_ref = SubpixelrefinementGenerator(s_refm, np.asarray(peaks))

    #For center of mass or cross-correlation, use:
    vector_ref = SubPixGen(spg_ref,method,method_values)

    #For Gaussian fitting use:
    #vector_ref = spg_ref.fitting_gaussians_method(36, intensity_ratio=0.35)
```

Depending on the number of peaks chosen, use one of these to combine the ones that need combining:

```
[ ]: Vs_ref = drift_correction(vector_ref) #Combining two peaks in both x and y.

    #Vs_ref = subtract_yvecs(vector_ref) #Assuming you only have one x-peak,␣
     ↪commbining two y-peaks

    #Vs_ref = np.asarray(vector_ref) #Assuming you only have one peak in x and y,␣
     ↪two peaks total
```

Choose region for strain mapping

```
[ ]: #For NA20hAA48h:
    #s1 = s.inav[100:250,250:400]
    #s1 = s.inav[0:400,0:400]

    #For NA0hAA48h with beta'':
    #s1 = s.inav[0:200,0:400]

    #For NA0hAA48h without beta'':
    s1 = s.inav[0:400,0:400]
    s1.change_dtype('float64')
    s1
```

Determine peak positions to subpixel precision for the rest of the data, using one of the three
methods; Center of mass, cross-correlation or Gaussian fitting

```
[ ]: spg = SubpixelrefinementGenerator(s1, np.asarray(peaks))

    #For center of mass or cross-correlation, use:
    peak_vectors = SubPixGen(spg,method,method_values)
```

```
#For Gaussian fitting use:
#peak_vectors = spg.fitting_gaussians_method(36, intensity_ratio=0.35)
```

Depending on the number of peaks chosen, use one of these to combine the ones that need combining:

```
[ ]: Vs = drift_correction(peak_vectors) #Combining two peaks in both x and y.

     #Vs = subtract_yvecs(peak_vectors) #Assuming you only have one x-peak,␣
     ↪combining two y-peaks

     #Vs = peak_vectors #Assuming you only have one peak in x and y, two peaks total
```

Compare distorted and undistorted diffraction vectors to obtain a strain map

```
[ ]: D = get_DisplacementGradientMap(hs.signals.Signal2D(Vs), Vs_ref)
     strain_map = D.get_strain_maps()
```

```
[ ]: plt.close("all")
     strain_map.plot(cmap='seismic',vmax=0.02,vmin=-0.02)
```

Save the strain map

```
[ ]: #strain_map.save('/home/elisasth/Pictures/NA20hAA48h/Strain/
     ↪NA20hAA48h_strain-map_com_ref3')
     strain_map.save('/home/elisasth/Pictures/NA0hAA48h/Strain/
     ↪NA0hAA48h_strain-map_com_nobeta')
```

```
[ ]: strain_map.axes_manager
```

1.0.4   0.0.3 Load strain map hspy file

```
[ ]: #strain_map_path = "/home/elisasth/Pictures/NA20hAA48h/Strain/
     ↪NA20hAA48h_strain-map_com_ref3.hspy"
     #strain_map_path = "/home/elisasth/Pictures/NA0hAA48h/Strain/
     ↪NA0hAA48h_strain-map_com_nobeta.hspy"
     strain_map_path = "/home/elisasth/Pictures/NA0hAA48h/Strain/
     ↪NA0hAA48h_strain-map_com.hspy"

     #With log
     #strain_map_path = "/home/elisasth/Pictures/NA20hAA48h/Strain/
     ↪NA20hAA48h_strain-map_com_log.hspy"
     #strain_map_path = "/home/elisasth/Pictures/NA0hAA48h/Strain/
     ↪NA0hAA48h_strain-map_com_log.hspy"
```

```
[ ]: strain_map_fin = hs.load(strain_map_path)
```

```
[ ]: plt.close("all")
     strain_map_fin.plot(cmap='seismic',vmax=0.02,vmin=-0.02)

     #For NA20hAA48h:
     #line = hs.roi.Line2DROI(x1=116, y1=0, x2=116, y2=400, linewidth=15)
     #line = hs.roi.Line2DROI(x1=0, y1=195, x2=400, y2=195, linewidth=15)

     #For NA0hAA48h:
     #line = hs.roi.Line2DROI(x1=116, y1=0, x2=116, y2=400, linewidth=15)
     #line = hs.roi.Line2DROI(x1=0, y1=195, x2=400, y2=195, linewidth=15)
     #line.add_widget(strain_map_fin)
```

```
[ ]: trace = line(strain_map_fin)
     trace.plot( )
```

1.0.5 0.0.4 Rolling ball background subtraction

```
[ ]: #savepath = "/home/elisasth/Pictures/NA20hAA48h/Strain_svg_files/"
     savepath = "/home/elisasth/Pictures/NA0hAA48h/Strain_svg_files/"

     def plot_comparison(image, background, name):
         fig, ax = plt.subplots(nrows=1, ncols=3)

         ax[0].imshow(image, cmap='seismic',vmax=0.02,vmin=-0.02)#vmax=0.02,vmin=-0.
      ↪02
         ax[0].set_title('Original image')
         ax[0].axis('off')
         plt.colorbar(im0)

         ax[1].imshow(background, cmap='seismic',vmax=0.02,vmin=-0.02)
         ax[1].set_title('Background')
         ax[1].axis('off')

         ax[2].imshow(image - background, cmap='seismic',vmax=0.02,vmin=-0.02)
         ax[2].set_title('Result')
         ax[2].axis('off')

         fig.tight_layout()
         #fig.savefig(f'{savepath}{name}_NA20hAA.svg',format="svg",dpi=800)
         #fig.savefig(f'{savepath}{name}_NA0hAA.svg',format="svg",dpi=800)
         fig.savefig(f'{savepath}{name}_NA20hAA_beta.svg',format="svg",dpi=800)

     def plot_result(image, background, name):
         plt.figure()
         im = plt.imshow(image - background, cmap='seismic',vmax=0.02,vmin=-0.02)␣
      ↪#*100 and write percent
         plt.title('Result')
```

```
    plt.axis('off')
    plt.colorbar(im)
    #plt.savefig(f'{savepath}{name}_NA20hAA_Result.svg',format="svg",dpi=800)
    #plt.savefig(f'{savepath}{name}_NA0hAA_Result.svg',format="svg",dpi=800)
    plt.savefig(f'{savepath}{name}_NA20hAA_Result_beta.
 ↪svg',format="svg",dpi=800)
```

```
[ ]: image = strain_map_fin.data
```

```
[ ]: #For NA20hAA48h:
     background0 = threshold_local(image[0], 41, offset=0, method='gaussian') #51 #41
     background1 = threshold_local(image[1], 41, offset=0, method='gaussian')
     background2 = threshold_local(image[2], 41, offset=0, method='gaussian')
     background3 = threshold_local(image[3], 41, offset=0, method='gaussian')
```

```
[ ]: #For NA0hAA48h with beta'':
     background0 = threshold_local(image[0], 31, offset=0, method='gaussian')#51
     background1 = threshold_local(image[1], 31, offset=0, method='gaussian')
     background2 = threshold_local(image[2], 31, offset=-0.0001, method='gaussian')
     background3 = threshold_local(image[3], 31, offset=0, method='gaussian')#np.
      ↪percentile(strain_map_fin,1) #median
```

```
[ ]: #For NA0hAA48h without beta'':
     background0 = threshold_local(image[0], 41, offset=0, method='gaussian') #51 #41
     background1 = threshold_local(image[1], 41, offset=0, method='gaussian')
     background2 = threshold_local(image[2], 41, offset=0, method='gaussian')
     background3 = threshold_local(image[3], 41, offset=0, method='gaussian')
```

```
[ ]: plt.close("all")
     plot_comparison(image[0], background0, "Exx")
     plot_comparison(image[1], background1, "Eyy")
     plot_comparison(image[2], background2, "Exy")
     plot_comparison(image[3], background3, "Theta")
     plt.show()
```

```
[ ]: plt.close("all")
     plot_result(image[0], background0, "Exx")
     plot_result(image[1], background1, "Eyy")
     plot_result(image[2], background2, "Exy")
     plot_result(image[3], background3, "Theta")
     plt.show()
```

```
[ ]: plt.close("all")
```

Elisabeth Savitri Thrane

Effect of Natural Ageing on an Al-Cu-Mg-Si Alloy

NTNU
Norwegian University of
Science and Technology